Investigation of Structure-Function Relationships of Supported Metal Catalysts for the Aldehyde-Water-Shift Reaction

by

Wei-Chung Wen

A dissertation submitted in partial fulfillment
of the requirements for the degree of
Doctor of Philosophy
(Chemical Engineering)
in the University of Michigan
2019

Doctoral Committee:

Professor Erdogan Gulari, Co-Chair
Emeritus Professor Levi T. Thompson Jr., Co-Chair
Assistant Professor Charles C. L. McCrory
Professor Johannes W. Schwank

Wei-Chung Wen

weichung@umich.edu

ORCID iD: 0000-0003-0373-4563

Dedication

This dissertation is dedicated to my beloved family.

Acknowledgements

The work presented in this dissertation would not be possible without the generous support from numerous individuals. First and foremost, I would like to thank my advisor, Prof. Levi Thompson for his tremendous support and guidance. He saw potential in me and always encouraged and challenged me to think critically. This fostered me to become a better researcher and individual, both personally and professionally. Additionally, as I am not a native English speaker, I am especially grateful for his patience and the extra effort that he was willing to make in helping me to cultivate my speaking and writing skills to and become a better presenter and writer. I would not be able to achieve what I achieve today without the support and encouragement from Prof. Thompson.

I would like to express my gratitude to my dissertation committee members: Prof. Mark Barteau, Prof. Erdogan Gulari, Prof. Charles McCrory, and Prof. Johannes Schwank. In particular, Prof. Barteau always shared his comprehensive knowledge in catalysis and provided me with insightful discussion in surface chemistry and catalyst characterization. Prof. Gulari kindly agreed to join my committee as a co-chair in my last year, and advised me with his expertise in reforming catalysis. His support is greatly appreciated. Prof. McCrory is always encouraging and inspired me from the angle of chemistry, which allowed me to explore more possibility of the research projects. When I seemed to focus too much on experimental details, Prof. Schwank kindly led me to grasp the big picture, and urged me to view the project from practical and industrially relevant perspectives. I am also very grateful for his unconditional support over the past five years.

I also had the privilege to work with many talented individuals over the course of grad school, especially my colleagues in the Thompson group and the Barteau group. I appreciate the professional and personal interactions with Dr. Saemin Choi, Dr. Shawn Eady, Dr. Jason Gaudet, Dr. Tapiwa Mushove, Dr. Jee-Jay Chen, Dr. Yuan Chen, Dr. Brian Wyvratt, Dr. Abdoulaye Djire, Dr. Xingyi Yang, Dr. Siu on Tung, Dr. Tanya Breault, Dr. Krista Hawthorne, Dr. Ameed Nour, Anisha Rehlan, Allison Franck, Ryan Franck, Dr. Jonathan Kucharyson, Dr. Sarah Paleg, Dr. Trenton Wilkes, Dr. Sydney Laramie, Dr. Jennifer Jocz, Dr. Xiaowen Zhao, Saral Carl, Scott Johnson, Jingran Xiao, Zixuan Wang, Jiwoong Kang, Connor McGlothin, Elizabeth Wilson, Olabode Fujah, Nishanth Bharadwaj, Ronald Hobson, and Zewei Chen. These interactions and experiences were essential for my development, and I had a great time working with them.

Through the different stages of my grad school, there are a few individuals I would like to especially thank. Dr. Tapiwa Mushove is a great friend and mentor since I came to the States. Being my first roommate and lab colleague, Tapiwa warmly welcomed me to the community and helped me to adapt promptly to grad school with his experience and generous friendship. He became my mentors for my grad school and career in later years. Dr. Yuan Chen, Dr. Brian Wyvratt, and Dr. Shawn Eady are also great friends, who are always understanding and supportive. We spent countless nights working together in lab; the night would be much longer and lonelier without their company. They are also great mentors. Yuan and Brian taught me a great deal about catalysis, from system construction to materials characterizations, when I first joined the group. Shawn not only provided me with insight from the perspective of chemistry through discussion, but also offered valuable advice on the manuscript that we worked on together. I would also like to thank Dr. Saemin Choi. He has is always willing to help and discuss the challenges that I encountered in research. He also generously advised my communication and writing skills,

especially during my 5th year, which I am particularly grateful for. I would also like to acknowledge Dr. Jason Gaudet for his continuous supports with in-depth discussion and his extensive expertise in catalysis, especially in system design, reaction kinetics, and problem solving. Jason and I are also working on a manuscript, and his constructive suggestions and feedback are greatly appreciated.

I'd also like to extend my appreciation to a distinct group of friends at Michigan, who supported me tremendously over the course of my graduate study. While it is difficult to mention everybody, I particularly appreciate the warm friendships from the tennis community, especially Dr. Juhchin Yang, Grace Chang, Dr. Guo-Hao Lin, Dr. Chuang Hsun-Jen, Roger Lu, Peng-Kai Kao, and Kevin Wu. I am also grateful for the support from Michigan Taiwanese Student Association. Among the members of the association, I would like to especially acknowledge Dr. Jee-Jay Chen, Dr. Wen-Chi Lin, and Boyu Chang. Jee-Jay, Wen-Chi, and Boyu are great friends and mentors, who heartily welcomed me and introduced me to the community, and became my mentors for my grad school and career later on. I am also grateful to the members of our band, Dr. Hung-An Ting, Tung-Yu Wu, and Su-Yang Shieh. We had a great time playing instruments and singing together, which is one of the best memories that I had here in Michigan.

Additionally, I would like to acknowledge the Center for Enabling New Technologies Through Catalysis (CENTC), which was an innovation center under the National Science Foundation, for providing the funding for this research. I also would like to thank Dr. Jiu-Hwa L. Upshur for her generous support via the Chia-Lun Lo Fellowship. Meanwhile, I am grateful for my interactions with Dr. L. J. Chen, who was the CEO of AU Optronics Corp. when I first met him in my undergraduate. By sharing his experience, Dr. Chen inspired me to study abroad in the

United States, and propelled me determined to pursue my Ph.D. degree. I would not have started my grad school without his inspiration.

Last but not least, I must thank my family. My dear dad, mom, and brother. While being over 7,500 miles away from home and studying alone in the United States could be unbearably lonely, with the strong bonding among family members and their support, I never had felt separated and solitary. Finally, I want to thank my girlfriend, Joy, who has always been there with me to share every piece of my happiness, frustration, excitement, and suspense, and who brings love and the real joy to my life.

Table of Contents

Dedication ..... **ii**

Acknowledgements ..... **iii**

List of Tables ..... **xi**

List of Figures ..... **xv**

Abstract **1**

Chapter 1 Introductions **1**

1.1 Motivation 1

1.1.1 Production of Chemicals from Biomass-Derivatives 2

1.1.2 The Use of Water as Oxidant for Hydrogen Production 5

1.2 Aldehyde Water Shift Reaction 8

1.3 Heterogeneous Catalysts for Oxidation Reactions with Water 11

1.3.1 Metal Oxide Supported Metal Catalysts 11

1.3.2 Molybdenum Carbide Supported Metal Catalyst 14

1.4 Potential Reaction Pathways and Side Reactions 16

1.5 Research Goals and Organization of the Dissertation 17

1.6 Reference 19

Chapter 2 AWS with Metal Oxide Supported Metal Catalysts **22**

2.1 Introduction 22

2.2 Experimental Methods 25

2.2.1 Catalyst Synthesis 25
2.2.2 Materials Characterization 26
2.2.3 Reaction Rate and Selectivity Measurements 28
2.3 Results 30
2.3.1 Catalyst Characterization 30
2.3.2 Aldehyde Water Shift Activity 34
2.3.3 Selectivity 39
2.4 Discussion 42
2.5 Conclusion 47
2.6 Reference 48
Chapter 3 AWS with Mo_2C Supported Metal Catalysts 50
3.1 Introduction 50
3.2 Experimental Methods 52
3.2.1 Catalyst Synthesis 52
3.2.2 Material Characterizations 54
3.2.3 Reaction Rate and Selectivity Measurement 55
3.3 Results 56
3.3.1 Catalyst Characterization 56
3.3.2 Aldehyde Water Shift Activity 60
3.3.3 Selectivity 65
3.4 Discussion 66
3.5 Conclusion 69
3.6 References 70
Chapter 4 Investigation of Active Sites on Mo_2C Supported Metal Catalysts 72
4.1 Introduction 72

4.2 Experimental Methods 74
4.2.1 Materials and Methods 74
4.2.2 Reaction Rate and Selectivity Measurement 78
4.2.3 Activity Deconvolution 79
4.2.4 Active Site Model Derivation 79
4.3 Results 80
4.3.1 Catalyst Characterization 80
4.3.2 Aldehyde Water Shift Activity 84
4.3.3 Sides Reactions and Selectivity 90
4.3.4 Reaction Pathway Calculations 93
4.4 Discussion 95
4.5 Conclusion 99
4.6 References 100

Chapter 5 Reaction Kinetics of α-MoC_{1-x} and β-Mo_2C Supported Metal Catalysts 102

5.1 Introduction 102
5.2 Experimental Methods 104
5.2.1 Catalyst Synthesis 104
5.2.2 Material Characterizations 106
5.2.3 Reaction Rate and Selectivity Measurement 109
5.2.4 Rate Expressions for Kinetic Study 112
5.3 Results 117
5.3.1 Catalyst Characterization 117
5.3.2 Aldehyde Water Shift Activity 119
5.3.3 Selectivity 121
5.3.4 Reaction Kinetic and Mechanism 123

5.4 Discussion 129
5.5 Conclusion 133
5.6 References 134
Chapter 6 Summary and Recommended Future Work 136
6.1 Summary and Overall Conclusions 136
6.2 Extension of Current Research 139
6.2.1 Further Examining the Characteristics of Surface Sites 139
6.2.2 Revealing the Impact of Metal-Support Interactions to AWS activity 141
6.2.3 Further Investigating Reaction Kinetics and Mechanisms 142
6.3 Research in New Areas 143
6.3.1 Elucidating the Effect of Preparation Methods on Carbide-based Catalysts 143
6.3.2 Understanding the Effect of Carbide Structure and Metal/Carbon Ratio 144
6.3.3 Coupling the Experimental Research with Computational Works 146
6.3.4 Extend the AWS Studies to Other Model Compounds 147
6.4 Reference 147
Appendix 150

List of Tables

Table 1.1 Thirty bio-derivatives that has top potentials for the use of building blocks. The final twelve sugar-derived building blocks are marked in bold. In the final twelve, succinic acid, fumaric acid, and malic acid were categorized as 1,4 diacids. Adapted from [6]. 3

Table 1.2 Gravimetric and volumetric energy densities of common fuels. Adapted from [19]. ... 7

Table 2.1 Select catalyst surface and physical properties for the catalysts. 31

Table 2.2 Results from nonlinear regression of H_2 production rates for Cu-Zn-Al, Nano-Cu, Cu/CeO_2, Pt/CeO_2, Cu/Al_2O_3, and Pt/Al_2O_3 empirical decay rate laws. a(t) is the ratio of the rate at time t to the initial rate (a=r(t)/ro), kd is the specific decay constant, and t is time on stream. 37

Table 2.3 The AWS rates and Cu site-normalized rates at 240 ˚C, and the associated activation energies. 39

Table 2.4 Average ethanol and crotonaldehyde production rates and turnover frequencies for metal oxide-supported catalysts and bare supports at 240 °C over 14 hrs on stream. 42

Table 3.1 Surface and physical properties for the Mo_2C based catalysts synthesized via wet impregnation. 57

Table 3.2 Results from nonlinear regression of 0.1 ML M/Mo_2C catalysts to empirical decay rate laws. 62

Table 3.3 AWS rates and turnover frequencies at 240 °C and activation energies for the various catalysts. 63

Table 3.4 Stabilized ethanol and crotonaldehyde production rates at 240 °C after 10 hours deactivation on stream. 65

Table 4.1 Surface and physical properties for all catalysts. 82

Table 4.2 Percentage of Mo_2C surface exposed and Cu dispersion calculated based on the CO uptake results. 84

Table 4.3 Results from nonlinear regression of Mo_2C-based catalysts empirical decay rate laws. 86

Table 4.4 AWS 240°C rates, Cu normalized rate, and activation energy 88

Table 4.5 AWS activity and CO uptake results for selective fresh and regenerated catalysts..... 90

Table 4.6 Stabilized production rates of acetic acid, ethanol, and crotonaldehyde at 240 °C. 91

Table 4.7 The error calculation for the production rates of H_2, ethanol, and acetic acid. 94

Table 5.1 Examples of different designations of different structure of the molybdenum carbide in the literature. 103

Table 5.2. Synthesis temperature program protocols for α-MoC_{1-x} and β-Mo_2C [4,16]..... 106

Table 5.3 Acetaldehyde and water partial pressure variations used in the kinetic study over α-MoC_{1-x}, β-Mo_2C, 1.0 ML Cu/α-MoC_{1-x}, and 1.0 ML Cu β-Mo_2C. 112

Table 5.4 Redox, Eley-Rideal (ER), Langmuir-Hinshelwood (L-H, single and two sites) models used for kinetic data fittings. 115

Table 5.5 Surface and physical properties for α-MoC_{1-x} and β-Mo_2C and their supported Cu catalysts. Results for supported Cu catalysts prepared by wet impregnation are also included for reference. 118

Table 5.6 H_2 production rates and turnover frequencies at 240 °C and activation energies for α-MoC_{1-x}, β-Mo_2C, and their supported Cu catalysts prepared via incipient wetness impregnation. 120

Table 5.7 Stabilized acetic acid, ethanol and crotonaldehyde production rates at 240 °C for α-MoC_{1-x}- and β-Mo_2C-based catalysts. 122

Table 5.8 Fitting results for α-MoC_{1-x}, β-Mo_2C, 1.0 ML Cu/α-MoC_{1-x}, and 1.0 ML Cu/β-Mo_2C using power law. Rate data for AWS reaction, Cannizzaro reaction, and aldol condensation were fitted with Matlab: Rate = k [aldehyde]^a[water]^w, all $R^2 > 0.92$.. 126

Table 5.9 Model discrimination results for α-MoC_{1-x}, β-Mo_2C, 1.0 ML Cu/α-MoC_{1-x}, and 1.0 ML Cu/β-Mo_2C using redox, E-R, and L-H models. The presented figures follow the order of standard error of residuals (S), Akaike information criterion (AIC) (residual sum of squares, degree of freedoms). Models that produced the top-three best fits for each catalyst are highlighted. 127

Table 5.10 AWS kinetic parameters for the best-fit E-R model (aldehyde adsorb, RDS: surface reaction). 128

Table 5.11 AWS kinetic parameters for the best-fit L-H model (single type of site, RDS: surface reaction) for α-MoC_{1-x}-based catalysts. 128

Table 5.12 AWS kinetic parameters for the redox model with water reduction as the RDS for β-Mo_2C-based catalysts. 129

Table 5.13 AWS kinetic parameters for the best-fit L-H model (two types of site, RDS: surface reaction). 129

Table 6.1 Comparison of surface properties and AWS activity for 0.1 ML Cu/Mo_2C via incipient wetness impregnation and wet impregnation. 144

Table A.1 Thermodynamic properties and Gibbs free energy of reactions. 150

Table A.2 Carbon balance for all catalysts examined in this dissertation..... 152

List of Figures

Figure 1.1 A Sankey diagram depicting the passage from fossil fuel feedstocks to chemical products sector for 2013. NGLs: Natural gas liquids, N-fertilizers: Nitrogenous fertilizers. Figure adapted from [1]. 1

Figure 1.2 Schematic illustration of the potential oxidation products from 5-Hydroxymethylfurfural (HMF). Reaction intermediates include maleic anhydride (MA), 2,5-diformylfuran (DFF), 5-hydrox- ymethyl-2-furancarboxylic acid (HFCA), 2-formyl-5-furancar-boxylic acid (FFCA), and 2,5-furan dicarboxylic acid (FDCA). Adapted from [7]. 4

Figure 1.3 Syngas generation and water gas shift reactors for ammonia synthesis. HC= hydrocarbon, HTS= high temperature shift. Adapted from [17]..... 6

Figure 1.4 Hydrogen production pathways developed by Office of Energy Efficiency and Renewable Energy, U.S. Department of Energy. Central: produce at large facilities and then delivered to the point of use. Distributed: produce at or near the site of use in. Taken from [21]..... 8

Figure 1.5 Half-sandwich complexes of Ir, Rh, and Ru. Adapted from [23]. 9

Figure 1.6 Two major reaction mechanisms proposed for WGS on CeO_2-based catalysts: (a) Redox and (b) associative mechanism using Pt/CeO_2 as example. Adapted from [56]. 13

Figure 1.7 Preferential binding geometries calculated for the adsorbates on the C-terminated Mo_2C (001) surface. Taken from [58]. 14

Figure 1.8 Reactions that could potentially occur under the condition employed. 16

Figure 2.1 The role of metal and support in WGS reaction sequence; Pt/CeO_2 as example. Figure adopted from [9]. 24

Figure 2.2 Schematic of acetaldehyde adsorption on Cu surface with the presence of surface oxygen. Adopted from [21]. 25

Figure 2.3 Scheme diagram of the AWS reactor. The red line highlight the pathway of a reactant stream during experiment. 30

Figure 2.4 Diffraction patterns for (a) CeO_2-, (b) Al_2O_3-, and (c) SiO_2-supported Cu catalysts, Cu-Zn-Al, and Nano-Cu. Relevant standards were included: CuO (JCPDF 98-00-0429), Cu_2O (JCPDF 98-000-0186), Cu (JCPDF 00-004-0836), Pt (JCPDF 00-004-0802), Au (JCPDF 00-004-0787), ZnO (JCPDF 00-005-0664), CeO_2 (JCPDF 00-034-0394), and Al_2O_3 (JCPDF 00-047-1308). SiO_2 is amorphous 32

Figure 2.5 Surface area normalized NH_3 desorption spectra for metal oxide-supported catalysts and bare supports. 33

Figure 2.6 Normalized deactivation profiles for H_2 production (relative to initial rates) at 240 °C for the CeO_2-and Al_2O_3-supported Cu and Pt catalysts, Cu-Zn-Al, and Nano-Cu catalysts. 35

Figure 2.7 Arrhenius plots of the H_2 production rate rates for CeO_2- and Al_2O_3-supported metal catalysts. 39

Figure 2.8 Carbon selectivities for the catalysts. The selectivities are defined as the moles of acetaldehyde reacted to form a specific product divided by the total amount of acetaldehyde converted. 40

Figure 2.9 Schematic representation of the proposed AWS reaction mechanism on Cu/CeO_2. . 45

Figure 3.1 Diffraction patterns for Mo_2C-supported metal catalysts and relevant standards: Pt (JCPDF 00-004-0802), Au (JCPDF 00-004-0787), Cu (JCPDF 00-004-0836), α-MoC_{1-x} (JCPDF 00-015-0457), β-Mo_2C (JCPDF 00-035-0787). 58

Figure 3.2 Pictures taken after adding the Mo_2C catalysts into the Cu precursor solution. (a) Mo_2C. The solution remains clear and no precipitate observed. (b) K_NReduce/Mo_2C (K/Mo_2C without reduction). Blue precipitate observed. (c) K_Reduce/Mo_2C (K/Mo_2C reduced at 450 °C). Blue precipitate observed. 59

Figure 3.3 The XRD pattern of the blue precipitate and Malachite $Cu_2(OH)_2(CO_3)$ standard pattern from the Jade database (red line). 59

Figure 3.4 Deactivation profiles of 0.1 ML M/Mo_2C and Cu-Zn-Al catalysts at 240°C..... 60

Figure 3.5 Arrhenius plots of the AWS reaction rates for Mo_2C supported metal catalysts. 64

Figure 3.6 Carbon selectivities for M/Mo_2C catalysts. The selectivity is defined as the moles of acetaldehyde reacted to form certain product divided by the total amount of acetaldehyde converted. 66

Figure 4.1 Diffraction patterns Mo_2C and Mo_2C-supported metal catalysts. Relevant standards: Cu (JCPDF 00-004-0836), α-MoC_{1-x} (JCPDF 00-015-0457), and β-Mo_2C (JCPDF 00-035-0787). 81

Figure 4.2 CO TPD spectra for Mo2C supported metal catalysts. 83

Figure 4.3 Deactivation profiles at 240°C for Mo_2C-based catalysts. 85

Figure 4.4 AWS rates 240°C for Cu on Mo_2C as a function of Cu loading; predicted rates using the perimeter site and surface site models were included. 89

Figure 4.5 Arrhenius plots showing the A WS areal rates for all Mo2C-based catalysts. 89

Figure 4.6 Carbon selectivities for catalysts. 92

Figure 4.7 Cannizzaro reaction rates versus acid sites density of Mo_2C-based catalysts. 93

Figure 4.8 Schematic of the reaction mechanism on Cu/Mo_2C catalyst. 97

Figure 4.9 Schematic of the speculated Cannizzaro reaction mechanism on Mo_2C-based catalysts. 98

Figure 5.1 Bulk crystallographic structures of (a) face-center-cubic, (b) the hexagonal-close-packed (hcp), and (c) orthorhombic carbide. Turquoise and magenta spheres denote C and Mo atoms, respectively. Adopted from [1]. 102

Figure 5.2 Point of zero charge determination for the unpassivated Mo_2C, passivated Mo_2C, and MoO_2 materials. Adopted from [7]. 109

Figure 5.3 The order of partial pressure variations of acetaldehyde and water. 111

Figure 5.4 Point of zero charge determination for the native α-MoC_{1-x} and β-Mo_2C. 117

Figure 5.5 Diffraction patterns for α-MoC_{1-x}, β-Mo_2C, 1.0 ML Cu/α-MoC_{1-x}, and 1.0 ML Cu/β-Mo_2C. 119

Figure 5.6 Arrhenius plots for the α-MoC_{1-x}, β-Mo_2C, 1.0ML Cu/α-MoC_{1-x}, and 1.0ML Cu/β-Mo_2C catalysts. Data m-Mo_2C and 1.0 ML Cu/m-Mo_2C are also included. Given that the m-Mo_2C is a mixture of α-MoC_{1-x} and β-Mo_2C, it is not surprising that the m-Mo_2C shows an activity in between α-MoC_{1-x} and β-Mo_2C. 121

Figure 5.7 Carbon selectivity for α-MoC_{1-x}, β-Mo_2C, 1.0 ML Cu/α-MoC_{1-x}, and 1.0 ML Cu/β-Mo_2C. The data was collected during the pseudo-steady-state regime at 240 °C. 123

Figure 5.8 Reaction rates (a) AWS reaction, (b) Cannizzaro reaction, and (c) aldol condensation as a function of acetaldehyde partial pressure. The partial pressure of water was kept at a constant of 0.15 atm. The data was collected during the pseudo-steady-state regime at 240 °C. The data points in color blue is the results for α-MoC_{1-x} and the data points in

color red is the results for β-Mo_2C. The hollow symbols stand for the data points for the bare supports, and the solid symbols represent the data points for the supported 1.0 ML Cu catalysts..... 124

Figure 5.9 Selectivity of (a) α-MoC_{1-x} and β-Mo_2C (b)1.0 ML Cu/α-MoC_{1-x}, and 1.0 ML Cu/β-Mo_2C as a function of acetaldehyde partial pressure. The partial pressure of water was kept at a constant of 0.15 atm. The data was collected during the pseudo-steady-state regime at 240 °C..... 124

Figure 5.10 Reaction rates (a) AWS reaction, (b) Cannizzaro reaction, and (c) aldol condensation as a function of water partial pressure. The partial pressure of water was kept at a constant of 0.15 atm. The data was collected during the pseudo-steady-state regime at 240 °C. The data points in color blue is the results for α-MoC_{1-x} and the data points in color red is the results for β-Mo_2C. The hollow symbols stand for the data points for the bare supports, and the solid symbols represent the data points for the supported 1.0 ML Cu catalysts..... 125

Figure 5.11 Selectivity of (a) α-MoC_{1-x} and β-Mo_2C (b)1.0 ML Cu/α-MoC_{1-x}, and 1.0 ML Cu/β-Mo_2C as a function of water partial pressure. The partial pressure of water was kept at a constant of 0.15 atm. The data was collected during the pseudo-steady-state regime at 240 °C..... 125

Abstract

The conversion of biomass into fuels and chemicals is considered as sustainable alternatives of non-renewable fossil fuel and petroleum. Given the high water content in biomass, biomass conversion with water has also drawn increasing attention. The present research investigates the aldehyde water shift (AWS) reaction as a model reaction, in which acetaldehyde is oxidized by water and converted into acetic acid and hydrogen. Inspired by cascade catalytic systems reported for homogeneous catalysts and the bifunctional mechanism reported for the water gas shift reaction, we proposed that high AWS activities could be achieved for catalysts with highly dispersed sites for water dissociation and aldehyde oxidation that are in close proximity. With the hypothesis, we designed a series of oxide- and molybdenum carbide-supported metal catalysts and examined their physical/chemical properties and reactivity, aiming to understand the structure-function relationship. The respective roles of the support and the admetal in AWS, characters of active sites, and kinetic models are also elucidated.

In the research, catalysts were prepared via incipient wetness impregnation and wet impregnation. Physisorption/chemisorption, x-ray diffraction, temperature programmed desorption, and other experiments were implemented to access the structural and surface characteristics. For oxide-supported metal catalysts, we highlight the importance of support reducibility and admetal selection. Supported Cu catalysts had ~4 times higher areal rate than those for supported Pt and Au catalysts. The combination of Cu and ceria yielded the highest AWS activity, and had a turnover frequency that was 8-fold higher than that for the bulk Cu. For the mix-phase molybdenum carbide-based catalysts, the bare carbide outperformed oxide supported

Cu catalysts with a 2-fold or higher AWS rates, and its activity was enhanced by 100% upon 1.0ML Cu deposition. When increasing the Cu loading on the carbide, AWS rates of Cu predicted by the perimeter model agreed well with the experimental results. This suggests that Cu-carbide interfacial sites play a key role in catalyzing the reaction. These results of ceria and carbide supported Cu catalysts are consistent with the bifunctional mechanism hypothesis, in which water dissociation on the reducible oxide and carbide support is coupled with aldehyde oxidation on Cu admetal. The structure of carbide was also determined to be important to its reactivity. The hexagonal carbide showed a ~130% higher AWS rate than that of the cubic carbide. For all carbide-based catalysts, the AWS reaction appeared to be limited by the surface reaction between the adsorbed water and adsorbed acetaldehyde.

As metal oxide and carbide-based catalysts showed significant differences in selectivity, characteristics driving the selectivity were also investigated. For oxide-based catalysts, crotonaldehyde was produced as the major side product via aldol condensation. The rates of aldol condensation were found to correlate well with the weak acid site densities, implying that acid sites can be responsible for the crotonaldehyde formation. For carbide-based catalysts, ethanol produced via Cannizzaro reaction was found to be the major side product. The rates of Cannizzaro reaction were a strong function of acid site densities of carbide catalysts, indicating that the Cannizzaro reaction could be catalyzed by acid sites. This research establishes a groundwork for using supported metal catalyst and will help guide the development of future AWS catalysts.

Chapter 1

Introductions

1.1 Motivation

Fossil fuel and petrochemical products are pervasive in modern society. In 2013, 513.4 Mt/yr of fossil fuel feedstocks and 162.6 Mt/yr of refinery feedstocks were consumed and converted into 820.3 Mt/yr of chemical products, as shown in Figure 1.1. Among the fossil fuel feedstock consumed, 62% was fed through steam crackers to produce ethane/ethylene and propylene from light feed unit while aromatics and olefins were produced from the heavy feed unit. These intermediates were then converted into 329.4 Mt/yr of thermoplastics, thermosets, fiber, and elastomers. The copious amount of chemical consumption indicates that our society relies heavily on petrochemical products [1].

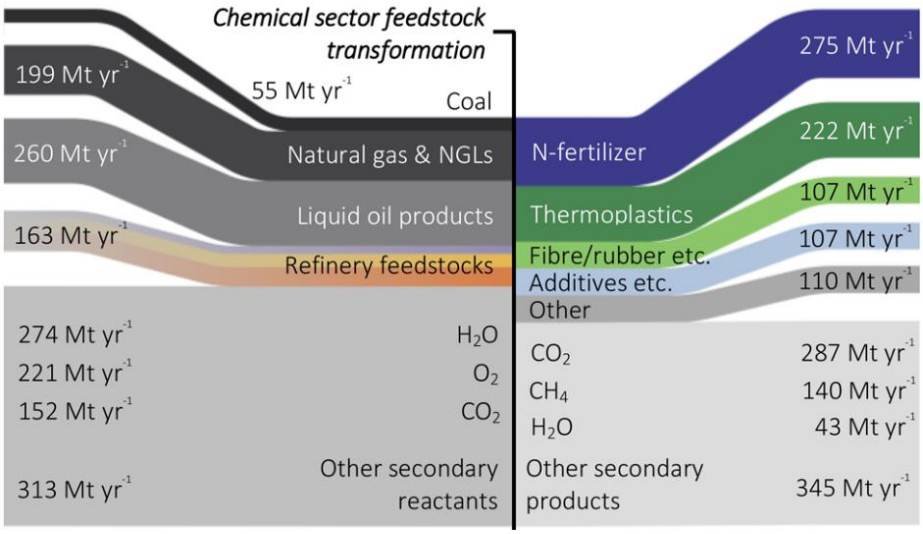

Figure 1.1 A Sankey diagram depicting the passage from fossil fuel feedstocks to chemical products sector for 2013. NGLs: Natural gas liquids, N-fertilizers: Nitrogenous fertilizers. Figure adapted from [1].

Despite the high demands for these products, petroleum and fossil fuel are not renewable resources. An estimation from 2010 indicates that crude oil and natural gas reserves are expected to be depleted in 42 years and 63 years, respectively [2]. Given that petroleum and fossil fuel sources are not environmentally and economically sustainable, tremendous efforts have been established to seek and implement substitutes from alternative and renewable sources [3]. Among the possible solutions, biomass has received the most attention due as the resource could be inexhaustible in principle [2,4]. While the conversion of biomass into chemicals and fuel has a long history, more serious efforts have been dedicated to investigating efficient productions of fuel and value-added chemicals from biomass in order to reduce our dependence on petrochemicals in recent years [3,5].

1.1.1 Production of Chemicals from Biomass-Derivatives

In 2009, the U.S. Department of Energy (DOE) published a report screening promising biorefinery products that have great potential to serve as economic drivers. The selection process reviewed existing petrochemical model of common building blocks and the prior industry experience of the team at Pacific Northwest National Laboratory (PNNL) and National Renewable Energy Laboratory (NREL) [6]. Specifically, criteria used in the review process include: (1) competition against existing petrochemical products; (2) new and improved properties for replacement of existing functionality and applications; (3) basis for a diverse portfolio of products from a single intermediate. From the initial screening, DOE identified nearly 50 bio-derived chemicals that have great potentials to be used as reagents, building blocks, or intermediates. These selected chemicals include acetaldehyde, acetic acid, ethanol, furfural, and other C1-C6 chemicals. Top 30 candidates were down-selected based on their chemical functionality, and the most

versatile 12 sugar-derived building blocks that could be produced from both lignocellulosics and starch, were further identified. The Top 30 and the Final 12 are shown in Table 1.1 [6].

Table 1.1 Thirty bio-derivatives that has top potentials for the use of building blocks. The final twelve sugar-derived building blocks are marked in bold. In the final twelve, succinic acid, fumaric acid, and malic acid were categorized as 1,4 diacids. Adapted from [6].

Carbon Number	Potential Top 30 candidates
1	Carbon monoxide & hydrogen (syngas)
3	**Glycerol**, **3-hydroxypropionic acid (3-HPA)**, lactic acid, malonic acid, propionic acid, serine
4	Acetoin, **aspartic acid**, **fumaric acid**, **3-hydroxybutyrolactone (3-HBL)**, **malic acid**, **succinic acid**, threonine
5	**Arabinitol/xylitol**, furfural, **glutamic acid**, **itaconic acid**, **levulinic acid**, proline, xylonic acid
6	Aconitic acid, citric acid, **2,5-furan dicarboxylic acid (FDCA)**, **glucaric acid**, lysine, levoglucosan, **sorbitol**

Many of the Final 12 bio-derivatives selected are produced via the fermentation of enzymatic conversion processes (e.g. 1,4-diacids, aspartic acid, glutamic acid, and itaconic acid). Only a few can be produced via catalytic processes [6], such as 2,5-furan dicarboxylic acid (FDCA). As FDCA can be used as a building block for polyethylene terephthalate (PET) and polybutyleneterephthalate (PBT), which are highly valued in chemical markets [6], the production of FDCA from 5-hydroxymethylfurfural (HMF) oxidation has been extensively studied (Figure 1.2) [7].

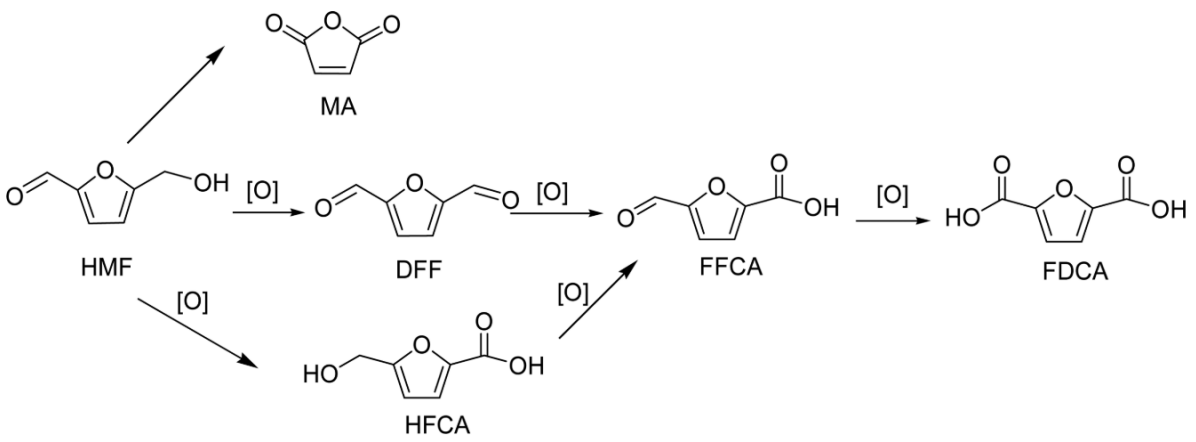

Figure 1.2 Schematic illustration of the potential oxidation products from 5-Hydroxymethylfurfural (HMF). Reaction intermediates include maleic anhydride (MA), 2,5-diformylfuran (DFF), 5-hydrox- ymethyl-2-furancarboxylic acid (HFCA), 2-formyl-5-furancar-boxylic acid (FFCA), and 2,5-furan dicarboxylic acid (FDCA). Adapted from [7].

To realize the production of chemicals, catalysts play essential roles in accelerating the reaction. In the early 1900's, Wilhelm Ostwald first defined catalysts as "a substance which affects the rate of a chemical reaction without being part of its end products" [8]. With the implementation of supported metal catalysts, the oxidation reaction shifted from using nitric acid as an oxidant [3]. Currently, the oxidation of HMF to produce FDCA takes place in basic aqueous solution with a partial pressure of O_2 (0.5 – 10 atm) as an oxidant at moderate temperatures (25 to 100 °C). Common catalysts selected for this reaction include supported noble metal catalysts (e.g. Pt, Au, and Pd), many of which have reported over 95% yields to FDCA [7]. In the oxidation reaction, it is reported that the noble metal dissociates molecular oxygen to oxidize the HMF [9]. In 2012, Davis et al. reported that H_2O could be a source of oxygen during oxidation in a basic solution via the formation of hydroxyl groups (OH^-). In such a mechanism involving water, it was proposed that O_2 played an indirect role in regenerating OH^- as the principal oxidant on the catalyst surface [10,11]. In addition to the thermocatalytic process, H. Cha and K. Choi explored the nature of this oxidation process using a photoelectrochemical cell [12]. They reported the oxidation of HMF to FDCA using 2,2,6,6-tetramethylpiperidine 1-oxyl (TEMPO) as a redox mediator at the anode, and

the reduction of H_2O to H_2 at the cathode. The half-cell reactions are illustrated below; the overall reaction oxidizes HMF with water and produces FDCA and hydrogen.

$$\text{Anode: } \mathrm{HMF} + 6\mathrm{OH}^- \rightarrow \mathrm{FDCA} + 6\mathrm{e}^-$$

$$\text{Cathode: } 6\mathrm{H_2O} + 6\mathrm{e}^- \rightarrow 3\mathrm{H_2} + 6\mathrm{OH}^-$$

$$\text{Overall Reaction: } \mathrm{HMF} + \mathrm{H_2O} \rightarrow \mathrm{FDCA} + 3\mathrm{H_2}$$

1.1.2 The Use of Water as Oxidant for Hydrogen Production

With promising reports from Davis et al. and Cha and Choi, the potential of using water as an oxidant for conversions of biomass feedstock was demonstrated. Given the high water content in biomass, water could be an ideal terminate oxidant and an attractive alternative to gaseous oxygen for oxidation reactions since it allows for finer control of partial oxidation reactions. Additionally, the reaction involving water as oxidant includes the production of hydrogen, an important chemical reagent and fuel. To date, investigations of using water as an oxidant for biomass-derivative conversions are mostly limited to light hydrocarbons [13]. In steam reforming, hydrocarbons or oxygenate constituents oxidized by water and converted into carbon monoxide and hydrogen (CO + H_2, syngas) [14]. Among the reactions, steam reforming of ethanol has received the most attention [15,16]. Another famous reaction using water as an oxidant is the water gas shift (WGS) reaction, which converts water and carbon monoxide to hydrogen and carbon dioxide.

$$\text{Steam Reforming of Ethanol: } \mathrm{CH_3CH_2OH} + \mathrm{H_2O} \rightarrow 2\mathrm{CO} + 3\mathrm{H_2}$$

$$\text{Water Gas Shift Reaction: } \mathrm{CO} + \mathrm{H_2O} \rightarrow \mathrm{CO} + \mathrm{H_2}$$

In industrial settings, WGS and steam reforming reactors are typically installed after the gasification process to remove hydrocarbon products and to generate a cleaner stream of hydrogen and carbon dioxide. The purified hydrogen stream can be used for numerous industrial processes,

including ammonia synthesis, hydrocracking, and Fischer-Tropsch synthesis. Among these chemical processes involving hydrogen, ammonia synthesis is perhaps the most important application (See process scheme in Figure 1.3) [17].

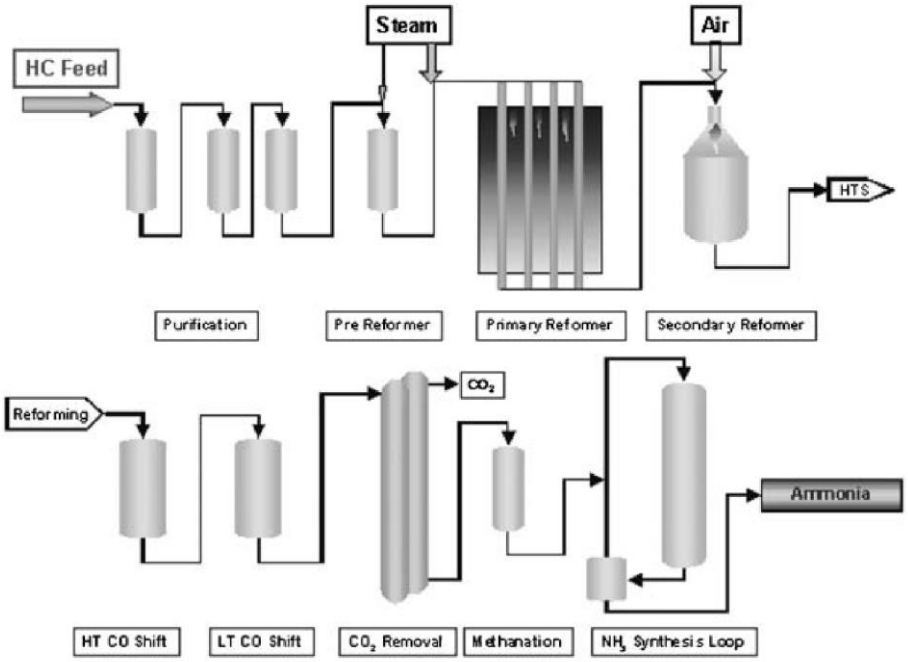

Figure 1.3 Syngas generation and water gas shift reactors for ammonia synthesis. HC= hydrocarbon, HTS= high temperature shift. Adapted from [17].

In recent decades, research on the WGS reaction and steam reforming has diverted to applications in fuel cells, a technology that uses hydrogen to generate electricity and produce water as "waste". With this technology, hydrogen is considered as one of the most promising energy solutions to combat global climate change and to achieve a sustainable future [18]. Theoretically, hydrogen has a gravimetric energy density of 143 MJ/kg, which is up to three times that of gasoline fuels and biodiesel (Table 1.2) [19]. In a polymer electrolyte membrane (PEM) fuel cell, the electrical efficiency can be as high as 60% when using a direct hydrogen source. With high energy density and efficiency, PEM hydrogen fuel cell technology is considered as the most promising technology for light-duty transportation [20].

Table 1.2 Gravimetric and volumetric energy densities of common fuels. Adapted from [19].

Catalysts	Energy per mass (MJ/kg)	Energy per volume (MJ/L)
Hydrogen (liquid)	143	10.1
Hydrogen (compressed, 700 bar)	143	5.6
Hydrogen (ambient pressure)	143	0.0107
Methane (ambient pressure)	55.6	0.0378
Natural gas (liquid)	53.6	22.2
Natural gas (compressed, 250 bar)	53.6	9
Natural gas	53.6	0.0364
LPG propane	49.6	25.3
LPG butane	49.1	27.7
Gasoline (petrol)	46.4	34.2
Biodiesel oil	42.2	33
Diesel	45.4	34.6

Among ways to produce hydrogen, hydrogen production from bio-derived liquids was identified as one of the promising sustainable energy solutions by the DOE (Figure 1.4), especially for hydrogen production at or near the site of use. The DOE anticipates the technology to be economically viable (<$4/kg) in the near future.

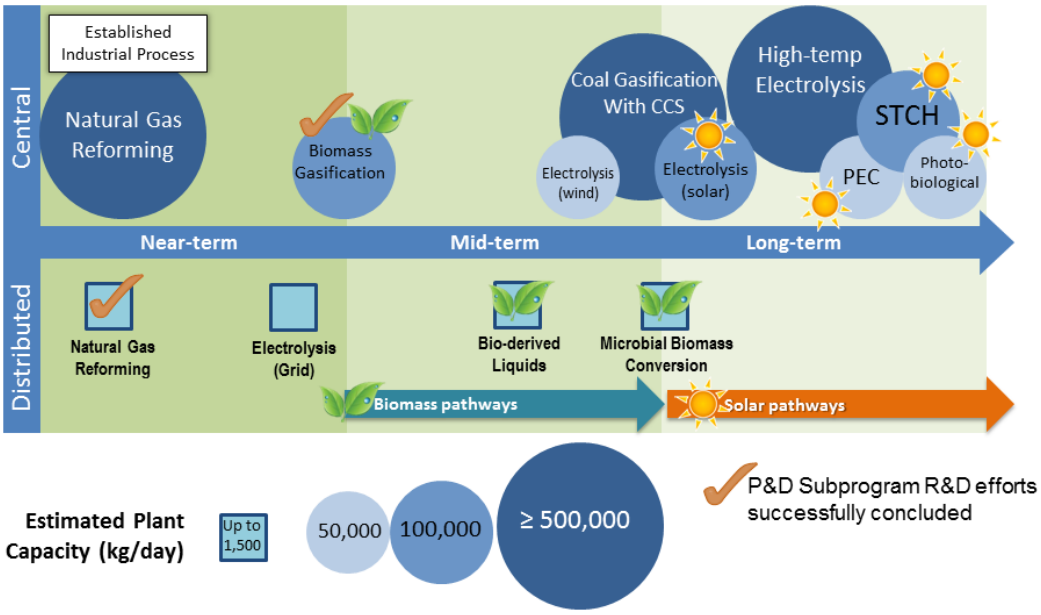

Figure 1.4 Hydrogen production pathways developed by Office of Energy Efficiency and Renewable Energy, U.S. Department of Energy. Central: produce at large facilities and then delivered to the point of use. Distributed: produce at or near the site of use in. Taken from [21].

Nevertheless, as discussed earlier, research using water for biomass oxidation has primarily focused on the steam reforming [17,22], which is typically coupled with the WGS to increase the H_2 yield. While CO_2 produced via complete oxidation of hydrocarbon is not a useful chemical, using water for partial oxidation and the production of commodity chemicals along with hydrogen could be beneficial and warrants more attention. To explore the potential of such type of reaction pathway and expand our knowledge in this area, the research described in this dissertation will focus on investigating a model reaction that partially oxidizes aldehyde with water, the aldehyde water shift (AWS) reaction.

1.2 Aldehyde Water Shift Reaction

In AWS reaction, aldehyde is oxidized by water and converted into corresponding carboxylic acid and hydrogen. A general reaction equation of AWS is shown below. This reaction resembles WGS reaction and steam forming, and the "aldehyde water shift" was designated due to its

similarity to WGS reaction [23]. In the reaction, aldehyde reactants are common constituents in water-laden biomass-derived feedstocks [24,25]; water is a mild oxidant and an attractive alternative to gaseous oxygen.

General Aldehyde Water Shift Reaction: $RCHO + H_2O \rightarrow RCOOH + H_2$

AWS reaction, in comparison to the extensively studied WGS, is a relatively new area of research. To date, the majority of the catalyst studies for AWS have utilized homogenous complexes. Murahashi et al. first demonstrated the AWS reaction in 1987 using a ruthenium catalyst in the presence of benzalacetone as hydrogen acceptors [26]. In 2004, Stanley et al. reported that carboxylic acid was a side product of the hydroformylation reaction when using a dirhodium tetraphosphine catalyst. Using alkene as the starting molecule, the aldehyde produced would further react with water to form heptatonic acid in the presence of catalyst [27]. More recently in 2014, Brewster and co-workers developed a series of half-sandwich cyclopentadienyl Ir, Rh, and Ru complexes for the AWS (Figure 1.5). They evaluated their activities for the AWS of alkyl and aromatic aldehydes and discussed the effects of varying the metal center, which the iridium complexes had the highest conversions and selectivities based of a stable reaction intermediates formed [23]. Brewster et al. later on evaluated Ru diamine complexes, and reported acetaldehyde to acetic acid selectivity (via AWS and Cannizzaro reactions) in excess of 85% at 105 °C [28].

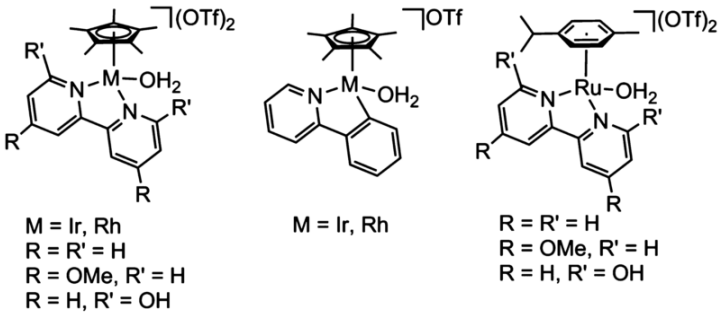

Figure 1.5 Half-sandwich complexes of Ir, Rh, and Ru. Adapted from [23].

Despite high selectivity, the use of homogeneous catalysts for commercial processes is often cost prohibitive [29]. Unlike homogeneous complexes, heterogeneous catalysts offer numerous advantages including lower cost, facile product and catalyst separation, and improved thermal stabilities. Consequently, heterogeneous catalysts provide a more economically viable option for industrial applications [29,30].

In 2016, Orozco et al. reported the conversion of aldehydes to carboxylic acids as a reaction step during the ketonization of heptanal using heterogeneous catalysts [31]. Based on isotopic and kinetic studies with the m-ZrO_2 catalyst, they confirmed the occurrence of the AWS reaction as part of the overall mechanism. Orozco et al. also investigated the role of CeO_2 on overall ketonization conversion, and proposed that the AWS reaction mechanism involved oxygen vacancies on the CeO_2 [32]. Following the pioneering work of Orozco et al., Xiang et al. reported AWS as a side reaction during ethanol dehydrogenation over CuCr catalysts. By varying the Cu:Cr ratio, they attributed the AWS activity to the presence of surface Cu species [33]. However, beyond these reports, the use of supported metal catalysts for AWS has yet to be explored, and the respective roles of the metal and the support remain ill-defined.

Continuing these pioneering works, the present research further explores the use of supported metal catalysts. The aim of this research is to understand the role of support and admetal, investigate the characteristics of active sites, and elucidate reaction kinetics and mechanisms. In this dissertation, acetaldehyde was selected as the model compound because of its structural simplicity and physical properties, which can be easily operated in a flow system. Using acetaldehyde as the model compound, the resulting product is acetic acid, an important carboxylic acid that has a broad spectrum of applications, including food, dye, polymer, and pharmaceutical

industries [34–36]. For the versatile role of acetic acid, the DOE also selected it as one of the top 47 bio-derived value-added chemicals in 2009 [6]. The reaction equation is shown below.

Aldehyde Water Shift Reaction: $CH_3CHO + H_2O \rightarrow CH_3COOH + H_2$

The AWS reaction, which produces acetic acid from acetaldehyde, also has the potential to complete the current acetic acid production process. In current production processes of acetic acid, oxidation of acetaldehyde with molecular oxygen is one of the major reaction pathways [36,37]. By substituting the molecular oxygen with water, the AWS reaction could potentially be implemented to resemble the current process for acetic acid production. In the AWS reaction, hydrogen is also produced simultaneously as a valuable byproduct which can also be used as a reagent for other reactions (e.g. hydrogenation). This is an economically competitive advantage for implementing the AWS reaction.

Despite the simple structure of the model compound selected (i.e. acetaldehyde) in this research, the knowledge acquired regarding using water for aldehyde oxidation over supported metal catalysts can also provide important insights into other oxidation reactions that use compounds with more complicated structures, such as the oxidation of HMF to FDCA.

1.3 Heterogeneous Catalysts for Oxidation Reactions with Water

As reports of heterogeneous catalysts for the AWS reaction are limited, in this dissertation, the catalyst design was inspired by catalysts for the WGS and steam reforming. By leveraging the knowledge from these reactions that use water as the oxidant, we can investigate the structure-function relationships that influence the catalytic performance for AWS, and further establish conceptual frameworks for AWS catalysts design.

1.3.1 Metal Oxide Supported Metal Catalysts

The WGS catalysis technology has been implemented in industrial processes for decades to remove carbon monoxide generated during the gasification and reforming process and produce hydrogen [38]. While catalyst developments for the large-scale processes are relatively mature (e.g. Fe_2O_3-Cr_2O_3 and Cu-Zn-Al), current research focuses have shifted towards fuel cell application, which requires a compact reactor design [17]. As discussed earlier, the use of hydrogen in fuel cells is one of the most promising sustainable energy solutions. Catalysts that have been extensively investigated for this applications include precious admetals (e.g. Pt, Rh, Ru, Au, and Pd) deposited on reducible oxides (e,g, ceria (CeO_2), titania (TiO_2)) and mixed oxides of ceria (e.g. CeO_2-ZrO_2) [17]. In general, catalysts composed of "reducible" oxide, like TiO_2 and CeO_2, show higher activity than those using "irreducible" supports, like Al_2O_3 or SiO_2 [39]. For the WGS and steam reforming reaction, many attribute the superiority in reactivity of the reducible oxide based catalysts to the oxygen vacancies presenting on the reducible oxide and the strong metal-support interaction [40–42].

On a reducible oxide, oxygen vacancies can be created via reduction of the material, forming cations with lower valences [40]. For instance, by reducing CeO_2 with H_2, the reagent could reduce the surface of CeO_2, remove oxygens through H_2O formations, form anionic vacancies, and result in the reduction of neighboring cations from Ce^{4+} to Ce^{3+} [42]. Aside from H_2, other species (e.g. CO) can also interact with CeO_2 and be oxidized in a similar mechanism. This facile removal of surface oxygen is favored by the high mobility of oxygen in the CeO_2 lattice [42,43]. For other reducible oxides, such as TiO_2 and ZnO, a similar mechanism of oxygen vacancy formation has also been reported [40,44]. The oxygen vacancies formed can then be restored by taking oxygen atoms from the feed reactants, such as the dissociation of H_2O or O_2, and released subsequently to activate an oxidation reaction [45]. The described redox property on reducible

oxide plays a critical role in the overall mechanism of catalyzing WGS reaction and steam reforming [45,46]. By depositing admetals on reducible oxide, the strong metal-support interaction can enhance the redox properties and thus alter the electronic properties of both support and the admetal to enhance the catalyst reactivity [47]. For instance, the presence of Cu admetal on CeO_2 can stabilize and induce oxygen vacancies [48,49]. Meanwhile, additional sites for reactant adsorptions and activations are created on the admetal [50]. Since the reducible support and admetal have unique contributions, the interface sites (e.g. perimeter of admetal particles) are demonstrated to play a critical role during the WGS and steam reforming for various of admetals (e.g. Cu, Pt, Au, and Ir) [47,51–53]. The respective characteristics of reducible oxide and admetal can elucidate a bifunctional mechanism, in which the support facilitates water dissociation and the admetal promote reactant adsorption [15,50,54,55], shown in Figure 1.6. Together, the unique properties of reducible oxide supported metal catalysts lead to superior reactivity for WGS and steam reforming in comparison to irreducible oxide supported metal catalysts.

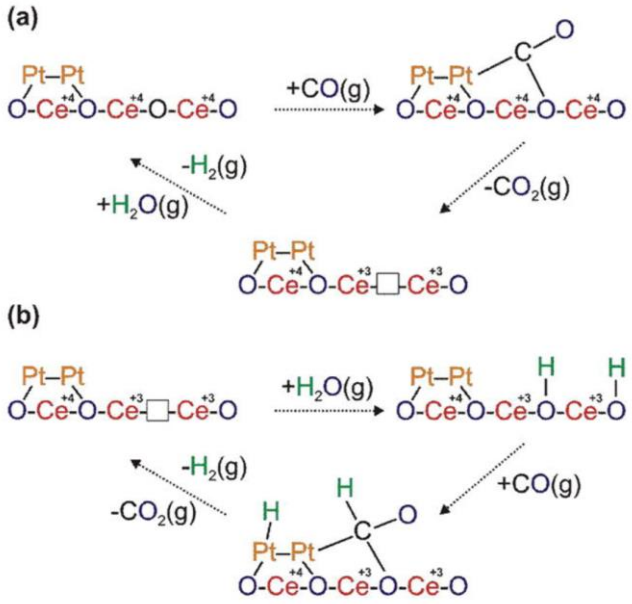

Figure 1.6 Two major reaction mechanisms proposed for WGS on CeO_2-based catalysts: (a) Redox and (b) associative mechanism using Pt/CeO_2 as example. Adapted from [56].

1.3.2 Molybdenum Carbide Supported Metal Catalyst

Continuing the development of supported metal catalysts, the use of molybdenum carbide (Mo_2C) for WGS reaction has drawn significant attention since early 21st century due to its excellent catalytic performance, which is comparable to a commercial WGS reaction catalyst, Cu-Zn-Al [57]. The high reactivity of the Mo_2C is attributed to its unique properties to dissociate water. From DFT calculation, L. Ping and J. Rodriguez reported that the Mo_2C can easily dissociate water, forming surface atomic oxygens and releasing H_2. The surface atomic oxygen can subsequently be used for oxidation (Figure 1.7). With this unique capability, the most active site on Mo_2C can catalyze the WGS reaction a thousand-times faster compared to Cu [58], which is the active metal in Cu-Zn-Al.

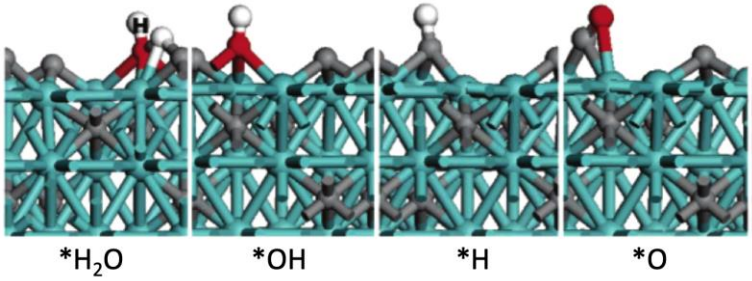

Figure 1.7 Preferential binding geometries calculated for the adsorbates on the C-terminated Mo_2C (001) surface. Taken from [58].

In parallel to the mechanism reported for metal oxide supported metal catalysts, the WGS activity of Mo_2C can be further enhanced by metal deposition. By depositing Pt on Mo_2C, Schweitzer et al. reported a 350% WGS activity enhancement compared to bare Mo_2C and demonstrated that the perimeter site of the Pt particle (e.g. interfacial sites of Pt and Mo_2C) play a key role in catalyzing the reaction. The proposed bifunctional mechanism for Pt/Mo_2C stated that the Pt admetal adsorbs CO while the Mo_2C domain performs H_2O dissociation. An oxidation reaction then takes place at the interface of the Pt and carbide, producing CO_2 and H_2 [39]. Similar conclusions were drawn for other admetals supported on Mo_2C, such as Au, Cu, Pd, and Ni [59].

Aside from WGS, a similar bifunctional mechanism was also reported for steam reforming of methanol and ethanol on Mo_2C supported metal catalysts, which resulted in higher activity after depositing surface metal [60,61].

In addition to the interfacial sites, the metal-support interaction also induces electronic perturbation and contribute to the reactivity of catalysts. Schweitzer et al. discovered a strong interaction between the Pt admetal and the Mo_2C support, resulting in a raft-like 2-dimensional Pt structure on the Mo_2C. When examining the Pt deposited on Mo_2C with X-ray absorption spectroscopy (XAS), the Pt maintained a low coordination number as the loading increased, indicating that the Pt-Mo_2C bonds are more favorable than Pt-Pt bonds (0.9 eV in cohesive energy). This strong interaction resulted in an excellent dispersion of Pt on Mo_2C [39]. With X-ray photoelectron spectroscopy (XPS), Yao et al. reported that the binding energy of Au 4f in 2 wt% Au/α-MoC is about 0.6 eV higher compared to that for the metallic Au. They proposed that the electronic perturbation resulted in a stronger adsorption of CO which explains the high activity of Au/α-MoC compared to α-MoC [62]. Lin et al. also reported a similar electronic perturbation on 2wt% Pt/α-MoC, which the binding energy of Pt $4f_{7/2}$ shifted 0.6 eV higher compared to bulk Pt, resulting in enhanced activity of Pt/MoC for methanol reforming [63]. The unique properties of Mo_2C for water dissociation and the strong interaction between admetal and the Mo_2C support make Mo_2C-supported metal catalysts ideal for oxidation reaction involving water as an oxidant.

Despite the wealth of knowledge regarding the using supported metal catalysts for WGS reaction and steam reforming, little is known about the use of these materials for the AWS reaction. Further studies are necessary to advance our understanding of these reactions using water as an oxidant and producing hydrogen.

1.4 Potential Reaction Pathways and Side Reactions

Under the condition evaluated in this dissertation, there are numerous reactions that could be expected. The potential reactions are shown in Figure 1.8. Reaction #1 is the AWS reaction, which is the desired reaction in this dissertation. Reaction #2 is the Cannizzaro reaction, in which two acetaldehyde molecules react with water [31], forming acetic acid and ethanol. Previously, it was reported that the Cannizzaro reaction could be catalyzed by materials possessing surface acid-base pairs [64], or on metal surfaces with oxygen or hydroxyl groups adsorbed [65]. In Reaction #3, the aldol condensation, a C-C bond forms between two acetaldehyde molecules and crotonaldehyde is produced [66]. Acid sites [66] or acid-base pairs could be responsible for the condensation reaction [67]. In Reaction #4, paraldehyde is produced via trimerization of the acetaldehyde [68]. Reaction #5 is the decarbonylation of acetaldehyde, in which acetaldehyde decomposes into methane and carbon monoxide [69]. Reaction #6 is the reforming of acetaldehyde, which produces carbon monoxide and hydrogen. Experiments determining reaction pathway, selectivity, and speculated reaction mechanisms will be discussed in later chapters.

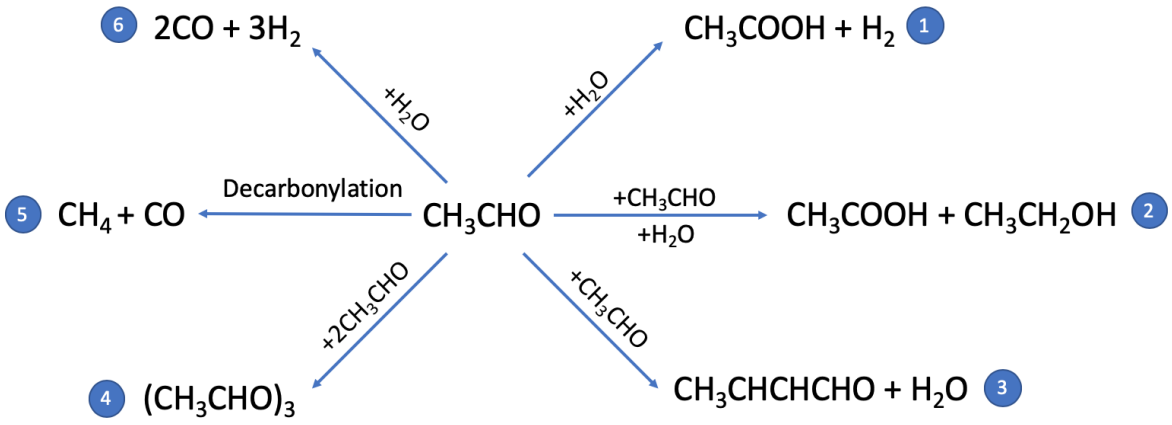

Figure 1.8 Reactions that could potentially occur under the condition employed.

1.5 Research Goals and Organization of the Dissertation

The overall goal of the research described in this dissertation is to elucidate the structure-function relationship for heterogeneous catalysts using H_2O as an oxidant to produce commodity chemicals and fuels from water-laden biomass-derived feedstocks, using the aldehyde water shift (AWS) reaction as the model reaction. Major research objectives were established to achieve this goal:

1. Design supported metal catalysts for the AWS reaction
2. Understand the role of admetal, support, and the synergistic effects
3. Identify characteristics of the active sites for the AWS reaction
4. Elucidate reaction kinetics and mechanism
5. Investigate the factors driving the selectivity

With the research goals and objectives identified, this dissertation is divided into six chapters and outlined as follows.

Chapter 2: AWS with Metal Oxide Supported Metal Catalysts

This chapter explores the potential of using supported metal catalysts for the AWS reaction. A series of metal oxide supported metal catalysts with low admetal loading and benchmark catalysts were evaluated for the AWS to elucidate the role of admetal, support, and synergistic effects. The key hypothesis presented in this chapter is that a bifunctional mechanism could lead to high AWS activity. Trends were observed among admetal, support reducibility, and reactivity of the catalysts. The integration of Cu admetal and reducible oxide was found to play an important role in catalyzing the AWS reaction, which is consistent with the hypothesis. The selectivity and rate of side reactions were found to be correlated with the surface acid sites density.

Chapter 3: AWS with Mo_2C Supported Metal Catalysts

Work performed in this chapter explores the use of Mo_2C-supported metal catalysts for the AWS reaction. The catalyst design was further developed based on the concept of the bifunctional mechanism demonstrated in Chapter 2, in which the Mo_2C was reported to have the sites for both water and aldehyde adsorption. The catalysts were prepared via wet impregnation and with low metal loading. Physical properties and catalytic performance are reported, including surface areas, CO and NH_3 uptake, AWS reaction rates, and selectivity. Mo_2C was found to be a highly active catalyst and support for AWS compared to metal oxides supported metal catalysts. Unlike metal oxides supported metal catalysts, the effects of admetal were relatively trivial when supported on Mo_2C.

Chapter 4: Investigation of Active Sites on Mo_2C Supported Metal Catalysts

To acquire more evidence for the bifunctional mechanism, the research discussed in this chapter investigates the characteristics of the active site for the AWS reaction on Mo_2C supported Cu catalyst. The Cu/Mo_2C catalysts were synthesized via incipient wetness impregnation, and the physical and catalytic properties of Mo_2C catalysts with various Cu loading from 0.1 ML to 2 ML were evaluated. The activity of Mo_2C support and Cu admetal was deconvoluted, and the Cu-Mo_2C interfacial sites were found to be critical to AWS activity, which is consistent with the bifunctional mechanism posited. The characteristics driving the selectivity was also investigated. The Cannizzaro reaction, a major side reaction for Mo_2C-based catalysts, was found to be catalyzed by acid sites. Reaction mechanisms consistent with the findings and the known chemistry of the catalysts were deducted.

Chapter 5: Reaction Kinetics of α-MoC_{1-x} and β-Mo_2C Supported Metal Catalysts

This chapter discusses the uses of α-MoC_{1-x} and β-Mo_2C supported Cu catalysts for the AWS reaction, as we proposed that the structure of the carbide has influence on the properties and

reactivities of catalysts. The research described investigates the physical and catalytic properties of α-MoC_{1-x} and β-Mo_2C which include the PZC of the materials. Extended studies were performed to investigate the reactivity. To validate the mechanism for AWS reaction proposed in Chapter 4, which is speculated to proceed via the Langmuir-Hinshelwood, reaction kinetics modeling experiments was carried out on the α-MoC_{1-x}, β-Mo_2C, and their supported Cu catalysts. The modeling results were not contradictory to the bifunctional mechanism hypothesis.

Chapter 6: Summary and Recommended Future Work

The final chapter summarizes key findings and accomplishments from this research. Based on the findings reported in this dissertation, extensions of the current research and future directions are proposed.

1.6 Reference

[1] P. G. Levi, J. M. Cullen, Environ. Sci. Technol. 52 (2018) 1725–1734.
[2] W. Keim in: M. Bertau, H. Offermanns, L. Plass, F. Schmidt, H. J. Wernicke (Eds.), Methanol: The Basic Chemical and Energy Feedstock of the Future. Springer-Verlag, Berlin Heidelberg, 2014, pp 24.
[3] A. Corma, S. Iborra, A. Velty, Chem. Rev. 107 (2007) 2411–2502.
[4] L. Wu, T. Moteki, A. A. Gokhale, D. W. Flaherty, F. D. Toste, Chem. 1 (2016) 32–58.
[5] M. Chen, P. M. Smith, M. P. Wolcott, Bioproducts Business 1 (2016) 42–59.
[6] T. Werpy, G. Petersen, A. Aden, J. Bozell, J. Holladay, J. While, A. Manheim, D. Elliot, L. Lasure, S. Jones, M. Gerber, K. Ibsen, L. Lumberg, S. Kelly, Top Value Added Chemicals from Biomass I—Results of Screening for Potential Candidates from Sugars and Synthesis Gas, U.S. Department of Energy, 2004
[7] Z. Zhang, K. Deng, ACS Catal. 5 (2015) 6529–6544.
[8] G. Ertl, Angew. Chem. Int. Ed. 47 (2008) 3524–3535.
[9] P. Vinke, H. E. Van Dam, H. Van Bekkun, Stud. Surf. Sci. Catal. 5 (1990) 147–158.
[10] S. E. Davis, B. N. Zope, R. J. Davis, Green Chem. 14 (2012) 143–147.
[11] S. E. Davis, A.D. Benavidez, R.W. Gosselink, J. H. Bitter, K. P. De Jong, A. K. Datye, R. J. Davis, J. Mol. Catal. A: Chem. 388–389 (2014) 123–132.
[12] H. G. Cha, K. Choi, Nat. Chem. 7 (2015) 328–333.
[13] P. K. Cheekatamarla, C. M. Finnerty, J. Power Sources 160 (2006) 490–499.
[14] R.R. Davda, J. W. Shabaker, G.W. Huber, R.D. Cortright, J. A. Dumesic, Appl. Catal., B 56 (2005) 171–186.
[15] T. Hou, S. Zhang, Y. Chen, D. Wang, W. Cai, Renewable Sustainable Energy Rev. 44 (2015) 132–148.
[16] M. Ni, D. Y. C. Leung, M. K. H. Leung, Int. J. Hydrogen Energy. 32 (2007) 3238–3247.

[17] C. Ratnasamy, J. P. Wagner, Catal. Rev. 51 (2009) 325–440.
[18] A. Demirbas, Energy Sources, Part A 38 (2016) 1721–1729.
[19] K. Mazloomi, C. Gomes, Renewable Sustainable Energy Rev. 16 (2012) 3024–3033.
[20] U.S. Department of Energy, FUEL CELL TECHNOLOGIES OFFICE, Fuel Cells, 2015. https://www.energy.gov/sites/prod/files/2015/11/f27/fcto_fuel_cells_fact_sheet.pdf. (Access Nov 18, 2018)
[21] U.S. Department of Energy, FUEL CELL TECHNOLOGIES OFFICE, Hydrogen Production, https://www.energy.gov/eere/fuelcells/hydrogen-production (Access Nov 28, 2018)
[22] A. Iulianelli, P. Ribeirinha, A. Mendes, A. Basile, Renewable Sustainable Energy Rev. 29 (2014) 355–368.
[23] T. P. Brewster, W. C. Ou, J. C. Tran, K. I. Goldberg, S. K. Hanson, T. R. Cundari, D. M. Heinekey, ACS Catal. 4 (2014) 3034–3038.
[24] T. Milne, F. Agblevor, M. Davis, S. Deutch, D. Johnson in: A. V. Bridgwater and D. G. B. Boocock (eds.), Developments in Thermochemical Biomass Conversion, Springer Netherlands, 1997, p. 409–424.
[25] J. Adam, M. Blazsó, E. Mészáros, M. Stöcker, M.H. Nilsen, A. Bouzga, J.E. Hustad, M. Grønli, G. Øye, Fuel 84 (2005) 1494–1502.
[26] S. Murahashi, T. Naota, K. Ito, Y. Maeda, H. Taki, J. Org. Chem. 52 (1987) 4319–4327.
[27] G. G. Stanley, D. A. Aubry, N. Bridges, B. Barker, B. Courtney, ACS Div. Fuel Chem. Prepr. 49 (2004) 712–713.
[28] T. P. Brewster, J. M. Goldberg, J. C. Tran, D. M. Heinekey, K. I. Goldberg, ACS Catal. 6 (2016) 6302–6305.
[29] A.Z. Fadhel, P. Pollet, C.L. Liotta, C.A. Eckert, Molecules. 15 (2010) 8400–8424.
[30] R. A. Sheldon, R. S. Downing, Appl. Catal., A. 189 (1999) 163–183.
[31] L. M. Orozco, M. Renz, A. Corma, ChemSusChem. 9 (2016) 2430–2442.
[32] L. M. Orozco, M. Renz, A. Corma, Green Chem. 19 (2017) 1555–1569.
[33] N. Xiang, P. Xu, N. Ran, T. Ye, RSC Adv. 7 (2017) 38586–38593.
[34] G. Martin, Industrial and manufacturing chemistry, D. Appleton & co., New York, 1920.
[35] F. S. Wagner, Acetic Acid, in: Kirk-Othmer Encyclopedia of Chemical Technology, 3rd ed., John Wiley & Sons, Inc., 2014, pp. 1–21.
[36] H. Cheung, R.S. Tanke, G.P. Torrence, Acetic Acid, in: ULLMANN'S Encyclopedia of Industrial Chemistry, Wiley-VCH Verlag GmbH & Co. KGaA, Weinheim, 2012, pp. 210–238.
[37] K. Sano, H. Uchida, S. Wakabayashi, Catal. Surv. Jpn. 3 (1999) 55–60.
[38] D. S. Newsome, Catal. Rev. -Sci. Eng. 45 (1980) 275-318.
[39] N. M. Schweitzer, J. A. Schaidle, O. K. Ezekoye, X. Pan, S. Linic, L. T. Thompson, J. Am. Chem. Soc. 133 (2011) 2378–2381.
[40] S. J. Tauster, S. C. Fung, R. T. K. Baker, J. A. Horsley, Science 211 (1981) 1121–1125.
[41] X. Y. Shi, W. Zhang, C. Zhang, W. T. Zheng, H. Chen, J. G. Qi, J. Microscopy 262 (2016) 203–215.
[42] A. Trovarelli, Catal. Rev. 38 (1996) 439–520.
[43] W. Liu, M. Flytzani-Stephanopoulos, Chem. Eng. J. 64 (1996) 283-294.
[44] A. Janotti, C. G. Van De Walle, Appl. Phys. Lett. 87 (2005) 1–3.
[45] C. Pojanavaraphan, A. Luengnaruemitchai, E. Gulari, Appl. Catal., A. 456 (2013) 135–143.
[46] J. A. Rodriguez, P. Liu, X. Wang, W. Wen, J. Hanson, J. Hrbek, M. Pérez, J. Evans, Catal.

Today 143 (2009) 45–50.
[47] C. T. Campbell, Nat. Chem. 4 (2012) 597–598.
[48] J. Sun, L. Zhang, C. Ge, C. Tang, L. Dong, Chin. J. Catal. 35 (2014) 1347–1358.
[49] C. G. Maciel, M. N. Belgacem, J. M. Assaf, Catal. Lett. 141 (2011) 316–321.
[50] A. Bruix, J. A. Rodriguez, P. J. Ramírez, S. D. Senanayake, J. Evans, J. B. Park, D. Stacchiola, P. Liu, J. Hrbek, F. Illas, J. Am. Chem. Soc. 134 (2012) 8968–74.
[51] Q. Fu, A. Weber, M. Flytzani-Stephanopoulos, Catal. Lett. 77 (2001) 87–95.
[52] J. A. Rodriguez, D. C. Grinter, Z. Liu, R. M. Palomino, S. D. Senanayake, Chem. Soc. Rev. 46 (2017) 1824–1841.
[53] J. A. Rodriguez, S. D. Senanayake, D. Stacchiola, P. Liu, J. Hrbek, Acc. Chem. Res. 47 (2014) 773–782.
[54] J. A. Rodriguez, P. Liu, J. Hrbek, J. Evans, M. Pérez, Angew. Chem. 119 (2007) 1351–1354.
[55] K. G. Azzam, I. V. Babich, K. Seshan, L. Lefferts, J. Catal. 251 (2007) 153–162.
[56] C. M. Kalamaras, S. Americanou, A. M. Efstathiou, J. Catal. 279 (2011) 287–300.
[57] J. Patt, D.J. Moon, C. Phillips, L. Thompson, Catal. Lett. 65 (2000) 193–195.
[58] P. Liu, J. A. Rodriguez, Phys. Chem. B. 110 (2006) 19418–19425.
[59] K. D. Sabnis, Y. Cui, M. C. Akatay, M. Shekhar, W. S. Lee, J. T. Miller, W. N. Delgass, F. H. Ribeiro, J. Catal. 331 (2015) 162–171.
[60] Y. Ma, G. - X. Hao, Z. Zuo, W. Huang, P. Phanthong, K. Kusakabe, A. Abudula, RSC Adv. 4 (2014) 44175–44184.
[61] J. Cao, Y. Ma, G. Guan, X. Hao, X. Ma, Z. Wang, K. Kusakabe, A. Abudula, Appl. Catal., B 189 (2016) 12–18.
[62] S. Yao, S. Yao, X. Zhang, W. Zhou, R. Gao, W. Xu, Y. Ye, L. Lin, X. Wen, B. Chen, E. Crumlin, J. Guo, Z. Zuo, W. Li, J. Xie, L. Lu, C.J. Kiely, L. Gu, C. Shi, J. A. Rodriguez, D. Ma, Science. 4321 (2017) 1–10.
[63] L. Lin, W. Zhou, R. Gao, S. Yao, X. Zhang, W. Xu, S. Zheng, Z. Jiang, Q. Yu, Y.-W. Li, C. Shi, X.-D. Wen, D. Ma, Nature. 544 (2017) 80–83.
[64] X. D. Peng, M. A. Barteau, Langmuir 5 (1989) 1051–1056.
[65] Wang, X., Catalysis Today (2018), https://doi.org/10.1016/j.cattod.2018.06.021
[66] E. Dumitriu, V. Hulea, I. Fechete, A. Auroux, J.-F. Lacaze, C. Guimon, , Microporous Mesoporous Mater. 43 (2001) 341–359.
[67] M. J. Climent, A. Corma, V. Fornés, R. Guil-Lopez, S. Iborra, , Adv. Synth. Catal. 344 (2002) 1090–1096.
[68] M. Eckert, G. Fleischmann, R. Jira, B.H. M., K. Golka, Acetaldehyde, in: ULLMANN'S Encyclopedia of Industrial Chemistry, Wiley-VCH Verlag GmbH & Co. KGaA, Weinheim, 2012, pp. 192-207.
[69] H. Zhao, J. Kim, B.E. Koel, Surf. Sci. 538 (2003) 147–159.

Chapter 2

AWS with Metal Oxide Supported Metal Catalysts

2.1 Introduction

In this chapter, the use of metal oxide supported metal catalysts for the aldehyde water shift (AWS) reaction was explored. As previously discussed in the First Chapter, Orozco et al. reported the occurrence of AWS reaction as part of ketonization over CeO_2 catalysts, and proposed that the AWS reaction mechanism involved oxygen vacancies on the CeO_2 [1]. Following the work pioneered by Orozco et al., Xiang et al. reported AWS as a side reaction during ethanol dehydrogenation over CuCr catalysts. By varying the Cu:Cr ratio, they attributed the AWS activity to the presence of surface Cu species [2]. However, beyond these reports, there lacks an understanding of effective catalyst design strategies and reaction kinetics; factors influencing selectivity also remain undetermined.

In this Chapter, we describe the AWS activities and selectivities of a series of oxide supported metal catalysts with the goal of understanding the respective roles of the admetal and support, and defining key structure-function relationships. Given that the number of reports for heterogeneous catalysts for AWS is limited, our catalyst design of supported metal catalysts for AWS was inspired by catalysts for the water gas shift (WGS), in which the close proximity of distinct sites for H_2O dissociation and CO oxidation have been reported to improve WGS activity [3–5]. As H_2O is used as oxidant in both AWS and WGS, the two reactions could have a parallel mechanism; we hypothesized that high AWS activities could be achieved for catalysts with intimately dispersed sites for H_2O dissociation and aldehyde oxidation.

A supported metal catalyst typically consists of a support and a surface admetal. In general, catalysts including a "reducible" support, such as CeO_2 and TiO_2, were more active than catalysts utilizing "irreducible" support [6]. In the WGS reaction on a reducible support, the oxygen vacancies on the surface facilitate water dissociation, CO then reacts with oxygen directly or indirectly from the oxygen released from the dissociation of water (via, for example, a Mars-Van Krevelen-type mechanism) [7–9]. By depositing a surface metal on the reducible support, additional catalytic sites are created. The metal-support interface has been reported to be critical for numerous reactions, including WGS, that the intimacy between sites on the admetal and the support lead to higher activity. Specifically, for the WGS, the admetal could create sites for CO adsorption and support is responsible for water dissociation [10–12]. Some also attribute the enhanced activity to the synergetic effects induced by the strong metal-support interaction, which induces surface electronic perturbations and create special sites at the perimeter of the metal particles [13–16]. In contrast, for an irreducible support such as Al_2O_3 and SiO_2, the support serves only as the media to improve dispersion for depositing a metal catalyst.

For WGS, CeO_2-supported Cu, Pt, and Au catalysts have been reported to be outstanding catalysts and outperform a commercial Cu-Zn-Al catalysts [5,6,17,18]. In the case of WGS over Au/CeO_2, Q. Fu and co-workers attributed its high activity to a bifunctional mechanism in which H_2O dissociation is catalyzed by CeO_2 and CO oxidation by the Au domains [3]. Rodriguez et al. drew a similar conclusion for CeO_2 supported Cu catalysts [4]. For WGS over Cu/CeO_2, synergistic effects have also been reported, such as that the strong interaction between $Cu\text{-}CeO_2$ can stabilize and induce the oxygen vacancies on CeO_2, which could dissociate water and lead to higher reactivity [4,7,19]. Azzam et al. also reported Pt/CeO_2 to be excellent WGS catalyst, and attribute the high performance to its bifunctionality and intimacy between sites for CO adsorption

on Pt and H_2O dissociation on CeO_2 (see Figure 2.1) [9]. In a computational study, Bruix et al. demonstrated that the Pt admetal on CeO_2 was able to dissociate water during the WGS reaction [5], in contrast to Au/CeO_2 and Cu/CeO_2, for which water dissociation took place mostly on the CeO_2 support or at the metal-support interface [4,5]. These attributes make Pt/CeO_2 a more effective WGS catalyst compared to Au/CeO_2 and Cu/CeO_2.

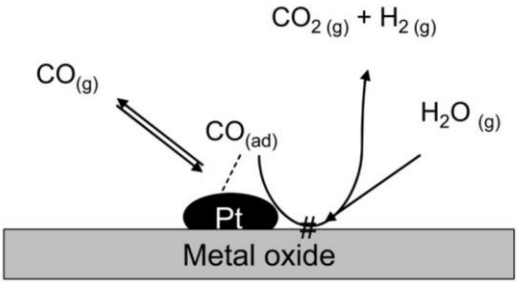

Figure 2.1 The role of metal and support in WGS reaction sequence; Pt/CeO_2 as example. Figure adopted from [9].

As H_2O is used as an oxidant in both WGS and AWS, the two reactions could share similar mechanisms. Leveraging knowledge and conceptual frameworks from WGS catalyst design, our catalyst selection for AWS in this chapter includes CeO_2 and Al_2O_3 supported Cu, Pt, and Au (=M). In particular, CeO_2 is a reducible oxide that is capable of H_2O dissociation [1,4,9] and an admetal could potentially provide sites for aldehyde adsorption and partial oxidization (as shown in Figure 2.2) [2,20–23]. Per our hypothesis of the bifunctional mechanism, we expect CeO_2-supported metal catalysts to be highly active for AWS. Al_2O_3, an irreducible and acidic oxide [6,24], was selected to assess the effect of support reducibility and acidity on AWS. As it was reported that aldehyde adsorption could take place on acid sites via the oxygen lone pair [25], we speculated that the surface acidity could correlate with the selectivity. The impact of the support on reactivity was further investigated by evaluating the performance of bulk Cu nanoparticles, a commercial Cu-Zn-Al WGS catalyst, and Cu/SiO_2 along with the Cu/CeO_2 and Cu/Al_2O_3. SiO_2 is

relatively inert compared to CeO_2 and Al_2O_3, and is expected to be catalytically inactive for the AWS reaction [26].

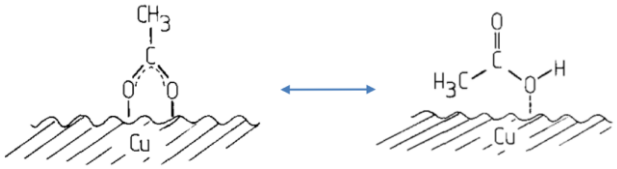

Figure 2.2 Schematic of acetaldehyde adsorption on Cu surface with the presence of surface oxygen. Adopted from [21].

In summary, the primary objectives of the research described in the Chapter are: (1) evaluate the effect of Cu, Pt, and Au admetal promoters on both reducible and irreducible supports, including CeO_2 and Al_2O_3, and (2) identify the catalyst characteristics that lead to high AWS activity, particularly those pertaining to synergistic support-admetal interactions. The findings of this chapter could also be used as a guideline for future catalyst design.

2.2 Experimental Methods

2.2.1 Catalyst Synthesis

The CeO_2-, Al_2O_3, and SiO_2-supported metal catalysts were prepared via an incipient wetness impregnation method as previously described [6]. In this chapter, the nominal surface coverages of metals were 0.1 monolayers (ML) based on 10^{19} site/m^2. The CeO_2 (Sigma-Aldrich), γ-Al_2O_3 (Alfa Aesar), and SiO_2 (AEROSIL®) particles were pelletized, crushed, and sieved to obtain the particles with the size between 125 and 250 μm. The metal oxides were calcined in air at 500 °C for 10 hours prior to metal deposition. Appropriate amounts of metal precursor were dissolved in a quantity of water sufficient to fill the pore volume of the support as determined by N_2 physisorption. Chloroplatinic acid hexahydrate ($H_2PtCl_6 \cdot 6H_2O$, Sigma-Aldrich), copper (II) nitrate hydrate ($Cu(NO_3)_2 \cdot 3H_2O$, Sigma-Aldrich) and gold (III) chloride trihydrate ($HAuCl_4 \cdot 3H_2O$, Sigma-Aldrich) were used as precursors for Pt, Cu, and Au deposition,

respectively. The solution was added to the support in aliquots using a pipet until the solution was fully absorbed by the support. The material was subsequently dried in a vacuum oven at 110 °C overnight, and finally calcined in air for 5 hours. The Pt-based catalysts were calcined at 450 °C; the Au- and Cu-based catalysts were calcined at 300 °C. Commercially available Cu-Zn-Al (Süd-Chemie/Clariant) was acquired and used as a benchmark catalyst for this study. Cu nanoparticles (QuantumSphere) was also acquired and evaluated to investigate the importance of the supports.

2.2.2 Materials Characterization

2.2.2.1 X-ray Diffraction

The crystalline phases and average crystallite sizes were determined by X-ray diffraction (XRD) using a Rigaku Miniflex equipped with a Cu Kα (λ = 0.15404 nm) radiation source and a Ni filter. The catalyst samples were crushed and loaded on a zero-background sample holder. All data was collected with a scan rate of 5°/min with a step size of 0.1° over a 2θ ranging from 10 to 90°. The obtained XRD patterns were analyzed using the JADE software to identify the phase purity of synthesized materials by comparing with the standard patterns in the International Centre for Diffraction Database built-in library and the reports in the literature.

2.2.2.2 N_2 Physisorption Analysis

The surface area of materials was determined by N_2 physisorption isotherm and Brunauer-Emmett-Teller (BET) method using a Micromeritics ASAP 2020 instrument. Approximately 100 mg of catalyst was first loaded into the BET quartz tube, and was degassed at 350 °C for 5 hours under vacuum (<5 mm Hg). Upon the completion of the degas, the weight of the degassed sample was recorded, and the tube was transferred to the analysis port. The sample was then exposed to different N_2 partial pressures relative to the saturation pressure, and the amounts of N_2 adsorbed and desorbed were monitored.

2.2.2.3 Active Site Density Measurement

The active site densities were determined using a Micromeritics ASAP 2920 instrument. For Pt- and Au-based catalysts, the site densities were determined via CO chemisorption; N_2O chemisorption was used to probe the site densities for Cu-based catalysts. In each measurement, approximately 100 mg of catalyst was loaded into a u-shape chemisorption reactor, supported by quartz wool added before the sample. Prior to the chemisorption analysis, the catalysts were pretreated under the same conditions used prior to AWS reactions described in this work. In particular, Pt-based catalysts were pretreated with 10% H_2/N_2 (Cryogenic Gases) at 300 °C for 1 hour [6]; Cu- and Au-based catalysts were pretreated with 4% H_2/N_2 at 200 °C (100 mL/min, Cryogenic Gases) for 4 hours [17,27]. Following the pretreatment, the materials were degassed with He at 10 °C higher than the pretreatment temperature for 0.5 hours and cooled to 40 °C to perform the chemisorption.

In CO chemisorption experiments, the catalysts were dosed with pulses of 5% CO/He; the exposure was repeated until reaching saturation, at which point the active site densities were determined [6]. In N_2O chemisorption experiments, the samples were exposed to a flowing mixture of 10% N_2O/He (Cryogenic Gases) for 2 hours. After the N_2O treatment, the materials were purged with He to remove excessive N_2O. An H_2 temperature-programmed reduction (TPR) was then conducted with the temperature increasing from 40 to 500 °C in 4% H_2/Ar (Cryogenic Gases) at a ramp rate of 10 °C/min. The active site density was calculated based on the H_2 consumed during the TPR [27].

2.2.2.4 NH_3 chemisorption and temperature program desorption

The NH_3 chemisorption technique was applied to probe the surface acid character using a Micromeritics ASAP 2920 instrument [28]. The catalysts were pretreated, degassed, and cooled to

40 °C as described in the active sites density measurement before exposure to NH_3. The sample was then saturated with anhydrous NH_3 (Cryogenic Gases) for 1 hour. The physisorbed/excess amount of NH_3 was removed by purging the sample in flowing He for 30 min. The sample temperature was then heated from 40 °C to 800 °C at a ramp rate of 10 °C/min. The desorbed gases were monitored using a ThermoStar GSD 300 mass spectrometer, which continuously sampled the post-reactor stream on the 2920.

2.2.3 Reaction Rate and Selectivity Measurements

In catalyst evaluations, 25 mg of Cu-Zn-Al, 40 mg of Nano-Cu, 50 mg of the CeO_2-supported catalysts, 75 mg of the Al_2O_3-supported catalysts, and 40 mg of the SiO_2-supported catalysts were used for the reaction measurements. The catalysts amounts were chosen to maintain similar conversions, meanwhile limited by the volume of the catalyst bed. The catalyst was loaded into a quartz flow-through reactor, and the catalyst bed was diluted with low surface area SiO_2 (Alfa Aesar) to maintain the same bed height and volume for all the experiments. The quartz reactor was mounted onto the reactor with ultra-torr fittings and quarter-inch Kalrez o-rings.

Prior to reactions, Pt-based catalysts were pretreated with 10% H_2/N_2 (100 mL/min, Cryogenic Gases) at 300 °C for 1 hour [6]; Cu and Au catalysts were pretreated with 4% H_2/N_2 (100 mL/min, Cryogenic Gases) at 200 °C for 4 hours [17,27]. The activity measurements were carried out at 200-300 °C and approximately 2.5 psig using a gas space velocity of 5,600 h^{-1}. The temperature range used is typical for the low-temperature WGS [29], and much lower than those in prior reports describing evidence for the AWS reaction over heterogeneous catalysts [1,2,30]. The reactant stream consisted of 9% acetaldehyde, 15% H_2O and 76% N_2. A N_2 stream (Cryogenic Gases) was saturated with acetaldehyde using two bubblers in series at 9 °C and 2.5 psig. Acetaldehyde (99.5% Extra Pure, ACROS Organics) was loaded in the first bubbler to saturate the

N_2 stream, and the second bubbler was installed to prevent over-saturation. The acetaldehyde-saturated stream was then diluted with another stream of N_2. Ultra-pure water was used as the water source, and the water was continuously purged with N_2 during the entire period of the experiment to keep the system deaerated. Ultra-pure water was injected via an HPLC pump and vaporized in the chamber prior to entering the system. Finally, the acetaldehyde and steam streams were mixed, and passed through the reactor in the furnace.

The post-reaction effluent was passed through a condenser to separate the gas and liquid phases due to the low water tolerance of the equipped gas chromatography detector. A round flask soaked in the ice bath was used to collect the condensed liquid products. The production of H_2 and other gas phase species were monitored using an SRI 8610C gas chromatograph with a thermal conductivity detector (GC-TCD), using a Supelco Carboxen 1000 packed column to separate gases and flowing ultra-high purity Ar (Cryogenic Gases) as the reference gas. Compositions of the liquid products were collected and analyzed post reaction using a Varian 450-GC gas chromatograph with flame ionization detector (FID), using a DB-WAX capillary column for product separation and ultra-high purity He (Cryogenic Gases) as the carrier gas. The composition was calculated based on the peak areas obtained in the GC trace and compared the peak area with calibration runs of samples with known concentration. Rate data was collected during the deactivation and subsequent pseudo-steady state regimes. A scheme diagram of the AWS reactor is shown in Figure 2.3. After each evaluation experiment, the spent catalysts were preserved and sealed under the N_2 environment for post-reaction analysis.

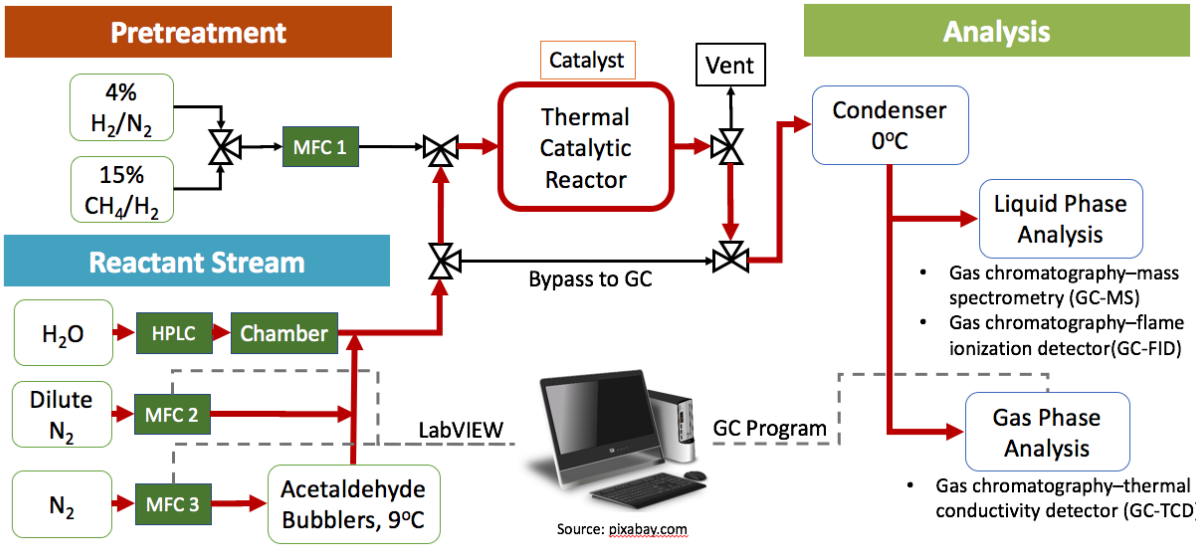

Figure 2.3 Scheme diagram of the AWS reactor. The red line highlight the pathway of a reactant stream during experiment.

For all reactivity measurement experiments, the conversions were kept below 10% to hold differential reaction conditions. The reactant conversions were estimated based on the production rates of the hydrocarbon relative to the initial concentration. Accurate calculation of acetaldehyde conversion was not accessible. With the low boiling points of acetaldehyde (20.2 °C), the condensed aldehyde evaporated continuously. Thus, the measured amounts of acetaldehyde in the GC could not represent the post-reaction composition. Carbon balance was monitor by comparing the moles of carbon fed and the moles of carbon detected in the hydrocarbon products. The selectivity is defined as the moles of acetaldehyde converted to specific hydrocarbon product divided by the total amount of acetaldehyde converted to FID-detectable hydrocarbon products.

2.3 Results

2.3.1 Catalyst Characterization

The surface areas, metal content and chemisorption uptakes for each of the catalysts are listed in Table 2.1. The surface areas did not vary significantly with the supported metal suggesting

that the metals were well dispersed. The surface area for the commercial Cu-Zn-Al catalyst was consistent with that provided in the vendor specifications [27]. Metal loadings for all oxide-supported metal catalysts were calculated based on the concentration of the prepared impregnation solutions and were equivalent to surface coverages of 9-12%, assuming atomic dispersion. CO chemisorption was used to determine the site density of the Pt-based catalyst [6]. Note that CO is not a suitable chemisorbate for the oxide-supported Cu, thus the N_2O chemisorption was used to probe the site density of metal oxide-supported Cu catalysts [31,32].

Table 2.1 Select catalyst surface and physical properties for the catalysts.

Catalysts	Surface Area (m^2/g)	Metal Loading (wt%) [a,b]	CO Uptake (μmol/g)	N_2O Uptake (μmol/g)	NH_3 Uptake (μmol/g)
CeO_2	40	---	0	16[c]	39
Cu/CeO_2	41	0.4	0	471[c]	20
Pt/CeO_2	37	1.0	27	27[d]	57
Au/CeO_2	36	1.0	0	0[d]	98
Al_2O_3	79	---	0	0[c]	67
Cu/Al_2O_3	76	0.8	0	48[c]	87
Pt/Al_2O_3	68	1.9	7	7[d]	133
Au/Al_2O_3	72	2.2	0	0[d]	154
SiO_2	94	---	---	0[c]	7
Cu/SiO_2	95	1.0	---	16[c]	22
Cu-Zn-Al	60	33	---	494[c]	178
Nano-Cu	8	100	0	---	---

[a] Determined by the amount of precursor used. Cu contents for the Cu−Zn−Al catalysts were obtained from vendor specification.
[a] Cu contents for Nano-Cu was obtained by phase composition analysis in XRD.
[c] Site density probed by N_2O chemisorption.
[d] Site density probed by CO chemisorption.

X-ray diffraction (XRD) patterns for the materials are shown in Figure 2.4. The absence of peaks for Cu and Pt in diffraction patterns for CeO_2- and Al_2O_3-supported Cu and Pt catalysts suggests that the metal domains were small and well dispersed. In contrast, small CuO peaks are

observed for the Cu/SiO_2 catalyst, indicating the formation of crystalline domains, albeit with dimensions that were too small to be quantified using XRD. In contrast, peaks for Au can clearly be observed in patterns for the Au/CeO_2 and Au/Al_2O_3 catalysts, with average crystallite sizes of 18 and 31 nm, respectively, based on line broadening analysis [33].

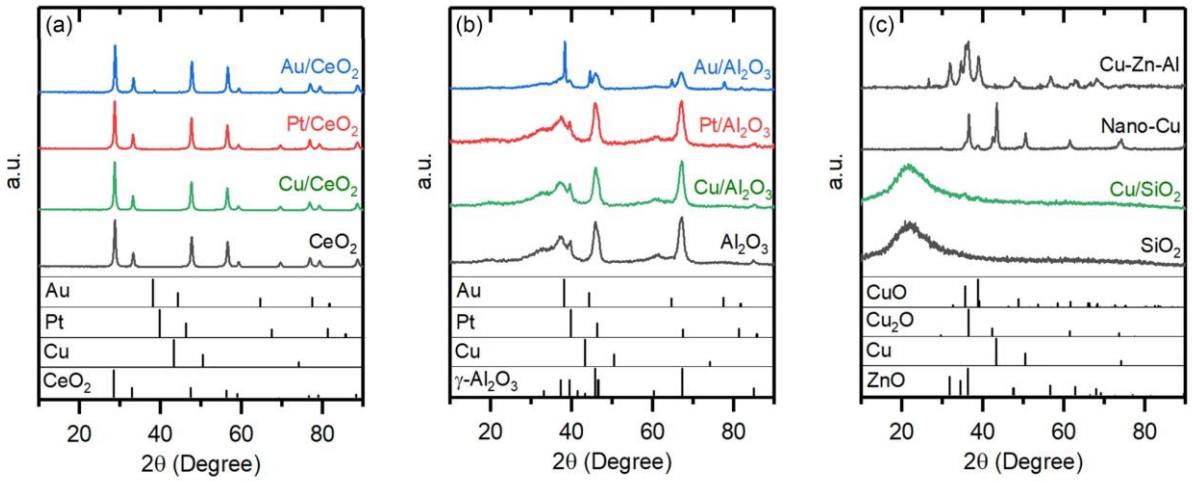

Figure 2.4 Diffraction patterns for (a) CeO_2-, (b) Al_2O_3-, and (c) SiO_2-supported Cu catalysts, Cu-Zn-Al, and Nano-Cu. Relevant standards were included: CuO (JCPDF 98-00-0429), Cu_2O (JCPDF 98-000-0186), Cu (JCPDF 00-004-0836), Pt (JCPDF 00-004-0802), Au (JCPDF 00-004-0787), ZnO (JCPDF 00-005-0664), CeO_2 (JCPDF 00-034-0394), and Al_2O_3 (JCPDF 00-047-1308). SiO_2 is amorphous.

The NH_3 temperature programmed desorption (TPD) spectra for the CeO_2-, Al_2O_3-, and SiO_2-supported metal catalysts are shown in Figure 2.5. Most of the NH_3 desorbed at 100-200 °C, which suggests that the majority of acid sites are weak acid sites [24]. The NH_3 uptake for each of the catalysts are listed in Table 2.1. The total amount of NH_3 taken up decreased in the following order: $M/Al_2O_3 > M/CeO_2 > M/SiO_2$. It is not unexpected that the Al_2O_3-supported catalysts had the highest acid site densities, given that Al_2O_3 is known for its surface acidity [24,34]. Overall, these uptakes and the desorption temperatures are similar with prior reports [24,28,35].

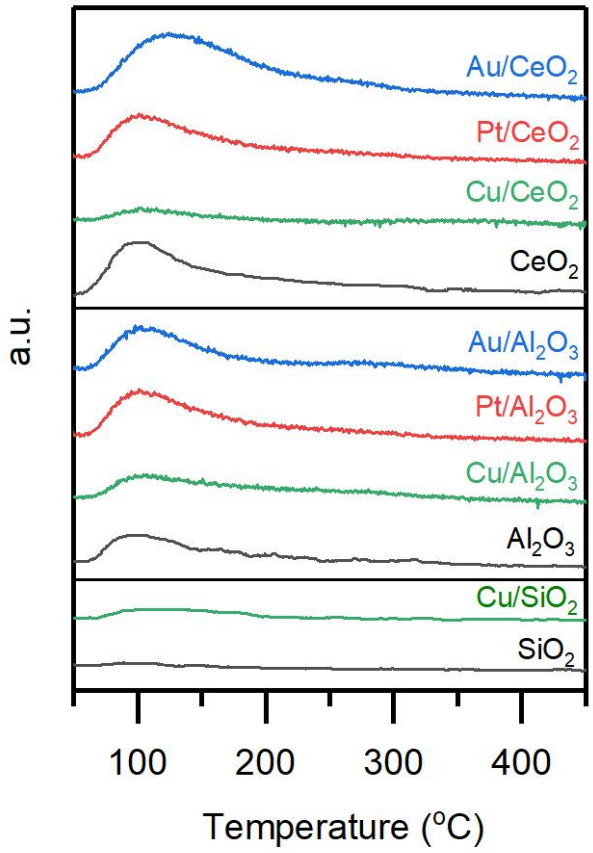

Figure 2.5 Surface area normalized NH_3 desorption spectra for metal oxide-supported catalysts and bare supports.

In N_2O chemisorption experiments, the results for the Cu/CeO_2 catalyst implied a N_2O:Cu surface site ratio greater than the theoretical maximum stoichiometry of 1:2. This resulted in a value over 100% when estimating the dispersion. This is likely a consequence of the oxygen from N_2O spilling over to vacancies on the CeO_2 support, as Cu can significantly enhance the reducibility of CeO_2 [7,36]. Thus, the results of N_2O chemisorption experiment cannot be accurately interpreted as the actual site density for the Cu/CeO_2 catalysts. Similar observations were reported by Sun et al. and Maciel et al. [37,38]. Because N_2O chemisorption was not suitable for determining the Cu surface site density for the Cu/CeO_2 catalyst and the Cu particles were x-ray amorphous, we estimated the turnover frequency (TOF) of Cu/CeO_2 assuming 100% Cu

dispersion. This will underestimate the TOF but provide a useful metric for comparison with the other Cu-based catalysts. The N_2O uptake based Cu dispersions for the Cu/Al_2O_3 and Cu/SiO_2 catalysts were typical of those reported in the literature, which are 40% and 10%, respectively [39].

2.3.2 Aldehyde Water Shift Activity

In this chapter, the performances of CeO_2-, Al_2O_3-, and SiO_2-supported metal catalysts were evaluated for the AWS reaction. In addition to acetic acid and H_2, the expected products for the AWS reaction, several other carbon-containing products were formed, which suggests that reactions other than AWS were facilitated by the catalysts studied here. These products and associated reactions will be discussed in the next section.

To clarify the source of H_2, several possible reactions that produce H_2 over supported Cu catalysts were evaluated. While it has been reported that H_2 could potentially form via ethanol dehydrogenation (Equation 2.1) under similar conditions to those used here [40,41], the product distribution was not observed to change with varying flow rate. This suggests that ethanol dehydrogenation is not a significant source of H_2. Additionally, neither CO nor CO_2 were observed in the product stream during the reaction, which implies steam reforming was also not a significant source of H_2. For Pt/CeO_2 and Pt/Al_2O_3 catalysts, CO and CH_4 were produced via acetaldehyde decarbonylation during deactivation (Equation 2.2) [42]. With the catalyst formulations, it would not be unexpected for some of the CO to be consumed in the WGS and produced H_2. However, the production of CO and CH_4 decayed to rates below the detection limit after deactivation. Based on these observations, the AWS reaction was concluded to be the primary source of H_2 production after the deactivation of catalysts, and the H_2 production rate was used as a direct measure of the

pseudo-steady AWS rate. In general, AWS rates determined from the H_2 production rates were consistent with the hydrocarbon production results.

$$CH_3CH_3OH \rightarrow CH_3CHO + H_2 \text{ (Equation 2.1)}$$

$$CH_3CHO \rightarrow CH_4 + CO \text{ (Equation 2.2)}$$

During all the reactions, aldehyde conversion was limited to 5% to maintain differential conditions and minimize the reverse reaction (see Appendix for the equilibrium calculation). The reaction conversion at 240 °C was inversely proportional to the flow rate, indicating that the rates were not limited by mass transport.

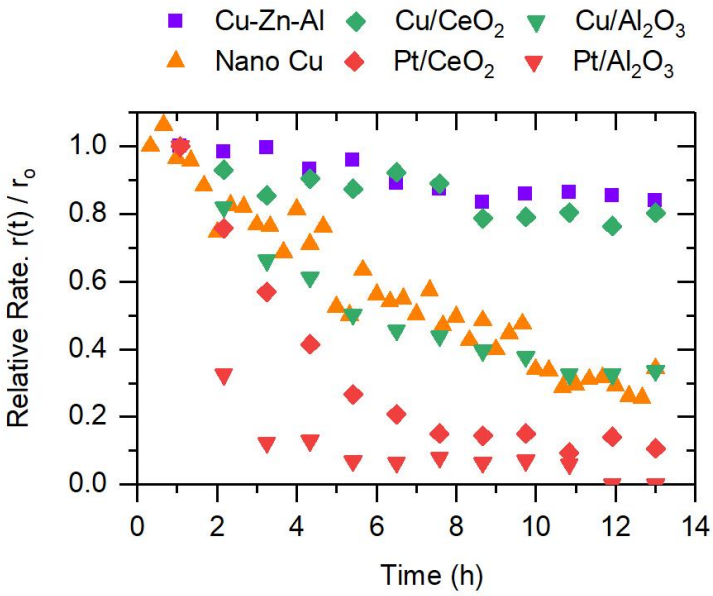

Figure 2.6 Normalized deactivation profiles for H_2 production (relative to initial rates) at 240 °C for the CeO_2-and Al_2O_3-supported Cu and Pt catalysts, Cu-Zn-Al, and Nano-Cu catalysts.

All catalysts deactivated during the first several hours on stream; representative plots are provided in Figure 2.6. At 240 °C, the H_2 production rates for all catalysts reached a pseudo-steady state after 8-10 hours on stream. While Cu/CeO_2 and Cu-Zn-Al deactivated by less than 40%, activities for the Cu/Al_2O_3 and Nano-Cu deactivated by ~70% during the first 10 hours on stream,

while Pt/CeO_2 and Pt/Al_2O_3 catalysts decreased by ~90%. The deactivation profiles were fit to model decay laws (see Table 2.2) to elucidate the mechanism. Results for the Cu-Zn-Al and Cu/CeO_2 were reasonably well fit by exponential and hyperbolic models, while data for the Nano-Cu catalyst was best fitted by the exponential model. The exponential decay model is typically associated with deactivation by surface poisoning whereas the hyperbolic decay model suggests sintering. Results for the Cu/Al_2O_3 catalyst were best fitted by the reciprocal power model which often indicates deactivation via site fouling or coking [43,44]. The basis for these differences is not currently known, and is the subject of future research.

Table 2.2 Results from nonlinear regression of H_2 production rates for Cu-Zn-Al, Nano-Cu, Cu/CeO_2, Pt/CeO_2, Cu/Al_2O_3, and Pt/Al_2O_3 empirical decay rate laws. a(t) is the ratio of the rate at time t to the initial rate (a=r(t)/ro), kd is the specific decay constant, and t is time on stream.

	Type	Linear	Exponential	Hyperbolic	Reciprocal Power
Catalysts	Differential form	$-da/dt = k_d a$	$-da/dt = k_d a$	$-da/dt = k_d a^2$	$-da/dt = k_d A_0^{1/5} a^m$
	Integral form	$a = 1 - k_d t$	$a = e^{-k_d t}$	$a = 1/(1 + k_d t)$	$a = A_0 t^{-k_d}$
Cu-Zn-Al	k_d (h^{-1})	0.0138	0.0153	0.0169	0.092
	A_o	---	---	---	1.043
	R_{adj2}	0.0824	**0.0839**	**0.847**	0.799
Nano-Cu	k_d (h^{-1})	0.063	0.095	0.137	0.310
	A_o	-	-	-	0.921
	R_{adj2}	0.917	**0.934**	0.882	0.757
Cu/CeO_2	k_d (h^{-1})	0.019	0.021	0.024	0.092
	A_o	-	-	-	1.007
	R_{adj2}	0.686	**0.709**	**0.7243**	0.704
Pt/CeO_2	k_d (h^{-1})	0.093	0.2271	0.418	0.570
	A_o	-	-	-	0.748
	R_{adj2}	0.584	**0.929**	0.834	0.810
Cu/Al_2O_3	k_d (h^{-1})	0.064	0.105	0.160	0.453
	A_o	-	-	-	1.086
	R_{adj2}	0.765	0.941	0.933	**0.974**
Pt/Al_2O_3	k_d (h^{-1})	0.103	0.401	0.823	1.592
	A_o	-	-	-	1.131
	R_{adj2}	-0.34	0.801	0.640	**0.990**

Pseudo-steady state areal rates for the supported Cu catalysts were significantly higher than those for the supports, demonstrating the importance of Cu (see Table 2.3).

Overall, both the admetal and support appeared to have a significant impact on the AWS reaction rate. In contrast to the inactivity of bare Al_2O_3 and SiO_2 supports, CeO_2 was observed to

have a low AWS activity (1.3 nmol/m^2·s), which is not surprising considering previous evidence of AWS catalysis with CeO_2 reported by Orozco et al. [1,30]. After metal deposition on CeO_2, the admetal changed the catalysts reactivity drastically. The stable rate of the Cu/CeO_2 catalyst was 13.6 nmol/m^2·s, which is 4 times higher than those for CeO_2-supported Pt and Au catalysts, and an order of magnitude higher than the rate of bare CeO_2.

In comparison to the M/CeO_2 catalysts, M/Al_2O_3 catalysts were relatively inactive. This is likely due to the difference in support reducibility; recall that Al_2O_3 is irreducible. For M/Al_2O_3 catalysts, only Cu/Al_2O_3 was observed to produce small amounts of H_2 after deactivation, with a rate 0.5 nmol/m^2·s of H_2 after the catalyst stabilized. The bare Al_2O_3 is inactive for AWS. While the promotion effect was less obvious with the Al_2O_3-supported metal catalysts, the reactivity trends of the supported admetals themselves were similar to CeO_2-based catalysts.

The effect of the support on reactivity was further investigated by comparing the AWS activity of Nano-Cu, Cu-Zn-Al, and Cu/SiO_2 with the previously discussed Cu/CeO_2 and Cu/Al_2O_3. Taking the Cu content and site density into consideration, the Cu site density-normalized rates (mol H_2/s/mol_{Cu}) were found to be a strong function of the support type and decreased in the following order: Cu/CeO_2 > Cu-Zn-Al > Nano-Cu ~ Cu/Al_2O_3. As stated earlier, we assumed 100% dispersion for Cu on CeO_2. Consequently, the Cu site density-normalized rate for Cu/CeO_2 catalyst in Table 2 can be considered as a lower limit for its activity. The activation energies were similar for all of the catalysts (see Table 2.3 and Figure 2.7).

Table 2.3 The AWS rates and Cu site-normalized rates at 240 ˚C, and the associated activation energies.

Catalysts	H_2 Production Rate (nmol/s/m^2)	AWS Rate (mol H_2/s/mol_{Cu} x 10^3)	Activation Energy (kcal/mol)
CeO_2	1.3	---	---
Cu/CeO_2	13.6	8.8[a]	19
Pt/CeO_2	3.3	---	19
Au/CeO_2	2.1	---	18
Cu/Al_2O_3	0.5	0.8[b]	23
Cu/SiO_2	<0.1[d]	<0.6[b]	---
Cu-Zn-Al	27.8	3.4[b]	22
Nano-Cu	13.8	0.8[c]	---

[a] Assumed 100% dispersion for Cu on CeO_2.
[b] Cu site density was determined by N_2O chemisorption.
[c] Calculated based on the surface area, assuming 10^{19} Cu sites/m^2.
[d] Calculated based on the detection limitation of the GC-TCD.

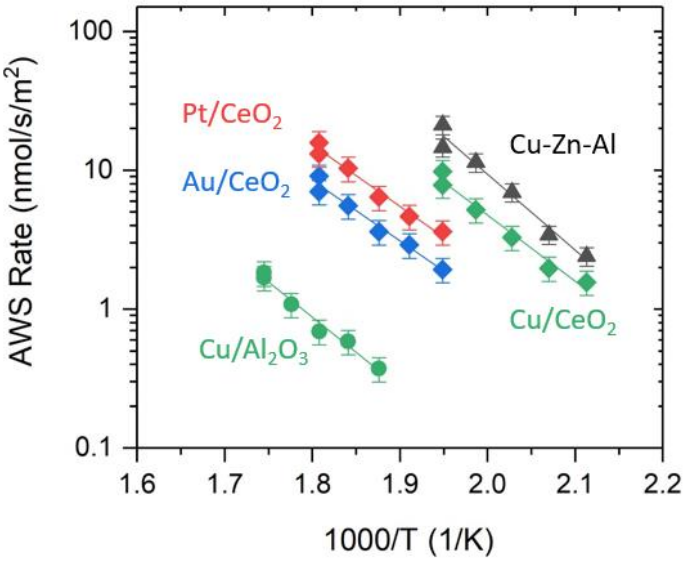

Figure 2.7 Arrhenius plots of the H_2 production rate rates for CeO_2- and Al_2O_3-supported metal catalysts.

2.3.3 Selectivity

In addition to acetic acid and H_2, crotonaldehyde production was observed for all the catalysts; ethanol was also produced in the case of Cu/CeO_2, Cu-Zn-Al and Nano-Cu catalysts.

CO, CH_4, and small amounts of paraldehyde and acetone were produced for some of the catalysts. Selectivity to the carbon-containing products are shown in Figure 2.8.

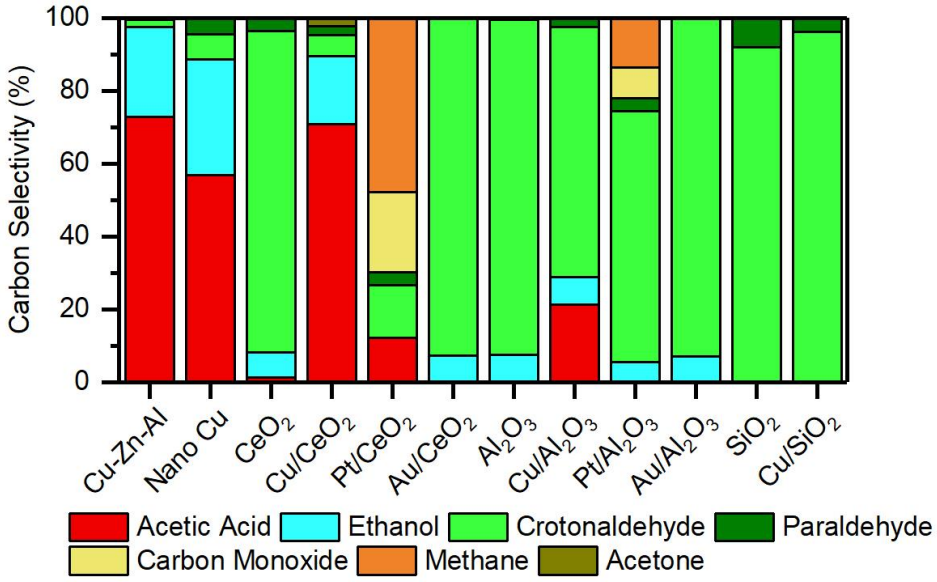

Figure 2.8 Carbon selectivities for the catalysts. The selectivities are defined as the moles of acetaldehyde reacted to form a specific product divided by the total amount of acetaldehyde converted.

The AWS active catalysts, primarily the Cu-based catalysts, were the most selective for acetic acid. Notably, Cu/CeO_2, Cu-Zn-Al, and Nano-Cu catalysts yielded high selectivity to acid, which were proximal to those reported for the homogeneous catalysts [45,46]. In addition to acid, the Nano-Cu also favored ethanol formation with a selectivity of approximately 35%. To determine the source of the ethanol formed, a control experiment was conduct in which only H_2 and acetaldehyde were fed to the Cu/CeO_2 catalyst. Under these conditions, very little ethanol was detected and there was no evidence of H_2 consumption. This result suggests that acetaldehyde hydrogenation was not the major source of ethanol produced. Instead, it is believed that the ethanol was produced via the Cannizzaro reaction (Equation 2.3) [46,47]. The crotonaldehyde is likely a product of aldol condensation (Equation 2.4). Paraldehyde was a minor product for some catalysts, which may have been formed via acetaldehyde trimerization (Equation 2.5) [48]**.** CO and CH_4

were only produced on Pt-based catalysts and likely were products of acetaldehyde decarbonylation [42].

$$2CH_3CHO + H_2O \rightarrow CH_3CH_2OH + CH_3COOH \text{ (Equation 2.3)}$$

$$2CH_3CHO \rightarrow CH_3CHCHCHO + H_2O \text{ (Equation 2.4)}$$

$$3\ CH_3CHO \rightarrow (CH_3CHO)_3 \text{ (Equation 2.5)}$$

The CeO_2, Al_2O_3, and Au/Al_2O_3 catalysts produced small amounts of ethanol but no acetic acid. This may because (1) the amounts of acid produced were close to/below the detection limit of the GC-FID, or (2) the small amount of ethanol was produced via acetaldehyde hydrogenation [25,49], or a combination of both. The Cannizzaro (ethanol production) and aldol condensation (crotonaldehyde production) reaction rates at 240 °C are compared in Table 2.4. Overall, the rates for the M/CeO_2, and M/Al_2O_3 catalysts were generally higher than those for their supports. As aldol condensations can be acid catalyzed [50], the rates were normalized by the NH_3 uptakes to allow comparisons of the intrinsic activities. The TOF is approximately 0.91±0.23 1/s. Due to the strong interaction between Pt and acetaldehyde, Pt-based catalysts behaved differently and their aldol condensation TOFs were not included.

Table 2.4 Average ethanol and crotonaldehyde production rates and turnover frequencies for metal oxide-supported catalysts and bare supports at 240 °C over 14 hrs on stream.

Catalysts	Acetic Acid Production Rate ($nmol/s/m^2$)	Ethanol Production Rate ($nmol/s/m^2$)	Crotonaldehyde Production Rate ($nmol/s/m^2$)	Aldol Condensation Turnover Frequencies ($1/s \times 10^3$)[b]
CeO_2	0.02	0.12	0.76	0.78
Cu/CeO_2	9.62	2.54	0.38	0.80
Pt/CeO_2	0.89	0	0.53	---
Au/CeO_2	0	0.63	4.03	1.50
Al_2O_3	0	0.13	0.80	0.95
Cu/Al_2O_3	0.63	0.23	1.01	0.89
Pt/Al_2O_3	0	0.15	0.92	---
Au/Al_2O_3	0	0.27	1.80	0.85
Cu/SiO_2	0	---	0.16	0.67
Cu-Zn-Al	48.02	16.4	0.64	0.22[c]
Nano-Cu	23.28	13.1	1.42	---

2.4 Discussion

In this chapter, we designed a series of metal oxide supported metal catalysts for the AWS reaction, including CeO_2- and Al_2O_3-supported Cu, Pt, and Au catalysts; surface and physical properties, as well as reactivities of catalysts, were also evaluated.

Among the three surface metals (Pt, Cu, and Au) discussed in this chapter, the supported Cu catalysts stood out and outperformed the supported Pt and Au catalysts after reaching the pseudo-steady state. The stable rate of the Cu/CeO_2 catalyst was 13.6 $nmol/m^2 \cdot s$, which is 4 times higher than those for CeO_2-supported Pt and Au catalysts and an order of magnitude higher than the rate of bare CeO_2. The activity enhancement of Cu on CeO_2 highlighted the importance of the presence of admetal and the metal selection. The observed difference in reactivity may be attributed to the differences in admetal-aldehyde interaction [51]. For Pt/CeO_2 catalyst, aldehyde

decomposition was catalyzed instead of AWS reaction, likely due to the strong interactions between acetaldehyde and Pt [42]. The strong bonding could also be the principal cause for deactivation of the Pt/CeO_2 and Pt/Al_2O_3 catalysts. For the Au/CeO_2 catalyst, the aldehyde-admetal interaction may not be strong enough to facilitate reaction turnover. The relatively large particle size of Au (average crystallite sizes of 18 nm for Au/CeO_2 and 31 nm for Au/Al_2O_3, determined via XRD) may also explain the lower activity; for reactions including CO oxidation and the WGS reaction, Au particles larger than a few nanometers were reported to be inactive [52,53].

In addition to differences related to admetal selection, the support also showed a significant impact on AWS reactivity. Compared with CeO_2-supported metal catalysts, the Al_2O_3-supported metal catalysts were relatively inactive; the rate of Cu/CeO_2 observed was 27-fold of that for the Cu/Al_2O_3. This is likely due to the difference in support reducibility; recall that Al_2O_3 is irreducible. With the observation, the support clearly played a key role in catalyzing the reaction. For Al_2O_3-supported metal catalysts, only Cu/Al_2O_3 was observed to produce small amounts of H_2 after deactivation, with a rate 0.5 $nmol/m^2 \cdot s$ of H_2 at pseudo-steady state. The bare Al_2O_3 is inactive for AWS. While the promotion effect was less obvious with the Al_2O_3-supported metal catalysts, the reactivity trends of the supported admetals themselves were similar to CeO_2-based catalysts. The activation energies were similar for each support group, which suggested that the rate-limiting step occurred on the supports. Given that the activation energies for the AWS were similar to those reported for WGS (e.g. 19 and 17 kCal/mol for Pt/CeO_2 and Cu-Zn-Al catalysts, respectively [6,54]), it is possible that water dissociation was the rate limiting step, which parallels many reports for WGS over metal oxide supported metal catalysts [4,55,56].

The effect of the support on reactivity was further investigated by comparing the reactivity of Nano-Cu, Cu-Zn-Al, and Cu/SiO_2 with the previously discussed Cu/CeO_2 and Cu/Al_2O_3. Taking the Cu content and site density into consideration, the Cu site density-normalized rates (mol H_2/s/mol_{Cu}) were found to be strong functions of the support type, and decreased in the following order: Cu/CeO_2 > Cu-Zn-Al > Nano-Cu ~ Cu/Al_2O_3. The Cu site-normalized rate of Cu/CeO_2 catalyst ($8.8 \cdot 10^{-3}$ mol H_2/s/mol_{Cu}) was approximately an order of magnitude higher than those for the Cu/Al_2O_3 and bulk Cu catalysts ($0.8 \cdot 10^{-3}$ mol H_2/s/mol_{Cu}). These results agree with our previous observation that the presence of CeO_2 makes a significant contribution beyond Cu dispersion, likely a consequence of its reducibility and the mobility of oxygen on the surface of CeO_2. The promotion effect of Cu may also be attributed to the enhancement of catalyst reducibility, as the addition of Cu to CeO_2 can stabilize and significantly increase the oxygen vacancies within CeO_2 [7,36], which was observed in our N_2O chemisorption experiments. In contrast, Al_2O_3 and SiO_2 are irreducible under the reaction conditions and it is not surprising that they are inactive for the AWS reaction. Note that the Cu site-normalized rates for Cu/Al_2O_3 and bulk Nano-Cu catalysts were similar; the deactivation behaviors were also nearly identical. These results suggest that the modest activity of the Cu/Al_2O_3 catalyst is likely due to solely to the Cu admetal. Given that ZnO is considered less reducible than CeO_2 [4], it is not unexpected that the TOF for the Cu-Zn-Al was intermediate those for Cu/CeO_2, Cu/Al_2O_3, and bulk Cu catalysts. While Cu/SiO_2 was expected to show activity similar to Cu/Al_2O_3 and bulk Cu, the low dispersion of Cu on SiO_2 resulted in a substantially slower H_2 production rate below the detection limit of our GC, making an accurate rate quantification inaccessible.

Aside from Cu, the addition of Pt and Au on CeO_2 have also been reported to enhance the reducibility of support and enhance the WGS activity of catalysts [4,5,17]. However, the trends

observed for the AWS reaction were different from the trends previously reported for the WGS reaction, along with the production of CH_4 and CO for Pt-based catalysts. As discussed earlier, this may be due to different interactions between the reactant and surface metal, a more complex reactant structure, as well as the relatively large Au particle size.

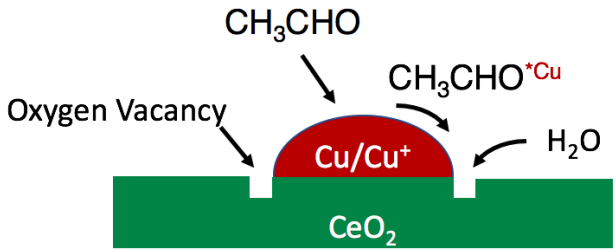

Figure 2.9 Schematic representation of the proposed AWS reaction mechanism on Cu/CeO_2.

The results described thus far are consistent with a bifunctional mechanism for AWS over the Cu/CeO_2 catalyst, with sites on CeO_2 responsible for H_2O dissociation and sites on or at the interface of the Cu domains for aldehyde oxidation, with oxygen directly or indirectly (via, for example, a Mars-Van Krevelen-type mechanism) sourced from H_2O (see Figure 2.9 and Equation 2.6 to Equation 2.10). Intimacy between these two distinct catalytic sites would facilitate high AWS rates. A similar type of mechanism could explain results for the Cu-Zn-Al with ZnO responsible for H_2O dissociation and Cu for acetaldehyde oxidation.

$$H_2O + 2*^S \rightarrow H*^S + OH*^S \text{ (Equation 2.6)}$$

$$CH_3CHO + *^M \rightarrow CH_3CHO*^M \text{ (Equation 2.7)}$$

$$CH_3CHO*^M + HO*^S \rightarrow CH_3COOH*^M + H*^S \text{ (Equation 2.8)}$$

$$CH_3COOH*^M \rightarrow CH_3COOH + *^M \text{ (Equation 2.9)}$$

$$2H*^S \rightarrow H_2 + 2*^S \text{ (Equation 2.10)}$$

In comparing results for our supported Cu catalysts with those reported for homogeneous catalysts, the heterogeneous catalysts appeared to be less active and, in some cases, less selective

for the AWS reaction. Brewster reported results that are consistent with an AWS TOF of $3.6 \cdot 10^{-3}$ 1/s for a $[(p\text{-cymene})RuCl_2]_2$ catalyst at 105 °C [45]. Extrapolating rates using the measured activation energies, the TOF for the Cu/CeO_2 catalyst would be two orders of magnitude lower, or $1.1 \cdot 10^{-5}$ 1/s at 105 °C, assuming atomic dispersion of the Cu. The assumption of 100% dispersion overestimates the density of active sites, but we do not believe that the dispersion is two orders of magnitude lower (i.e. 1%). While the Cu/CeO_2 catalyst appears to be less active than the homogeneous catalysts, it appears to be more active than other heterogeneous catalysts that have been described in the literature. Xiang et al. did not report AWS rates directly, but the results indicate an AWS rate of 0.55 $\mu mol/g_{Cu}/s$ at 350 °C [2]. Extrapolating data for our Cu/CeO_2 catalyst to 350 °C yields a rate of 3,596.2 $\mu mol/g_{Cu}/s$. Dispersions for these materials are dissimilar, although it is unlikely they differ by four orders of magnitude. Similarly, it is unlikely that differences in the reaction conditions can reconcile the significantly different rates.

In addition to the AWS reaction, the materials catalyzed the Cannizzaro and aldol condensation reactions. Given the high Cannizzaro reaction rates for the bulk Cu catalyst and the low rates observed for the bare metal oxide supports, ethanol production over the metal oxide-supported Cu catalysts appears to have been a consequence primarily of the Cu admetal. As metallic Cu is capable of activating water [55], it is not surprising that Cu was observed to catalyze the Cannizzaro reaction. In addition, the aldol condensation rates for most of the catalysts correlated with the weak acid site densities (see Table 2.4). These results are consistent with reports in the literature that aldol condensation can be acid-catalyzed [50,57,58]. Dumitriu et al. proposed that the acetaldehyde adsorbed in the η^1 form and reacts with the enol form of acetaldehyde to form an aldol on MFI zeolites. This aldol then converts to crotonaldehyde via dehydration [50]. Interestingly, the addition of Au to CeO_2 and Al_2O_3 resulted in higher surface

acidities and aldol condensation rates comparing to the bare metal oxide support. Abad et al. reported that interactions between Au and CeO_2 resulted in the formation of Ce^{3+} and positively charged Au particles [59], which could create additional Lewis acid sites for aldol condensation. More detailed characterizations are subject to future research. While an acid-base pairs mechanism was also reported for the condensation reaction [57], the investigation of acid-base coupling is not the aim of this research. Mechanisms for the Cannizzaro and aldol condensation reactions will be investigated and described in a future paper.

2.5 Conclusion

The results presented in this chapter explore the use of CeO_2- and Al_2O_3-supported Cu, Pt, and Au catalysts for the AWS reaction and demonstrate that the selection of both the admetal and support have a strong impact on reactivity. Based on our findings, supported Cu catalysts had higher AWS activity than supported Pt and Au catalysts, with Pt-based catalysts more preferentially decomposing acetaldehyde and Au-based catalysts being relatively inactive for AWS. The combination of Cu and a reducible oxide (i.e. CeO_2 or ZnO) yielded materials with high AWS activities, stabilities, and selectivities. We proposed that the reducible oxide catalyzed H_2O dissociation, while the Cu domains catalyzed aldehyde oxidation using oxygen from H_2O. The materials also catalyzed other reactions producing crotonaldehyde, ethanol and very small amounts of paraldehyde. The aldol condensation (crotonaldehyde formation) rates correlated with the acid site densities, and the Cannizzaro reaction (ethanol formation) appeared to be catalyzed by the surface Cu. Future work for the oxide-based materials could focus on characterizing the support reducibility and adsorption energy of aldehyde on the admetals, in addition to the investigation of complete mechanisms for the reactions.

2.6 Reference

[1] L. M. Orozco, M. Renz, A. Corma, Green Chem. 19 (2017) 1555–1569.
[2] N. Xiang, P. Xu, N. Ran, T. Ye, RSC Adv. 7 (2017) 38586–38593.
[3] Q. Fu, A. Weber, M. Flytzani-Stephanopoulos, Catal. Lett. 77 (2001) 87–95.
[4] J. A. Rodriguez, P. Liu, J. Hrbek, J. Evans, M. Pérez, Angew. Chem. 119 (2007) 1351–1354.
[5] A. Bruix, J. A. Rodriguez, P. J. Ramírez, S. D. Senanayake, J. Evans, J. B. Park, D. Stacchiola, P. Liu, J. Hrbek, F. Illas, J. Am. Chem. Soc. 134 (2012) 8968–74.
[6] N. M. Schweitzer, J. A. Schaidle, O. K. Ezekoye, X. Pan, S. Linic, L. T. Thompson, J. Am. Chem. Soc. 133 (2011) 2378–2381.
[7] X. Wang, J. A. Rodriguez, J. C. Hanson, D. Gamarra, A. Martinez-Arias, M. Fernandez-Garcia, J. Phys. Chem. B 110 (2006) 428–434.
[8] J. A. Rodriguez, P. Liu, X. Wang, W. Wen, J. Hanson, J. Hrbek, M. Pérez, J. Evans, Catal. Today 143 (2009) 45–50.
[9] K. G. Azzam, I. V. Babich, K. Seshan, L. Lefferts, J. Catal. 251 (2007) 153–162.
[10] M. Cargnello, V. V. T. Doan-nguyen, T.R. Gordon, R.E. Diaz, E.A. Stach, R.J. Gorte, P. Fornasiero, C.B. Murray, Science 341 (2013) 771–774.
[11] J. A. Rodriguez, D. C. Grinter, Z. Liu, R. M. Palomino, S. D. Senanayake, Chem. Soc. Rev. 46 (2017) 1824–1841.
[12] Z.J. Zhao, Z. Li, Y. Cui, H. Zhu, W.F. Schneider, W.N. Delgass, F. Ribeiro, J. Greeley, J. Catal. 345 (2017) 157–169.
[13] M. Kotobuki, R. Leppelt, D.A. Hansgen, D. Widmann, R.J. Behm, J. Catal. 264 (2009) 67–76.
[14] S. J. Tauster, S. C. Fung, R. T. K. Baker, J. A. Horsley, Science 211 (1981) 1121–1125.
[15] A. Kubacka, M. Fernández-García, A. Martínez-Arias, Appl. Catal., A. 518 (2016) 2–17.
[16] C. T. Campbell, Nat. Chem. 4 (2012) 597–598.
[17] C. H. Kim, L. T. Thompson, J. Catal. 244 (2006) 248–250.
[18] Y. Li, Q. Fu, M. Flytzani-Stephanopoulos, Appl. Catal., B. 27 (2000) 179–191.
[19] Y. Men, H. Gnaser, R. Zapf, V. Hessel, C. Ziegler, G. Kolb, Appl. Catal., A. 277 (2004) 83–90.
[20] S. T. Yong, C. W. Ooi, S. P. Chai, X. S. Wu, Int. J. Hydrogen Energy 8 (2013) 9541–9552.
[21] M. Bowker, R. J. Madix, Appl. Surf. Sci. 8 (1981) 299–317.
[22] S. E. Davis, B. N. Zope, R. J. Davis, Green Chem. 14 (2012) 143–147.
[23] J. L. Rodriguez, E. Pastor, X H. Xia, T. Iwasita, Langmuir 16 (2000) 5479–5486.
[24] P. Berteau, B. Delmon, Catal. Today 5 (1989) 121–137.
[25] J. Raskó, J. Kiss, Appl. Catal., A. 287 (2005) 252–260.
[26] P. Li, K. A. Perreau, E. Covington, C. H. Song, G. R. Carmichael, V. H. Grassian, Geophys. Res. 106 (2001) 5517–5529.
[27] Y. Chen, S. Choi, L. T. Thompson, ACS Catal. 5 (2015) 1717–1725.
[28] S. K. Bej, C. A. Bennett, L. T. Thompson, Appl. Catal. A 250 (2003) 197–208.
[29] C. Ratnasamy, J. P. Wagner, Catal. Rev. 51 (2009) 325–440.
[30] L. M. Orozco, M. Renz, A. Corma, ChemSusChem. 9 (2016) 2430–2442.
[31] K. D. Sabnis, Y. Cui, M. C. Akatay, M. Shekhar, W. S. Lee, J. T. Miller, W. N. Delgass, F. H. Ribeiro, J. Catal. 331 (2015) 162–171.
[32] Y. Chen, S. Choi, L. T. Thompson, J. Catal. 343 (2016) 147–156.
[33] A. Monshi, M.R. Foroughi, M.R. Monshi, 2012 (2012) 154–160.

[34] H. Pines, W. O. Haag, J. Am. Chem. Soc. 82 (1960) 2471–2483.
[35] J. Y. Miao, L. F. Yang, J. X. Cai, Surf. Interface Anal. 28 (1999) 123–125.
[36] L. P. Matte, A. S. Kilian, L. Luza, M. C. M. Alves, J. Morais, D. L. Baptista, J. Dupont, F. Bernardi, J. Phys. Chem. C 119 (2015) 26459–26470.
[37] J. Sun, L. Zhang, C. Ge, C. Tang, L. Dong, Chin. J. Catal. 35 (2014) 1347–1358.
[38] C. G. Maciel, M. N. Belgacem, J. M. Assaf, Catal. Lett. 141 (2011) 316–321.
[39] A. Dandekar, M.A. Vannice, J. Catal. 178 (1998) 621–639.
[40] K. Weissermel, A. Hans-Jürgen, Industrial Organic Chemistry, WILEY-VCH Verlag GrnbH & Co. KGaA, Weinheim, 2003
[41] M. E. Sad, M. Neurock, E. Iglesia, J. Am. Chem. Soc. 133 (2011) 20384–20398.
[42] H. Zhao, J. Kim, B. E. Koel, Surf. Sci. 538 (2003) 147–159.
[43] H.S. Fogler, Elements of Chemical Reaction Engineering, forth ed., Pearson Education, Inc. Upper Saddle River, New Jersey, 2006
[44] J. A. Schaidle, A. C. Lausche, L. T. Thompson, J. Catal. 272 (2010) 235–245.
[45] T. P. Brewster, J. M. Goldberg, J. C. Tran, D. M. Heinekey, K. I. Goldberg, ACS Catal. 6 (2016) 6302–6305.
[46] T. P. Brewster, W. C. Ou, J. C. Tran, K. I. Goldberg, S. K. Hanson, T. R. Cundari, D. M. Heinekey, ACS Catal. 4 (2014) 3034–3038.
[47] M. Watanabe, M. Osada, H. Inomata, K. Arai, A. Kruse, Appl. Catal., A. 245 (2003) 333–341.
[48] M. Eckert, G. Fleischmann, R. Jira, B.H. M., K. Golka, Aldehydes, in: Ullmann's Encyclopedia of Industrial Chemistry, Wiley-VCH, Weinheim, 2012, pp. 191-205
[49] H. Idriss, C. Diagne, J.P. Hindermann, A. Kiennemann, M.A. Barteau, J. Catal. 155 (1995) 219–237.
[50] E. Dumitriu, V. Hulea, I. Fechete, A. Auroux, J.-F. Lacaze, C. Guimon, Microporous Mesoporous Mater. 43 (2001) 341–359.
[51] B. Hammer, J. K. Norskov, Nature 376 (1995) 238–240
[52] M. Haruta, Chem. Rec. 3 (2003) 75–87.
[53] T. Tabakova, F. Boccuzzi, M. Manzoli, J.W. Sobczak, V. Idakiev, D. Andreeva Appl. Catal., B 49 (2004) 73–81.
[54] J. Patt, D.J. Moon, C. Phillips, L. Thompson, Catal. Lett. 65 (2000) 193–195.
[55] A. A. Gokhale, J. a. Dumesic, M. Mavrikakis, J. Am. Chem. Soc. 130 (2008) 1402–1414.
[56] P. Liu, J. A. Rodriguez, J. Chem. Phys. 126 (2007) 164705.
[57] M. J. Climent, A. Corma, V. Fornés, R. Guil-Lopez, S. Iborra, Adv. Synth. Catal. 344 (2002) 1090–1096.
[58] M. I. Zaki, M. A. Hasan, L. Pasupulety, Langmuir 17 (2001) 768–774.
[59] A. Abad, A. Corma, Angew. Chem. Int. Ed. 44, (2005) 4066–4069.

Chapter 3

AWS with Mo_2C Supported Metal Catalysts

3.1 Introduction

In chapter 2, we investigated the used of metal oxide supported Cu, Pt, and Au catalysts for the AWS reaction. We reported that both supports and surface admetals have significant impacts on the reactivity of the material. To summarize, the highest AWS activity was found in catalysts that integrated the surface Cu site with reducible supports, namely Cu/CeO_2 and Cu-Zn-Al. In contrast, Al_2O_3-based catalysts were inactive. Pt and Au admetals were also not as effective for the AWS reaction. The results observed for the active catalysts were consistent with the bifunctional mechanism, in which the most active AWS catalysts possess distinct sites for water dissociation and for aldehyde oxidation. Building upon the concept of bifunctional mechanism, we further explore the use of Mo_2C as the catalyst support for the AWS reaction in this chapter. As Mo_2C was reported to have sites for water dissociation and aldehyde adsorption, we expected the material could be highly active for the AWS reaction, even without the assistance of surface admetals.

In past decades, Mo_2C supported metal catalysts have been shown to be promising catalysts for numerous reactions, in particular for reactions that use water as an oxidant (e.g. water gas shift WGS and steam reforming of alcohol [1–4]). These catalysts are highly active and outperform conventional metal oxide supported metal catalysts. The superior catalytic performances of Mo_2C supported metal catalyst for water gas shift (WGS) were attribute to two aspects. First, Mo_2C is able to catalyze water dissociation effectively [5,6], which provides the oxygen required for

oxidation. This water dissociation step was reported to be the rate-limiting step for conventional metal oxide catalysts [7,8]. Secondly, the surface metals provide additional sites for oxidation. For WGS, the high activity of Pt/Mo_2C was attribute to the interaction between sites on Pt admetal and Mo_2C support, where the Mo_2C domain dissociates water and the Pt domain assists CO adsorption [1,9]. A similar conclusion was drawn for Mo_2C supported Au, Cu, Pd, and Ni catalysts [2]. Aside from WGS, a similar mechanism was also reported for the steam reforming of methanol and ethanol on Mo_2C supported Cu and Au catalysts, in which the Mo_2C support is responsible for water dissociation and the surface metals provide sites for hydrocarbon adsorption [3,10,11].

As H_2O is used as an oxidant in both AWS and WGS, the two reactions could have parallel mechanisms. Utilizing previous knowledge from the WGS reaction and steam reforming, an analogous conceptual framework for catalyst design could then be developed. As known from the WGS studies, the Mo_2C possess sites for water dissociation; P. Liu and J. Rodriguez reported that H_2O is most likely to be activated and dissociated on the C sites [5]. In addition to water dissociation, Siaj et al. reported that aldehyde could adsorb via the O lone pair on the Mo site [12]. Developing on these reports, we can implement the idea of the bifunctional mechanism and expect Mo_2C-based catalysts to be effective for catalyzing AWS. In this chapter, we selected Cu, Pt, and Au as admetals. These metals enhanced the AWS activity of reducible oxide catalysts as discussed in Chapter 2, and were also reported to be effective for promoting the WGS and steam reforming activities of Mo_2C. Thus, with the deposition of Cu, Pt, and Au on Mo_2C, we expected the activities for the AWS reaction could be further enhanced.

In addition to investigating activity for AWS, we also attempted to study the surface characteristics driving the selectivity. As discussed in Chapter 2, the major side reactions determined, aldol condensation and Cannizzaro reaction, require two acetaldehyde molecules to

react, and the adsorption of aldehyde was speculated to take place on acid sites. Thus, we speculated that suppressing the surface acid site densities could suppress the side reactions and improve the selectivity. To investigate whether the surface acidity has effect on the selectivity, an alkali metal, K, that decreased surface acidity of Mo_2C/HY zeolite-based materials [13], was deposited on Mo_2C and the performance of the catalyst was evaluated.

3.2 Experimental Methods

3.2.1 Catalyst Synthesis

The high surface area molybdenum carbide catalysts discussed in this chapter were prepared via a temperature programmed reaction method as previously described [1,14,15]. The ammonium paramolybdate (AM) precursor powder, $(NH_4)_6Mo_7O_{24}$•4 (H_2O), 81-83% as MoO_3, Alfa Aesar), was sieved to retain particles with the sizes range between 125 and 250 μm. For each synthesis, ~1.3g of sieved AM were loaded into a quartz flow-through reactor, supporting on a quartz wool bed plugged in the reactor. The precursor was first treated with pre-purified H_2 (400 mL/min, Cryogenic Gases) at 350 °C for 12 hours (ramp rate 4.64 °C/min) to reduce the materials. After the reduction, the reaction gas was then switched from H_2 to a mixture of 15% CH_4 in H_2 (400 mL/min, Cryogenic Gases) to carburize the reduced materials into carbide. At this point, the material was heated to 590 °C at 2.67 °C /min and held at 590 °C for 2 hours. Once the carburization step was completed, the reactor was taken out from the furnace and quenched to room temperature (< 30 °C). The resulting synthesized material composed of a face-center-cubic α -MoC_{1-x} and an orthorhombic β-Mo_2C, and is referred as the "native" material. The Mo:C stoichiometry for both α -MoC_{1-x} and β-Mo_2C are close to 2:1 so we will refer to this material as Mo_2C [16]. Given the pyrophoric nature of Mo_2C, the catalysts was passivated in a mixture of 1% O_2/He (20 mL/min, Cryogenic Gases) for ~7 hours at room temperature to form a thin protective

oxidation layer that prevents bulk oxidation when exposed to air [14]. After passivation, the material was referred to as "passivated" Mo_2C.

For Mo_2C supported metal catalysts ([Metal]/Mo_2C), the metal was deposited onto native Mo_2C via the method of wet impregnation as previously reported [14]. Copper(II) nitrate hydrate ($Cu(NO_3)_2 \cdot 3H_2O$, Sigma-Aldrich), chloroplatinic acid hexahydrate ($H_2PtCl_6 \cdot 6H_2O$, Sigma-Aldrich), and gold(III) chloride trihydrate ($HAuCl_4 \cdot 3H_2O$, Sigma-Aldrich) were used as precursors for Cu, Pt, and Au deposition, respectively. The amount of metal precursor used was calculated based on the target nominal surface coverage.

Proper amount of metal precursor was measured and dissolved in 70 ml of deaerated water, which was continuously sparged with N_2. The native carbide was then transferred from the reactor to the as-prepared solution, under 15% CH_4/H_2 atmosphere. The native carbide was soaked in the precursor solution for 20 hours to ensure a completion of metal deposition onto the Mo_2C surface. After the deposition was completed, the slurry was transferred to a quartz reactor with pre-loaded quartz wool, and dried in H_2 (400 mL/min, Cryogenic Gases) at room temperature for 3 hours. The material was then heated to 110 °C (ramp rate 1.89 °C/min) for 2 hours, followed by a reduction at 450 °C for 4 hours (ramp rate 5.67 °C /min) to produce dispersed metal domains and remove the counterion. After reduction, the material was quenched and passivated as previously described. In this dissertation, the catalyst with x monolayer (ML) nominal surface coverage (based on 10^{19} site/m^2) of [Metal] was referred as "x ML [Metal]/Mo_2C".

In this chapter, the synthesis of Cu/K/Mo_2C was also attempted. The K was first deposited via incipient wetness impregnation (nominal loading 0.5 ML) on to the native carbide in an inert, water-tolerant glovebox. Proper amount of potassium carbonate (K_2CO_3, Sigma-Aldrich) was dissolved in deaerated water sufficient to fill up the pores of native Mo_2C, as predetermined via

N_2 physisorption. The solution was added dropwise to the native Mo_2C with rigorous shake to ensure adequate dispersion. The resulting materials was and treated in two ways: (1) dried on the heating plate for 3 hours without reduction (K_NR/Mo_2C) (2) dried on the heating plate for 3 hours and then be reduced in H_2 at 450 °C following the temperature program described above, to acquire the native K modified Mo_2C (K_R/Mo_2C). Thus, we can determine if the presence of counterion of the K precursor would affect the following Cu deposition. The as-prepared K/Mo_2C catalysts were transferred and soak in Cu precursor solution using the wet impregnation method described earlier in this section to deposit Cu onto K/Mo_2C. 1 mL of the wet impregnation solution sample was taken before and after the deposition and examined via elemental analysis.

3.2.2 Material Characterizations

3.2.2.1 X-ray diffraction

The bulk phase crystal structure of the materials was determined via x-ray diffraction using a Rigaku Miniflex diffractometer equipped with a Cu Kα (λ = 0.15404 nm) radiation source and a Ni filter. Detailed experiment procedures can be found in Chapter 2.

3.2.2.2 N_2 Physisorption Analysis

The surface area of the catalysts was determined using the N_2 physisorption isotherm and the Brunauer-Emmett-Teller (BET) theory. Approximately 100 mg of sample was loaded into a BET tube, degassed at 350 °C for 5 hours, prior to performing analysis. Detailed experiment procedures were described previously in Chapter 2.

3.2.2.3 Elemental Analysis

The compositions of the Mo_2C-based catalysts were determined via elemental analysis performed using Inductively Coupled Plasma-Optical Emission Spectroscopy (ICP-OES) with a Varian 710-ES spectrometer. Approximately 15 mg of catalysts was added into 3 mL of aqua regia

(0.75 mL of hydrochloric acid and 2.25 mL of nitric acid), where the solution was left overnight to ensure complete dissolution of the metals. The as-prepared solution was diluted, and the composition was analyzed by comparing the wavelength intensities of elements with the intensities of known concentration standards.

3.2.3 Reaction Rate and Selectivity Measurement

15 to 25 mg of Mo_2C-based catalysts were loaded into the U-shape quartz reactor, supported with quartz wool, and diluted with low surface area SiO_2 (Alfa Aesar) to maintain consistent bed height for all experiments. Prior to performance evaluation, all Mo_2C-based catalysts were pretreated with 15% CH_4 in H_2 (100 mL/min, Cryogenic Gases) at 590 °C for 4 hours with a ramp rate of 9.4 °C/min to remove the passivation layer. After the pretreatment, the reactor was cooled down to 240 °C, the temperature that is typical for low temperature WGS [1,17]. Once reaching 240 °C, the gas was changed from 15% CH_4/H_2 to the reaction condition, as described in Chapter 2. The reaction was held at 240 °C for 10 hours for catalyst deactivation, and subsequently treated in two different ways: (1) held for another 3 hours to collect the reaction rates data in the pseudo-steady-state regime. Liquid products produced in pseudo-steady-state was collected with a separate round flask purged with N_2. (2) varied reaction temperature following the order of 200 °C, 230 °C, 210 °C, 220 °C, and back to 240 °C to obtain an Arrhenius plot. The reaction was held at each temperature for 2 hours before returning to 240 °C. After returning to 240 °C, the reaction was held for 3 hours before the termination of the experiment. The liquid products produced during deactivation (240 °C), temperature variation (200 to 230 °C), and final pseudo-steady-state regime (240 °C) were collected and analyzed separately. Detailed system of design can be found in the Method section of Chapter 2.

In regeneration experiments, the reactor and the catalyst was first cooled down the room temperature under N_2 flow. The catalyst was then treated with 15% CH_4 in H_2 (100 mL/min, Cryogenic Gases) at 590 °C for 4 hours with a ramp rate of 9.4 °C/min to remove species blocking the active sites on the catalyst. After the pretreatment, the reactor temperature was cooled to 240 °C as previously described and an identical experiment was performed. The spent catalyst was transferred from the reactor to a vial purged with N_2, then transferred to the 2920 chemisorption system to minimize exposure to air. The spent Mo_2C was pretreated again with 15% CH_4 in H_2 (100 mL/min, Cryogenic Gases) at 590 °C for 4 hours before performing CO chemisorption.

3.3 Results

3.3.1 Catalyst Characterization

The surface area, metal loading, CO chemisorption uptake, and NH_3 chemisorption uptake of the Mo_2C supported metal catalysts are listed in Table 3.1. As can be seen, for 0.1 ML surface coverage, the surface areas were relatively similar and did not change significantly upon deposition of the metal. This indicates the admetals did not block the pores of the support. When the nominal loading of metal increased to 0.5 ML, the surface area of the catalysts dropped, which suggests metal particles blocking surface pores.

Table 3.1 Surface and physical properties for the Mo_2C based catalysts synthesized via wet impregnation.

Catalysts	Surface Area (m^2/g)	Metal Loading (wt%)	CO Uptake (μmol/g)	NH_3 Uptake (μmol/g)
Mo_2C	99	---	297	155
0.1 ML Pt/Mo_2C	101	3.9	318	157
0.1 ML Cu/Mo_2C	93	1.0	296	152
0.1 ML Au/Mo_2C	85	3.7	272	168
0.5 ML Cu/Mo_2C	61	4.6	263	112
0.5 ML Cu/K_NR/Mo_2C	60	4.8 (Cu), 0.04 (K)	290	--
0.5 ML Cu/K_R/Mo_2C	83	4.4 (Cu), 0.04 (K)	235	--

Diffraction patterns for the materials are shown in Figure 3.1. As mentioned previously, the Mo_2C synthesized here is a mixture of α-MoC_{1-x} and β-Mo_2C. The absence of peak signals in the XRD patterns for Cu, Au and Pt-based Mo_2C catalysts suggests that the metal domains were small and well dispersed.

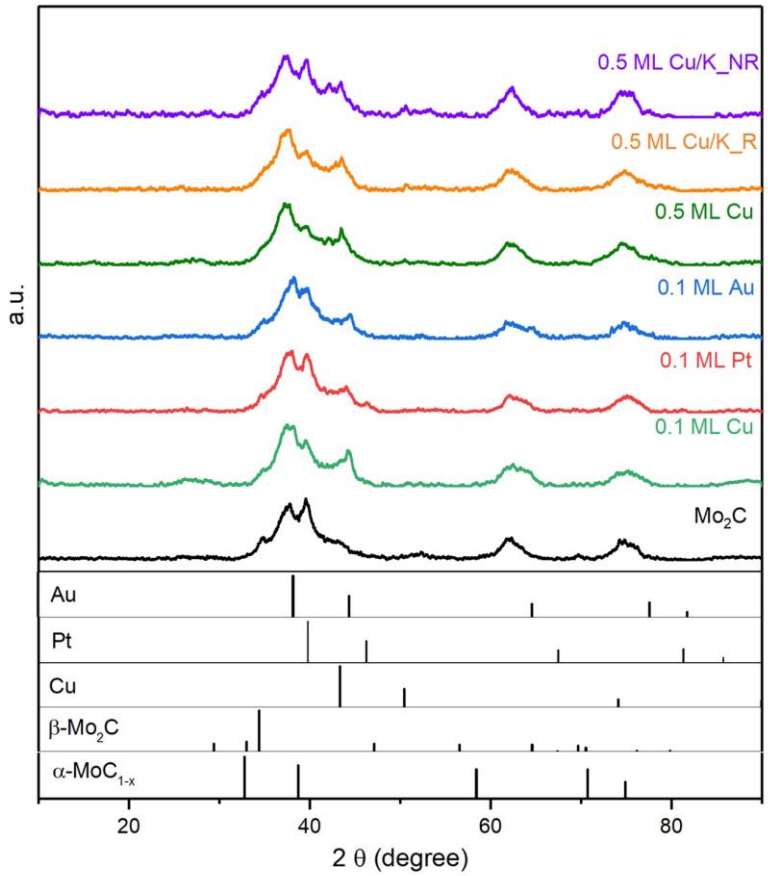

Figure 3.1 Diffraction patterns for Mo_2C-supported metal catalysts and relevant standards: Pt (JCPDF 00-004-0802), Au (JCPDF 00-004-0787), Cu (JCPDF 00-004-0836), α-MoC_{1-x} (JCPDF 00-015-0457), β-Mo_2C (JCPDF 00-035-0787).

Based on the results of elemental analysis, the amount of metal deposited on the surface is similar to nominal loading for 0.1 ML Cu/Mo_2C, Pt/Mo_2C, Au/Mo_2C catalysts, and 0.5 ML Cu/Mo_2C. The actual loadings determined were 0.1 ML Cu, 0.12 ML Pt, 0.11 ML Au, and 0.46 ML Cu, respectively. To study the effects of high loading, an effort to increase Cu loading to 0.7 ML was made. However, the Mo_2C surface saturated at 0.47 ML Cu and the loading could not be further increased. Additionally, the attempt of synthesizing Cu/K/Mo_2C catalysts did not success. When K/Mo_2C particles were soaked in a Cu precursor solution, blue precipitate was observed for both batches, as shown in Figure 3.2.

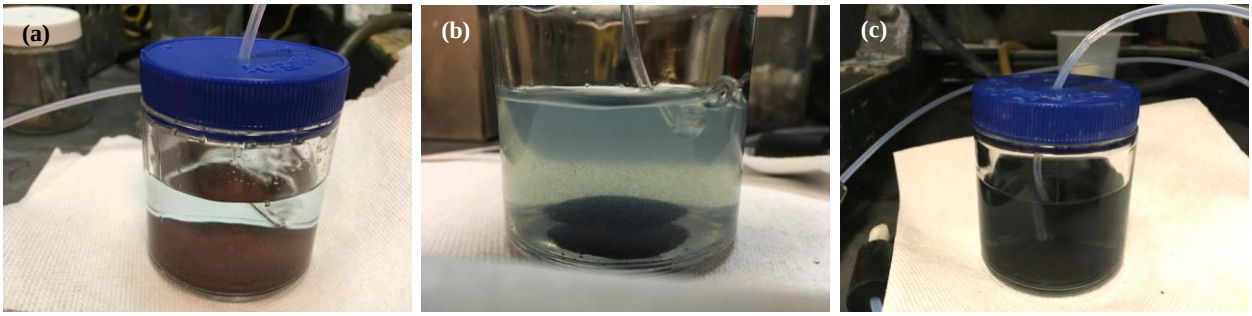

Figure 3.2 Pictures taken after adding the Mo_2C catalysts into the Cu precursor solution. (a) Mo_2C. The solution remains clear and no precipitate observed. (b) K_NReduce/Mo_2C (K/Mo_2C without reduction). Blue precipitate observed. (c) K_Reduce/Mo_2C (K/Mo_2C reduced at 450 °C). Blue precipitate observed.

To investigate the identity of the blue precipitate, a control experiment was conducted using a 50 mL solution containing K precursor and Cu precursor. The concentrations of each metal were similar to the concentration used in the actual synthesis. In the solution containing K precursor and Cu precursor, the formation of blue precipitate was observe. After centrifuging, the blue precipitate was collected and dried overnight for XRD analysis. The XRD pattern of the precipitate suggests that the blue precipitate formed was Malachite, $Cu_2(OH)_2(CO_3)$, as shown in Figure 3.3.

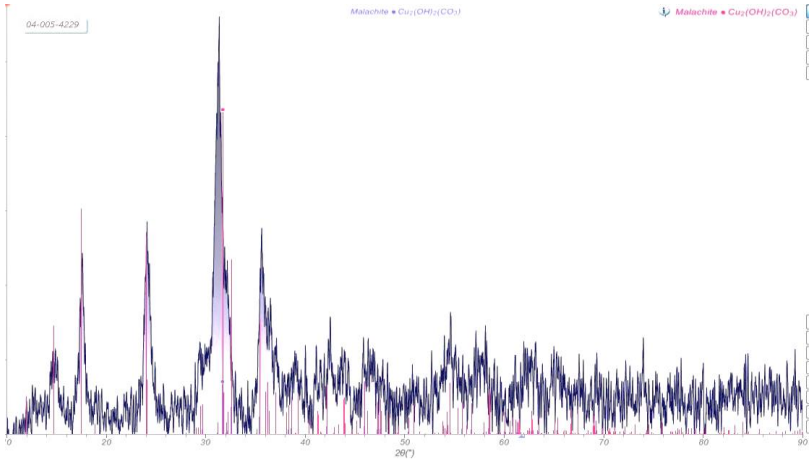

Figure 3.3 The XRD pattern of the blue precipitate and Malachite $Cu_2(OH)_2(CO_3)$ standard pattern from the Jade database (red line).

Based on the elemental analysis of the precursor solution and final catalyst products (Table 3.1), the K on both K_R/Mo_2C and K_N/Mo_2C did not remain on the Mo_2C surface. Instead, almost all the K on Mo_2C bleached into the Cu precursor solution. For both K_R/Mo_2C and K_N/Mo_2C, the loading results of Cu were similar to Cu deposition on bare Mo_2C. This indicates that the presence of K solution did not appear to be affect the deposition of Cu.

3.3.2 Aldehyde Water Shift Activity

As discussed earlier in Chapter 2, the AWS was concluded to be the major source of H_2. Thus, the H_2 production was used to measure the AWS reaction. In addition to acetic acid and H_2, several other carbon containing products were formed. These products and associated reactions will be discussed in section 3.3.3.

In catalyst evaluation experiments, all catalysts deactivated during the first several hours on stream (see Figure 3.4). At 240°C, the H_2 production rates reached a pseudo-steady state after ~10 hours for the M/Mo_2C materials. The AWS activity of Cu-Zn-Al, the benchmark catalyst, decayed about 20%, and the activity of M/Mo2C catalysts decayed 35-40%.

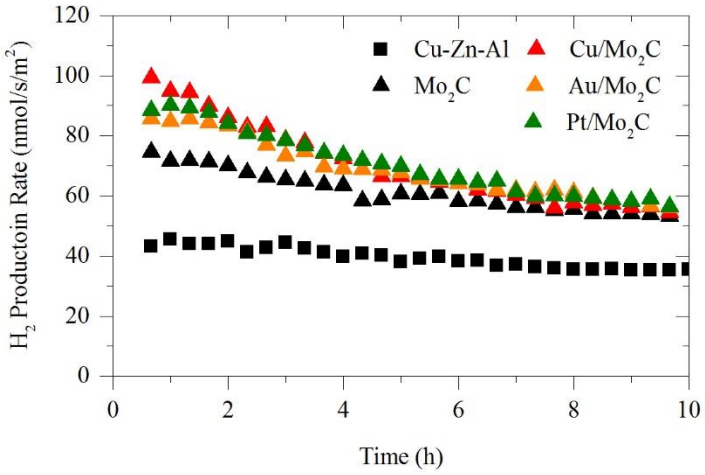

Figure 3.4 Deactivation profiles of 0.1 ML M/Mo_2C and Cu-Zn-Al catalysts at 240°C.

The deactivation profiles were fit to empirical decay models to understand the deactivation mechanism, as shown in Table 3.2. Reciprocal power and hyperbolic models produced better fits

for all Mo_2C-based catalysts; the exponential models also fitted Mo_2C well. The reciprocal model is typically associated with deactivation by surface fouling or carbon deposition, while hyperbolic decay model often suggests sintering and exponential decay implies site poisoning [18,19]. Given that the reciprocal power fitted Mo_2C-based catalysts reasonably well and catalysts subjected to fouling can often be regenerated [20], regeneration experiments were carried out for selected Mo_2C-based catalysts and will be discuss later in this section.

Table 3.2 Results from nonlinear regression of 0.1 ML M/Mo_2C catalysts to empirical decay rate laws.

Catalyst	Type	Linear	Exponential	Hyperbolic	Reciprocal Power
	Differential form	$-da/dt = k_d a$	$-da/dt = k_d a$	$-da/dt = k_d a^2$	$-da/dt = k_d A_0^{1/5} a^m$
	Integral form	$a = 1 - k_d t$	$a = e^{-k_d t}$	$a = 1/1 + k_d t$	$a = A_0 t^{-k_d}$
Cu-Zn-Al	k_d (h^{-1})	0.014	0.015	0.017	0.092
	A_o	---	---	---	1.043
	R_{adj}^2	0.0824	**0.0839**	**0.847**	0.799
Mo_2C	k_d (h^{-1})	0.0337	0.039	0.044	0.135
	A_o	---	---	---	0.994
	R_{adj}^2	0.920	**0.947**	**0.958**	0.930
0.1 ML Cu/Mo_2C	k_d (h^{-1})	0.04175	0.055	0.072	0.250
	A_o	---	---	---	1.052
	R_{adj}^2	0.8175	0.915	**0.948**	**0.978**
0.1 ML Pt/Mo_2C	k_d (h^{-1})	0.031	0.041	0.053	0.224
	A_o	---	---	---	1.073
	R_{adj}^2	0.800	0.905	**0.946**	**0.948**
0.1 ML Au/Mo_2C	k_d (h^{-1})	0.0267	0.034	0.043	0.178
	A_o	---	---	---	1.039
	R_{adj}^2	0.599	0.730	0.806	**0.858**

The pseudo-steady-state AWS rates of Mo_2C supported metal catalysts are provided in Table 3.3. As can be seen, the bare Mo_2C catalyst showed a rate substantially higher (50 nmol/s/m^2) than the benchmark Cu-Zn-Al catalysts, which had a rate of 27.8 nmol/s/m^2. In contrast to metal oxide supported metal catalysts, which the admetals changed reactivity of catalysts dramatically, the deposition of 0.1 ML admetal did little to promote the activity of Mo_2C. The 0.1

ML M/Mo_2C catalysts showed AWS rates of 54-57 nmol/s/m^2, which is only slightly higher than that for the bare Mo_2C (50 nmol/s/m^2).

Table 3.3 AWS rates and turnover frequencies at 240 °C and activation energies for the various catalysts.

Catalysts	AWS Rate (nmol/s/m^2)	AWS Turnover Frequency (1/s)	Activation Energy (kCal/mol)
Cu-Zn-Al	27.8	0.0034	22
Mo_2C	50.3	0.0166	14
Cu/Mo_2C	54.5	0.0172	13
Pt/Mo_2C	56.6	0.0262	13
Au/Mo_2C	56.8	0.0177	14
0.5 ML Cu/Mo_2C	86.2	0.0200	15
0.5 ML Cu/K_NR/Mo_2C	83.5	0.0295	14
0.5 ML Cu/K_R/Mo_2C	96.8	0.0200	15

When metal loading was further increased from 0.1 ML to 0.5ML, the enhancement in AWS activity became more significant. The 0.5 ML Cu/Mo_2C catalyst had an AWS rate of 86 nmol/s/m^2, which was a 70% enhancement comparing with the bare Mo_2C. For both 0.5 ML Cu/K_R/Mo_2C and Cu/K_NR/Mo_2C, the AWS activities were similar to the 0.5 ML Cu/Mo_2C.

To access the intrinsic activity of catalysts, CO chemisorption uptakes were used to determine AWS turnover frequencies by normalizing the AWS rates with CO site densities (see Table 3.1). The results indicate that the Mo_2C based catalysts are intrinsically more active than the CeO_2- and Al_2O_3- supported metal catalysts. Among all metal oxide supported metal catalysts investigated in Chapter 2, Cu/CeO_2 and Cu-Zn-Al had the highest AWS activities, which were 0.0088 mol H_2/s/mol_{Cu} and 0.0034 mol H_2/s/mol_{Cu}, respectively.

The apparent activation energies of M/Mo_2C observed were similar to those of the bare Mo_2C, while the E_a were lower than those found for Cu-Zn-Al and Cu/CeO_2, which had E_a of 22 and 19 kCal/mol, respectively. The corresponding Arrhenius plots for Mo_2C supported metal catalysts are provided in Figure 3.5.

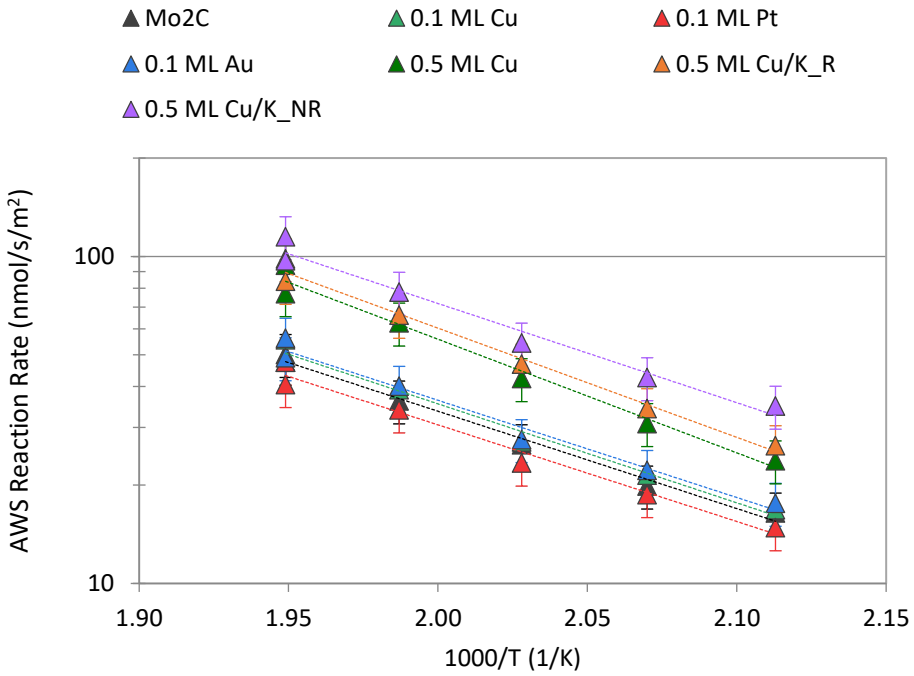

Figure 3.5 Arrhenius plots of the AWS reaction rates for Mo_2C supported metal catalysts.

As mentioned earlier in the deactivation discussion, the deactivation of Mo_2C-based catalysts could be attribute to surface fouling, and can often be regenerated [20]. In regeneration experiments, selected spent Mo_2C-based catalysts were pretreated with 15% H_2/CH_4 at 590 °C, which was the same procedure employed during activation and prior to CO chemisorption. The pseudo-steady-state reaction rates for the regenerated Mo_2C (49 nmol/s/m^2 at 240 °C) were nearly identical the fresh catalyst (50 nmol/s/m^2 at 240 °C). The site density determined via CO uptake for the regenerated material (298 µmol/g) was also very similar to the uptake for the fresh Mo_2C catalyst (297 µmol/g), which indicates the successful regeneration.

3.3.3 Selectivity

In addition to acetic acid, M/Mo_2C also produced significant amounts of ethanol and small amount of crotonaldehyde. Formation rates of acetic acid, ethanol and crotonaldehyde are provided in Table 3.4.

Table 3.4 Stabilized ethanol and crotonaldehyde production rates at 240 °C after 10 hours deactivation on stream.

Catalysts	Acetic Acid Rate ($nmol/s/m^2$)	Ethanol Production Rate ($nmol/s/m^2$)	Crotonaldehyde Production Rate ($nmol/s/m^2$)
Mo_2C	110.9	64.3	3.4
0.1 ML Cu/Mo_2C	98.8	45.5	3.1
0.1 ML Pt/Mo_2C	120.5	57.0	3.1
0.1 ML Au/Mo_2C	115.4	64.8	3.3
0.5 ML Cu/Mo_2C	143.0	65.3	4.7
0.5 ML $Cu/K\_NR/Mo_2C$	147.0	69.2	1.9
0.5 ML $Cu/K\_R/Mo_2C$	120.4	58.1	3.3

During a control experiment where only H_2 and acetaldehyde were fed to the Mo_2C catalyst, very little ethanol was detected and there was no evidence of H_2 consumption. This suggests that acetaldehyde hydrogenation was not the source of ethanol. Instead, we believe that the ethanol was produced via the Cannizzaro reaction [21,22]. Note that acetic acid is a common product of both AWS and Cannizzaro reaction. The formation rate of acetic acid during the reaction approximately equals the sum of the rates of AWS and Cannizzaro reaction (within 15% error) for Mo_2C-based catalysts and Cu-Zn-Al. These results are consistent with previous conclusions that AWS reaction was the source of H_2 and ethanol was produced via Cannizzaro reaction. On the other hand, The crotonaldehyde is likely a product of aldol condensation [23–26]. The carbon selectivities to the

carbon containing products are shown in Figure 3.6. For all M/Mo_2C catalysts, the carbon selectivity is relatively similar, between 60-65% to acetic acid.

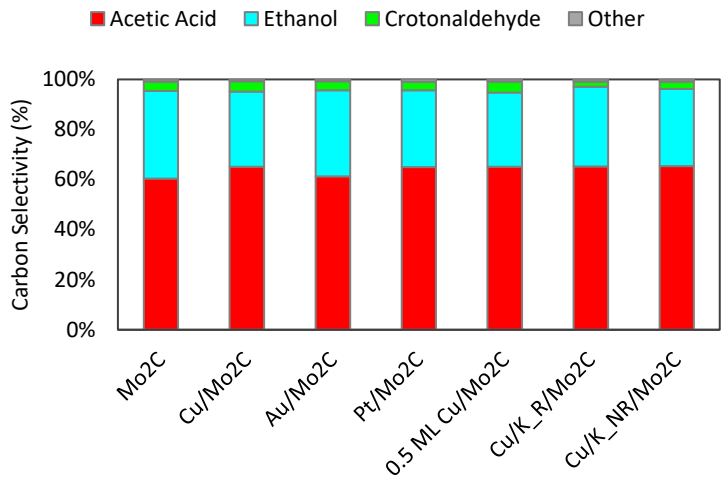

Figure 3.6 Carbon selectivities for M/Mo_2C catalysts. The selectivity is defined as the moles of acetaldehyde reacted to form certain product divided by the total amount of acetaldehyde converted.

3.4 Discussion

In this chapter, the physical, chemical and catalytic properties of a series of Mo_2C supported metal catalysts for the AWS reaction were investigated. This investigation demonstrates that the bare Mo_2C is an excellent catalyst for AWS, and its activity for AWS was two times or more active compared to the benchmark catalyst Cu-Zn-Al and other supported metal catalysts. The high activity of the Mo_2C could be attribute to the presence of various types of sites on the catalyst surface. Based on the conclusions of Chapter 2, it is likely that the intimacy between water dissociation sites and aldehyde oxidation sites could lead to high AWS activity. As previously reported, Mo_2C is able to activate and dissociate water efficiently, forming adsorbed OH* and H* on the catalysts surface [5,6]. Additionally, acetaldehyde was reported to adsorb on the Lewis acid and Mo sites via the O lone pair on the aldehyde [12,27]. With the presence of those unique properties, it is not surprising that the Mo_2C is highly active for AWS. Upon the depositions of

Cu, Pt, and Au on the Mo_2C surface, the initial AWS rates of M/Mo_2C were ~40% higher compared to that for the bare Mo_2C. However, the AWS rates of M/Mo_2C decayed to a level similar to the bare Mo_2C after reaching the pseudo-steady-state regime. These observations differ from that described for similar materials during WGS [1,2], in which the deposition of metals onto Mo_2C had a significant effect on the initial and steady state WGS rates.

To gain further insight into the deactivation, the deactivation profiles were fitted using empirical decay models. Based on the results of the fittings, deactivation of the Mo_2C-based could due to surface fouling. Using x-ray photoelectron spectroscopy to characterize catalyst surface, Lausche et al. reported that during methanol steam reforming (MSR) over Mo_2C, C=O and C-O species accumulated on the surface, which may due to the formation of carbonate or formate, and could be the cause of deactivation for MSR [19]. Schaidle et al. also proposed that carbonate and formate formation caused the deactivation of Mo_2C during WGS reaction [28]. It is likely that carbonate and acetate could also explain the deactivation of Mo_2C during AWS. Given that the deactivation due to surface fouling are often reversible [20], regeneration of M/Mo_2C was attempted. In regeneration experiments, the CO active site density and reactivity measurements of fresh and spent catalysts were very similar. Together, these results are consistent with a surface fouling versus a poisoning mechanism, and the ability of Mo_2C to be regenerated would make it an ideal catalyst for industrial application.

As discuss earlier, 0.1 ML M/Mo_2C had higher initial AWS rates but decayed to the level of Mo_2C. In attempt to better understand the promotion effects of admetal, the loading of Cu deposited on Mo_2C was increased. However, the Mo_2C surface saturated at ~0.5 ML of Cu loading and higher monolayer loadings could not be achieved. This phenomenon is speculated to be an effect of point-of-zero-charge (PZC). The PZC for the native Mo_2C was reported to be

approximately pH 5 [14,29], and the pH value for the Cu precursor solution for nominal loading at 0.7 ML was approximately 4.85. When the solution pH is below the PZC of the catalyst, the catalyst surface could be slightly protonated [30], which may prevent the Cu^{2+} ion to be in contact with the Mo_2C surface.

As the loading of Cu increased from 0.1 ML to 0.5 ML, enhancement in AWS activity became apparent. For 0.5 ML Cu/Mo_2C, the activity in AWS reaction was increased by ~70% compared to that for the bare Mo_2C, and the selectivity remained relatively similar. Given that the apparent activation energies for all M/Mo_2C catalysts were similar, namely E_a of 13 ± 2 kCal/mol, these results suggest that the rate-limiting step was governed by the Mo_2C support and was not altered by the admetals. As the rate-limiting-step remained the same, the enhancement in AWS activity after increasing Cu loading could due to the additional aldehyde adsorption sites created by the deposited Cu [31], which provided adequate aldehyde adsorption for high turnover of the AWS reaction as the Mo_2C supplied the oxygen from H_2O dissociation.

Aside from the AWS activity, high selectivity was also observed on Mo_2C-based catalysts, which were 60-65% selective to acid. This resembled the best-performed metal oxide catalysts found in Chapter 2, namely Cu-Zn-Al and Cu/CeO_2. Interestingly, unlike the metal oxide catalysts, the major side product for Mo_2C-based catalysts was ethanol, a product of Cannizzaro reaction. As reported in Chapter 2, the Cu-based materials showed higher rates of Cannizzaro reaction, potentially because the Cu metal can activate water. As Mo_2C can activate water facilely, this may explain the higher rate of Cannizzaro reaction observed on Mo_2C. To investigate the relation between the surface acid-base properties and the selectivity, K was selected to deposit onto the Mo_2C. However, elemental analysis results revealed that the K deposited prior to Cu deposition bleached out during Cu wet impregnation, regardless of whether the K/Mo_2C underwent reduction.

As K did not stayed on the Mo_2C surface, the Cu depositions did not appear to be affected and loading of Cu still reached the 0.5 ML saturation level. Consequently, it is not surprising that the 0.5 ML Cu/K/Mo_2C had similar surface properties and reactivity to the 0.5 ML Cu/Mo_2C.

For future preparation of Cu/K/Mo_2C catalysts, incipient wetness impregnation technique is required to ensure the deposited K will remain on the Mo_2C surface. As 0.5ML is the maximum loading of Cu when synthesized via wet impregnation, if a targeted Cu loading is above 0.5 ML, the Cu/Mo_2C also need to be prepared via incipient wetness impregnation.

3.5 Conclusion

In summary, the reactivity of a series of Mo_2C supported metal catalysts was investigated as catalysts for the AWS reaction. The bare Mo_2C was found to be ~80% or more active in comparison to the benchmark Cu-Zn-Al and other metal oxide supported metal catalysts. The selectivity of Mo_2C to acid was ~60%. The selectivity is similar to those of the best-performed metal oxide catalysts found in Chapter 2, namely Cu-Zn-Al and Cu/CeO_2. For M/Mo_2C catalysts, at low metal loading (0.1 ML) of Cu, Pt, and Au, the initial rates for AWS were enhanced by 40%; but after deactivation, the activity decayed to a level similar to the bared Mo_2C. When Cu loading was further increased, the Mo_2C reached surface saturation at 0.5 ML Cu deposition, where the AWS activity was enhanced by ~70%. This indicate there may exist synergetic effects between the support and the admetal, or a bifunctional mechanism, which promoted the activity for AWS. Despite the enhancement in AWS activity, no obvious enhancement in selectivity was observed. The apparent activation energies of M/Mo_2C remained similar to the bare Mo_2C, which suggests that rate limiting step was governed by the Mo_2C support and not altered by the admetal. Given that the rate-limiting-step remained the same, it is likely the Cu admetal provided additional sites for aldehyde adsorption, which reacted with the adjacent oxygen released by the Mo_2C from H_2O

dissociation. With the presences of site for water dissociation and aldehyde adsorption (i.e. the bifunctional mechanism), a higher AWS rate could be achieved.

Aside from the investigation of AWS activity, the present research also attempted to understand the relation between surface properties and selectivity via the deposition of K. This was not successful because the deposited K bleached off during the synthesis process, and no promotion effect was observed in the study.

A greater understanding of characteristics of the activity will aid in designing effective catalysts for the AWS reaction. The investigation of identity of the active sites will be discussed in the next chapter.

3.6 References

[1] N. M. Schweitzer, J. A. Schaidle, O. K. Ezekoye, X. Pan, S. Linic, L. T. Thompson, J. Am. Chem. Soc. 133 (2011) 2378–2381.

[2] K. D. Sabnis, Y. Cui, M. C. Akatay, M. Shekhar, W. S. Lee, J. T. Miller, W. N. Delgass, F. H. Ribeiro, J. Catal. 331 (2015) 162–171.

[3] L. Lin, W. Zhou, R. Gao, S. Yao, X. Zhang, W. Xu, S. Zheng, Z. Jiang, Q. Yu, Y.-W. Li, C. Shi, X.-D. Wen, D. Ma, Nature. 544 (2017) 80–83.

[4] S. Yao, X. Zhang, W. Zhou, R. Gao, W. Xu, Y. Ye, L. Lin, X. Wen, B. Chen, E. Crumlin, J. Guo, Z. Zuo, W. Li, J. Xie, L. Lu, C.J. Kiely, L. Gu, C. Shi, J. A. Rodriguez, D. Ma, Science. 4321 (2017) 1–10.

[5] P. Liu, J. A. Rodriguez, Phys. Chem. B. 110 (2006) 19418–19425.

[6] X. Tian, T. Wang, H. Jiao, Catal. Sci. Technol., 7 (2017) 2789–2797.

[7] M. J. L. Ginés, N. Amadeo, M. Laborde, C. R. Apesteguía, Appl. Catal., A. 131 (1995) 283–296.

[8] A. A. Gokhale, J. a. Dumesic, M. Mavrikakis, J. Am. Chem. Soc. 130 (2008) 1402–1414.

[9] K. D. Sabnis, M. C. Akatay, Y. Cui, F. G. Sollberger, E. A. Stach, J. T. Miller, W. N. Delgass, F. H. Ribeiro, J. Catal. 330 (2015) 442–451.

[10] Y. Ma, G. Guan, X. Hao, Z. Zuo, W. Huang, P. Phanthong, K. Kusakabe, A. Abudula, RSC Adv. 4 (2014) 44175–44184.

[11] J. Cao, Y. Ma, G. Guan, X. Hao, X. Ma, Z. Wang, K. Kusakabe, A. Abudula, Appl. Catal., B 189 (2016) 12–18.

[12] M. Siaj, I. Temprano, N. Dubuc, P. H. Mcbreen, J. Organomet. Chem.691 (2006) 5497–5504.

[13] X. Liu, S.J. Ardakani, K.J. Smith, Catal. Commun. 12 (2011) 454–458.

[14] J. A. Schaidle, N. M. Schweitzer, O. T. Ajenifujah, L. T. Thompson, J. Catal. 289 (2012) 210–217.

[15] Y. Chen, S. Choi, L. T. Thompson, J. Catal. 343 (2016) 147–156.

[16] Y. Chen, S. Choi, L. T. Thompson, Catal. Today 259 (2016) 285–291
[17] C. Ratnasamy, J. P. Wagner, Catal. Rev. 51 (2009) 325–440.
[18] H.S. Fogler, Elements of Chemical Reaction Engineering, forth ed., Pearson Education, Inc. Upper Saddle River, New Jersey, 2006
[19] A. C. Lausche, J. A. Schaidle, L. T. Thompson, Appl. Catal., A. 401 (2011) 29–36.
[20] M. D. Argyle, C. H. Bartholomew, Catalysts 5 (2015) 145–269.
[21] T. P. Brewster, W. C. Ou, J. C. Tran, K. I. Goldberg, S. K. Hanson, T. R. Cundari, D. M. Heinekey, ACS Catal. 4 (2014) 3034–3038.
[22] M. Watanabe, M. Osada, H. Inomata, K. Arai, A. Kruse, Appl. Catal., A. 245 (2003) 333–341.
[23] J. E. Rekoske, M. A. Barteau, Langmuir 15 (1999) 2061–2070.
[24] M. J. Climent, A. Corma, V. Fornés, R. Guil-Lopez, S. Iborra, Adv. Synth. Catal. 344 (2002) 1090–1096.
[25] H. Idriss, K.S. Kim, M. A. Barteau, J. Catal. 139 (1993) 119–133.
[26] H. Idriss, C. Diagne, J.P. Hindermann, A. Kiennemann, M.A. Barteau, J. Catal. 155 (1995) 219–237.
[27] J. Raskó, J. Kiss, Appl. Catal., A. 287 (2005) 252–260.
[28] J. A. Schaidle, A. C. Lausche, L. T. Thompson, J. Catal. 272 (2010) 235–245.
[29] B. M. Wyvratt, J. R. Gaudet, L. T. Thompson, J. Catal. 330 (2015) 280–287.
[30] J. Park, J. R. Regalbuto, J. Colloid Interface Sci. 175 (1995) 239–252.
[31] M. Bowker, R. J. Madix, Appl. Surf. Sci. 8 (1981) 299–317.

Chapter 4

Investigation of Active Sites on Mo_2C Supported Metal Catalysts

4.1 Introduction

In Chapter 3, we demonstrated that Mo_2C catalysts are highly active for the aldehyde water shift (AWS) reaction. The AWS activities of the catalysts were further enhanced upon the metal deposition on the Mo_2C surface. The deposition of 0.5 ML Cu on Mo_2C enhanced the AWS rate by ~70% compared to that of the bare Mo_2C. For all Mo_2C-based catalysts investigated in Chapter 3, the selectivity to acetic acid was 60-65%. Ethanol was produced as the major side products via Cannizzaro reaction for all of the Mo_2C-based catalysts, with the selectivity to ethanol in the range of 35-30%. Despite the high activities observed, respective roles of the Mo_2C support and the Cu admetal remain unclear. To further understand the chemistry of AWS reaction on the Mo_2C-based catalysts, the aim of the research described in the chapter is to investigate the characteristics of the active sites for the AWS and side reactions. With the lack of mechanistic studies and reports for AWS over supported metal catalysts in the literature, the methodology employed here was adopted from research for water gas shift (WGS) reaction and CO oxidation. For the WGS reaction, numerous research attributes the activity enhancement from the metal loading to a bifunctional mechanism, in which the admetal provides additional sites for CO adsorption and the support dissociates water to provide oxygen for the CO oxidation [1–4]. The reaction can be facilitated via promoting close proximity of these two types of sites, which is typically correlated to the periphery of the admetal particles (e.g. at the interface between the admetal and the support).

Given the difficulty to directly monitor the adsorbed reactants and the progress of the reaction, the bifunctional mechanism is generally established from the characteristics of the active sites and the known surface chemistry of the catalyst. For Pt/Mo_2C, one of the most WGS active catalysts, Schweitzer et al. examined the WGS activities as a function of Pt loading. By correlating the Pt loading with particle size, they compared the activity results with various active site models derived from different active site locations, and reported that the perimeter active site model agreed well with the experimental rate data. They concluded that the active sites were located primarily at the periphery of Pt particles, and the high WGS activities for Pt/Mo_2C were attributed to a bifunctional mechanism [1]. Similar conclusions were drawn from the experiment results for other admetals supported on Mo_2C, such as Au, Cu, Pd, and Ni [2]. These experimental observations also agree well with the computational works. For WGS, Lin et al. computationally demonstrated that the active sites of Pt/α-MoC were located at the interfacial sites of Pt and α-MoC [5]. A report of Yao et al. drew the same conclusion for Au/α-MoC; CO adsorbs on Au sites, and then reacts with the nearby OH split from water on α-MoC (111) sites [4]. Similar investigation was also reported for CO oxidation reactions. Cargnello et al. investigated the reactivity of CO oxidation over CeO_2 supported Ni, Pd, and Pt catalysts. By controlling the admetal particle sizes, they correlated the particle sizes with the catalyst activities and concluded that the ceria-metal interface sites were key to high CO oxidation activities, where admetal provide sites for CO adsorption and CeO_2 sites provide oxygen via the formation of oxygen vacancies [6].

Inspired by these pioneering works, the particular interest of this chapter is to investigate the characteristics of active sites for the AWS reaction by varying the particle size of the Cu admetal and correlating that with reactivity. To manipulate the particle size of the Cu admetal, 0.1 ML to 2.0 ML of Cu were deposited on Mo_2C. As described in Chapter 3, the Cu deposition on Mo_2C

reached saturation at approximately 0.5 ML when using wet impregnation for the metal loading. Consequently, Cu was deposited via incipient wetness impregnation in this chapter to achieve higher metal loadings. Along with the characterization experiments, the reactivity of the Cu/Mo_2C catalysts were evaluated. The AWS rates attributed to Mo_2C surface and Cu admetal were deconvoluted; the AWS rates of Cu were further correlated with Cu loadings using mathematical models derived with the locations of the active site. Per our hypothesis of the bifunctional mechanism, the interface of Cu-Mo_2C on Cu/Mo_2C is expected to be critical to its activity for the AWS reaction.

Additional to the AWS activity, basing on previous discussions in Chapter 2 and 3, we speculated that the surface acid sites correlated with the major side reactions, the Cannizzaro and aldol condensation, as the acetaldehyde molecule is likely to adsorb on the acid sites [7]. Thus, by removing the surface acid sites, the selectivity may be improved. In Chapter 3, we attempted to manipulate the selectivity by depositing K on Mo_2C to remove the surface acidity, however, the K deposited bleached off during the following wet impregnation of Cu. Accordingly, in this chapter, the K/Mo_2C and Cu/K/Mo_2C catalysts were synthesized via incipient wetness impregnation and the correlations between the surface acidities and the side reactions were examined.

4.2 Experimental Methods

4.2.1 Materials and Methods

4.2.1.1 Catalyst Synthesis

The Mo_2C supported Cu catalysts discussed in this chapter were prepared via a temperature programmed reaction method, followed by the incipient wetness impregnation for the metal deposition. The preparation of the native Mo_2C was described in the Methods section in Chapter 2. Ammonium paramolybdate precursor was treated in H_2 at 350 °C for 12 hours then in 15%

CH_4/H_2 at 590 °C for 2 hours. After cooling down to room temperature (< 30 °C), the native Mo_2C (unpassivated) was transferred into an inert atmosphere glove box without exposure to air. The admetals were deposited onto the Mo_2C support using the incipient wetness impregnation method. Copper(II) nitrate hydrate ($Cu(NO_3)_2 \cdot 2.5H_2O$, Sigma-Aldrich) and potassium carbonate (K_2CO_3, Sigma-Aldrich) were used as precursors for Cu and K deposition, respectively [8]. The metal precursors were dissolved in deaerated water in quantities sufficient to fill the pore volume of the support as determined by the N_2 physisorption. The nominal surface coverages were 0.1, 0.25, 0.5, 0.75, 1.0, and 2.0 monolayers (ML) based on 10^{19} site/m^2. The precursor solution was added to the support in aliquots using a pipet until the support reaches incipient wetness point. Given the pyrophoric nature of Mo_2C, the metal depositions were performed in a water-tolerant N_2 glovebox to preserve the native properties and structure. After the metal deposition step, the materials were dried on a heating plate in the glovebox. If the amount of precursor used exceeded the maximum solubility (1.0 and 2.0 ML) and the precursor was not fully dissolved, additional amount of deaerated water was used. In such case, the solution was first added to the catalyst until incipient wetness was evident on the catalysts. The samples were then dried on the heating plate, and the precursor solution was added again to the catalyst to obtain the target metal loading then fully dried on the heating plate.

After drying, the catalyst was loaded into a quartz reactor on a quartz wool bed. The reactor was sealed with Parafilm in the glovebox and transferred to the furnace. The materials were then reduced in H_2, following the reduction process at 450 °C to reduce the metal domain and remove the counterions as described in Chapter 3 [9]. Finally, the materials were passivated in 1% O_2/He (20 mL/min, Cryogenic Gases) at room temperature for 7 hours [10]. The passivated catalysts were stored in an argon glovebox to prevent further oxidation. The Mo_2C supported bimetallic K and

Cu catalysts (Cu/K/Mo_2C) were prepared via a similar method. The K was first deposited to remove surface acid sites on Mo_2C. After drying, Cu was then deposited onto K/Mo_2C, aiming to create additional active sites. Following the K and Cu deposition, the materials were dried, reduced, and passivated as described above. In this Chapter, the catalyst with x ML nominal surface coverage of [Metal] is referred to as x ML [Metal]/Mo_2C. K modified Mo_2C supported Cu catalysts, with x ML nominal coverage of K and y ML for Cu, are referred to as y ML Cu/x ML K/Mo_2C.

4.2.1.2 X-ray Diffraction

The bulk phase crystal structure of the materials was determined via a x-ray diffraction using a Rigaku MiniFlex diffractometer equipped a Cu Kα (λ = 0.15404 nm) radiation source and a Ni filter. Detailed experiment procedures are described in Chapter 2.

4.2.1.3 N_2 Physisorption Analysis

The surface area of the catalysts was determined using the 7-point N_2 physisorption isotherm and the Brunauer-Emmett-Teller (BET) theory. Approximately 100 mg of sample was loaded into a BET tube, degassed at 350 °C for 5 hours, prior to performing analysis. Detailed experiment procedures were described previously in Chapter 2.

4.2.1.4 Elemental Analysis

The compositions of the Mo_2C-based catalysts were determined via elemental analysis performed with Inductively Coupled Plasma-Optical Emission Spectroscopy (ICP-OES) using a Varian 710-ES spectrometer. Briefly, ~15 mg of catalysts was added into 3 mL of aqua regia (0.75 mL of hydrochloric acid and 2.25 mL of nitric acid), and the resulting solution was left overnight to ensure complete dissolution. The as-prepared solution was then diluted, and the composition

was analyzed by comparing the wavelength intensities of the target elements with the intensities of standard solutions with known concentrations.

4.2.1.5 CO Chemisorption

The site densities for Mo_2C-based materials were probed via CO chemisorption with a Micromeritics ASAP 2920 instrument [1,8]. In a CO chemisorption experiment, the catalyst was first pretreated with 15% CH_4/H_2 at 590 °C for 4 h to remove the passivation layer; the process was identical to the treatment prior to the reactivity measurement experiment of the catalyst. Following the pretreatment, the material was degassed in He at 600 °C for 0.5 hours and cooled to 40 °C. The catalyst was then dosed with pulses of 5% CO/He repeatedly until surface saturation, at which point the active site densities were determined. Upon the saturation, the sample was purged in He for 0.5 hours to remove excess and physisorbed CO. In the final temperature programmed desorption (TPD), the catalyst was heated from 40 °C to 800 °C in He to desorb CO, and the desorbed species were observed via a mass spectrometer (MS). The CO desorption peaks were curve-fitted employing a nonlinear least squares method with Bi-Gaussian functions using Origin Data Analysis and Graphing Software.

4.2.1.6 NH_3 Chemisorption

NH_3 chemisorption and TPD were also performed to probe the surface acid site densities of the catalysts [11]. After the pretreatment, degas, and cooling processes as described in the previous CO Chemisorption section, the sample was soaked in NH_3 stream at 40 °C for 1 hour, then purged with He for 2 hours to remove excess and physisorbed NH_3. In the following TPD, the acid site densities were calculated from the amount of NH_3 desorbed.

4.2.2 Reaction Rate and Selectivity Measurement

Approximately 15 mg of Mo_2C-based catalyst was used in each performance evaluation experiment. The catalysts were loaded into the U-shape quartz reactor, supported by quartz wool, and diluted with low surface area SiO_2 (Alfa Aesar) to maintain the same bed height for all of the experiments. The catalyst was first pretreated at 590 °C (ramp rate 9.4 °C/min) in 15% CH_4/H_2 (100 mL/min, Cryogenic Gases) for 4 hours. After the pretreatment, the reactor was cooled down to 240 °C; the temperature that is typical for the low-temperature WGS [12], and much lower than the 300 °C or above reported for other heterogeneous catalysts for the AWS [13–15]. Upon reaching 240 °C, the gas stream flowed through the reactor was changed from 15% CH_4/H_2 to the reaction mixture, as described in Chapter 2. The reaction was first held at 240 °C for 10 hours for catalyst stabilization, and examined in two ways afterward. In the first method, the reaction was held at 240 °C for additional 3 hours to collect the reaction rate data in the pseudo-steady-state regime. Liquid products produced in pseudo-steady-state was collected with a new round flask purged with N_2 prior to installation. In a second method, the reaction temperatures were varied following the order of 200 °C, 230 °C, 210 °C, 220 °C, and back to 240 °C to acquire the Arrhenius plot. The reaction was held at each temperature for 2 hours before the rate measurement. Detailed system design can be found in the Method section of Chapter 2.

In the regeneration experiment, the reactor was cooled down to room temperature after the completion of the initial reaction, and reactivated in 15% CH_4/H_2 at 590°C for 4 hours. The reactivities were then measured using the procedures described above. The spent catalyst was transferred from the reactor to the 2920 chemisorption analyzer to determine the surface site density with minimal exposure to air. Prior to the CO chemisorption experiments, the spent Mo_2C was treated with the same activation procedure in 15% CH_4/H_2 at 590 °C.

4.2.3 Activity Deconvolution

For Cu/Mo_2C, the activities of the support and the admetal were deconvoluted using the equations shown below. The rate of Cu/Mo_2C is considered as the sum of the rate of exposed Mo_2C surface and the Cu admetal.

Cu/Mo_2C AWS rate: $r_{Cu/Mo_2C} = r_{Mo_2C,\ Cu/Mo_2C}$ (support) + $r_{Cu,\ Cu/Mo_2C}$ (admetal)

Based on the observation that the CO adsorption took place mostly on Mo_2C, the exposed Mo_2C surface (not covered by Cu) was estimated based on the amount of CO uptake relative to the bare Mo_2C. Also, the exposed Mo_2C surface is assumed to show similar activities as that of the bare Mo_2C. Consequently, the rate attributed to the exposed Mo_2C can be calculated.

Support (Mo_2C) AWS activity: $r_{Mo_2C,\ Cu/Mo_2C} = r_{Mo_2C,bare} \cdot \frac{Cu/Mo_2C\ \ CO\ uptake}{bare\ Mo_2C\ CO\ uptake}$

By subtracting the rate of the exposed Mo_2C from the rate of Cu/Mo_2C, the rate attributed to Cu can be obtained. With the calculation, individual contributions of the support and the admetal to the AWS activities were deconvoluted.

Admetal (Cu) AWS activity: $r_{Cu,\ Cu/Mo_2C} = r_{Cu/Mo_2C} - r_{Mo_2C,bare} \cdot \frac{Cu/Mo_2C\ \ CO\ uptake}{bare\ Mo_2C\ CO\ uptake}$

4.2.4 Active Site Model Derivation

The derivation of perimeter active site and surface active site models of the Cu admetal particles on the Mo_2C surface were based on the following set of assumptions [1]. The shape of Cu particles was assumed to be a hemisphere. The turnover frequency of each active site (TOF, mol/s/site), the total number of Cu particles present on the surface (n), and density of Cu (ρ_{Cu}) were assumed to be constants. Site density on Cu particles (q) is a constant for each model, and changes in the site density depend on the site location. At each loading, all the Cu particles were assumed to have the same size. The radius (R) of the particle is a function of loading. The weight

of Cu in catalysts is noted as W_{Cu} and the weight of catalyst is noted as W_{Cat}. X_{Cu} is the weight fraction of Cu in the catalyst (W_{Cu}/W_{Cat}) where W_{Cat} remains constant for all of the experiments.

For perimeter active site model:

$W_{Cu} = \rho_{Cu} \cdot n \cdot \left[\frac{1}{2} \cdot \frac{4}{3}\pi R^3\right]$, rearranged and got $R = \left(\frac{3W_{Cu}}{2\rho_{Cu}n\pi}\right)^{1/3}$

$$r\left(\frac{\text{mol AWS}}{\text{s} \cdot \text{mol Cu}}\right) = \frac{TOF}{W_{Cu}/_{MW_{Cu}}} \cdot n \cdot q \cdot [2\pi R] = \frac{TOF}{W_{Cu}} \cdot MW_{Cu} \cdot n \cdot q \cdot 2\pi \cdot \left(\frac{3W_{Cu}}{2\rho_{Cu}n\pi}\right)^{1/3} \sim {W_{Cu}}^{-2/3} \sim {X_{Cu}}^{-2/3}$$

For surface active site model:

$W_{Cu} = \rho_{Cu} \cdot n \cdot \left[\frac{1}{2} \cdot \frac{4}{3}\pi R^3\right]$, which $R = \left(\frac{3W_{Cu}}{2\rho_{Cu}n\pi}\right)^{1/3}$

$$r\left(\frac{\text{mol AWS}}{\text{s} \cdot \text{mol Cu}}\right) = \frac{TOF}{W_{Cu}/_{MW_{Cu}}} \cdot n \cdot q \cdot [2\pi R^2] = \frac{TOF}{W_{Cu}} \cdot MW_{Cu} \cdot n \cdot q \cdot 2\pi \cdot \left(\frac{3W_{Cu}}{2\rho_{Cu}n\pi}\right)^{2/3} \sim {W_{Cu}}^{-1/3} \sim {X_{Cu}}^{-1/3}$$

4.3 Results

4.3.1 Catalyst Characterization

The XRD patterns for all catalysts are shown in Figure 4.1. The Mo_2C synthesized was a mixture of face-center-cubic α-MoC_{1-x} and hexagonal-close-pack β-Mo_2C [8,16]. For Cu/Mo_2C catalysts with low Cu loading (0.1 ML and 0.25 ML), the absence of Cu peaks suggests that the metal domains were small and well dispersed. For 0.5 ML Cu, small Cu peaks were observed, indicating the formation of some small crystalline domains, albeit with dimensions that were too small to be quantified using a peak-broadening (Scherrer) fitting. For Cu loading greater than 0.75 ML, the Cu peaks became identifiable. However, due to the peak overlap between α-MoC_{1-x} and Cu, it is difficult to accurately estimate the Cu crystalline size using peak-broadening fitting. The Cu peaks were also observed in the XRD pattern of 0.5 ML Cu/0.5 ML K/Mo_2C.

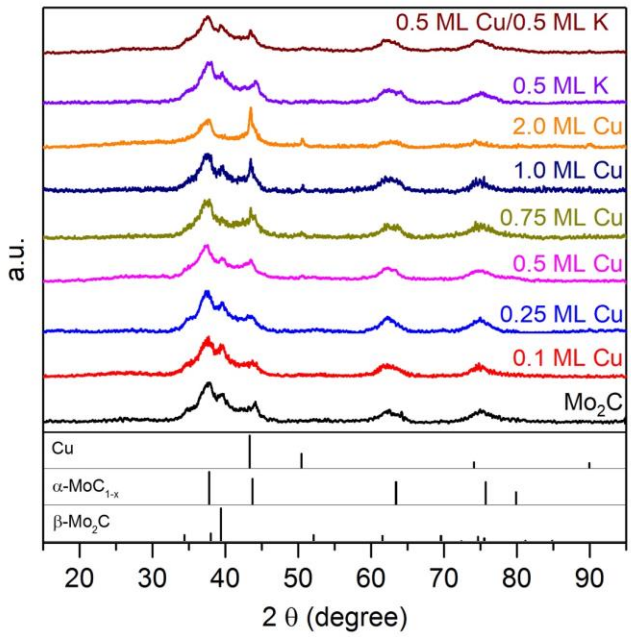

Figure 4.1 Diffraction patterns Mo_2C and Mo_2C-supported metal catalysts. Relevant standards: Cu (JCPDF 00-004-0836), α-MoC_{1-x} (JCPDF 00-015-0457), and β-Mo_2C (JCPDF 00-035-0787).

The surface area, metal content, and chemisorption uptake of each catalyst is provided in Table 4.1. The catalyst surface area declined as the metal loading increased, which suggests admetal pore-blocking. Among all catalysts, the 0.5 ML Cu/0.5 ML K/Mo_2C had the most severe reduction in surface area. The CO and NH_3 uptakes for Cu/Mo_2C catalysts also slightly deceased as Cu loading increased, which implies the adsorption sites could gradually be covered by the deposited Cu. Upon the deposition K onto Mo_2C, the surface acid sites were eliminated, which is consistent with the previous report [17]. Aside from NH_3, the CO desorbed from Mo_2C also decreased significantly after the addition of K. When K adatoms present on Mo_2C, the adsorbed CO was found more likely to undergo dissociation [18], which might affects the amount of CO uptake.

Table 4.1 Surface and physical properties for all catalysts.

Catalysts	Surface Area (m^2/g)	Metal content[a] (wt%)	CO uptake (μmol/g)	CO uptake ($\mu mol/m^2$)	NH_3 Uptake (μmol/g)	NH_3 Uptake ($\mu mol/m^2$)
Mo_2C	110	-	417	3.79	159	1.45
0.1 ML Mo_2C	87	1.1	385	4.42	145	1.67
0.25 ML Cu/Mo_2C	87	2.7	332	3.82	112	1.29
0.50 ML Cu/Mo_2C	82	5.0	242	2.95	104	1.27
0.75 ML Cu/Mo_2C	78	7.6	226	2.90	87	1.11
1.0 ML Cu/Mo_2C	74	9.6	178	2.41	76	1.03
2.0 ML Cu/Mo_2C	74	17.6	166	2.24	64	0.86
0.5 ML K/Mo_2C	87	1.7	13	1.49	21	0.24
0.5 ML Cu/0.5 ML K/Mo_2C	47	5.2 (Cu) 1.7 (K)	12	2.55	18	0.38

[a] Determined by the amount of precursor used.

Based on the report that most of the CO desorbed from Cu at temperatures below 0°C [19], and Mo_2C has a stronger interaction with CO than Cu [20], we speculated that the majority of CO adsorbed on Mo_2C. Overall, characterization results were consistent with the speculation. In CO chemisorption, the amount of CO uptake decreased linearly with the increase of Cu loading when loading is small (≤ 0.5 ML). As the XRD patterns showed that Cu were well dispersed at low loading, these data suggest that the CO adsorption sites on Mo_2C were covered up by Cu. In corresponding CO TPDs, no additional peak was created after Cu deposition, and desorption temperatures of Cu/Mo_2C were similar to Mo_2C in general with some variations (see Figure 4.2).

These results indicate the natures of CO adsorption sites of Cu/Mo_2C were similar to bare Mo_2C and the Mo_2C surface was the major location that the CO chemisorption took place. In a control experiment of CO chemisorption on 0.1 ML Cu/Al_2O_3, no measurable amount of CO uptake was detected.

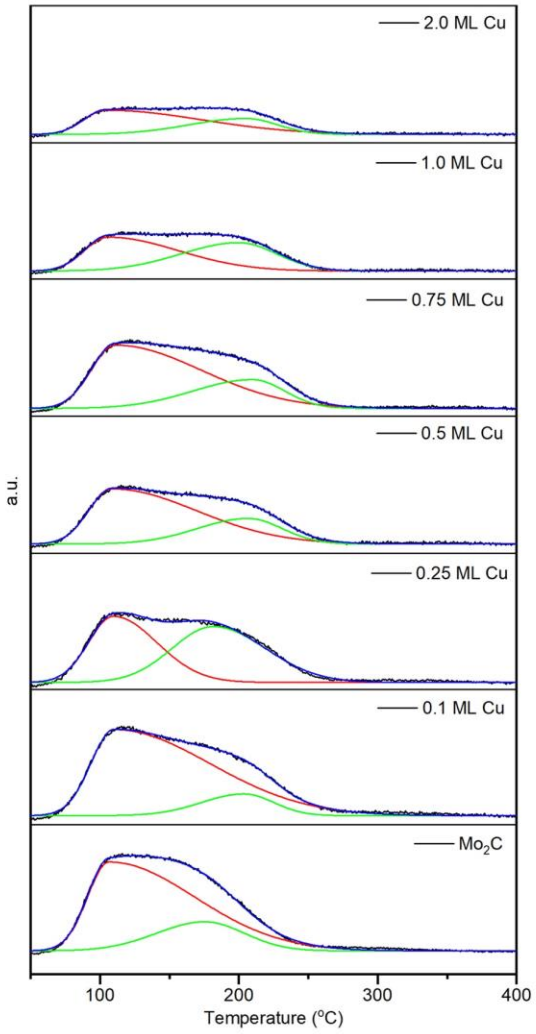

Figure 4.2 CO TPD spectra for Mo2C supported metal catalysts.

With the observations, we tentatively attribute the CO adsorption to the Mo_2C surface exposed (i.e. not covered by Cu); the percentages of Mo_2C surface exposed and covered by Cu could then be estimated, as shown in Table 4.2. The estimation results were consistent with the

observations in XRD patterns, which at low loading the Cu was well dispersed. The conclusion is also consistent with the previous report that Cu nanoparticles tend to form a 2D structure on Mo_2C surface at low loading [21].

Table 4.2 Percentage of Mo_2C surface exposed and Cu dispersion calculated based on the CO uptake results.

Cu loading	0.1 ML	0.25 ML	0.5 ML	0.75 ML	1.0 ML	2.0 ML
Exposed Mo_2C Surface	92.4%	79.7%	58.0%	54.1%	42.8%	39.9%
Mo_2C surface covered by Cu	7.6%	20.3%	42.0%	45.9%	57.2%	60.1%
Estimated Dispersion	76%	81%	84%	61%	57%	30%
Cu loading	0.1 ML	0.25 ML	0.5 ML	0.75 ML	1.0 ML	2.0 ML

4.3.2 Aldehyde Water Shift Activity

Under the reaction condition used in this research, H_2 may be formed by either AWS, steam reforming, or ethanol dehydrogenation [22,23]. As the product distribution was not observed to change with varying flow rate, the dehydration of ethanol, a product of a side reaction, is not a significant source of H_2. Meanwhile, as neither CO nor CO_2 were observed in the product stream, steam reforming was also determined not to be a significant source of H_2. Consequently, we concluded AWS was the major source of H_2, and the H_2 production rate is considered equivalent to the AWS rate. Acetic acid is not a good measurement for the rates of AWS reaction because the side reaction also produces acetic acid, along with ethanol. In general, the total amount of acetic acid produced is comparable to the summation of the amounts of H_2 and ethanol productions. Aside from acetic acid and ethanol, formations of crotonaldehyde were also observed. These products and associated reactions will be discussed in the next section.

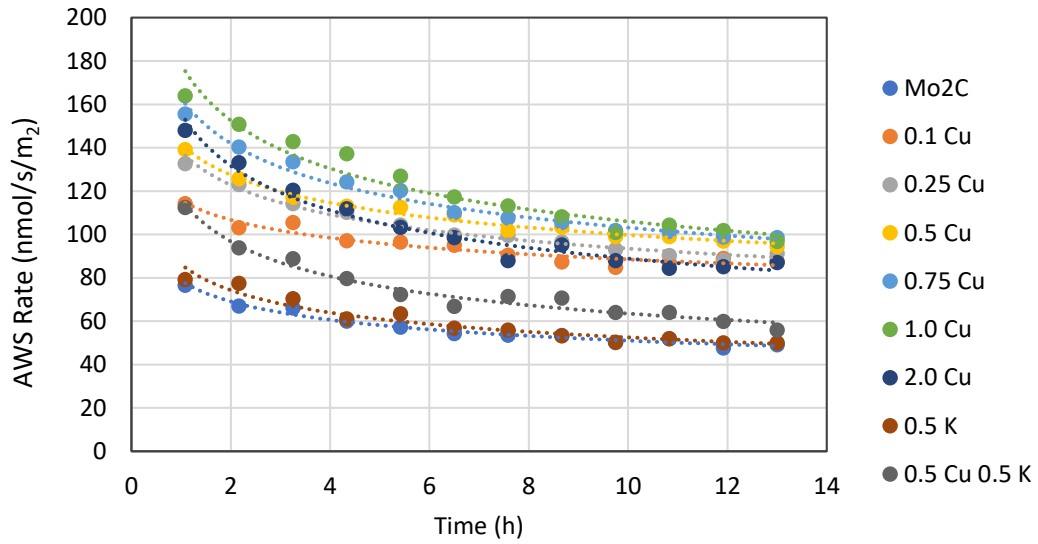

Figure 4.3 Deactivation profiles at 240°C for Mo_2C-based catalysts.

At 240 °C, all catalysts deactivated during the first few hours on stream and reached pseudo-steady states after ~10 h (shown in Figure 4.3), and the degrees of deactivation were similar (~37% ± 8%). To understand the deactivation mechanism, the deactivation profiles were fit to empirical decay models. The reciprocal power model, which typically associated with deactivation by surface fouling or carbon [24,25], fits data for all the materials reasonably well (see Table 4.3).

Table 4.3 Results from nonlinear regression of Mo_2C-based catalysts empirical decay rate laws.

Catalyst	Type	Linear	Exponential	Hyperbolic	Reciprocal Power
	Differential Form	$-da/dt = k_d a$	$-da/dt = k_d a$	$-da/dt = k_d a^2$	$-da/dt = k_d A_0^{1/5} a^m$
	Integral form	$a = 1 - k_d t$	$a = e^{-k_d t}$	$a = 1/1 + k_d t$	$a = A_0 t^{-k_d}$
Mo_2C	k_d (h^{-1})	0.031	0.042	0.052	0.186
	A_o	-	-	-	1.02
	R_{adj2}	0.782	0.874	0.923	0.973
0.1 ML Cu/ Mo_2C	k_d (h^{-1})	0.023	0.026	0.030	0.116
	A_o	-	-	-	1.01
	R_{adj2}	0.743	0.804	0.847	0.917
0.25 ML Cu/ Mo_2C	k_d (h^{-1})	0.030	0.036	0.043	0.166
	A_o	-	-	-	1.04
	R_{adj2}	0.862	0.920	0.950	0.979
0.5 ML Cu/ Mo_2C	k_d (h^{-1})	0.029	0.034	0.041	0.150
	A_o	-	-	-	1.02
	R_{adj2}	0.802	0.876	0.922	0.984
0.75 ML Cu/ Mo_2C	k_d (h^{-1})	0.034	0.042	0.052	0.194
	A_o	-	-	-	1.04
	R_{adj2}	0.847	0.919	0.952	0.979
1.0 ML Cu/ Mo_2C	k_d (h^{-1})	0.036	0.044	0.055	0.258
	A_o	-	-	-	1.03
	R_{adj2}	0.925	0.960	0.960	0.968
2.0 ML Cu/ Mo_2C	k_d (h^{-1})	0.041	0.053	0.068	0.240
	A_o	-	-	-	1.05
	R_{adj2}	0.779	0.885	0.927	0.967
0.5 ML K/ Mo_2C	k_d (h^{-1})	0.034	0.042	0.051	0.207
	A_o	-	-	-	1.07
	R_{adj2}	0.869	0.908	0.916	0.924
	k_d (h^{-1})	0.044	0.060	0.080	0.258

0.5 ML	A_o	-	-	-	1.03
Cu/0.5 ML K/ Mo_2C	R_{adj2}	0.733	0.865	0.921	0.968

The stabilized H_2 production rates at 240°C for all catalysts are provided in Table 4.4. The bare Mo_2C was highly active for AWS, and the rate was almost twofold higher than the rate of Cu-Zn-Al. The activity for AWS of the catalyst was further enhanced upon the deposition of Cu on Mo_2C. For Cu loading from 0.1 ML to 1.0 ML, the AWS rates increased gradually and peaked at 0.75 ML and 1.0 ML, which showed a 100% enhancement. As Cu loading increased to 2.0 ML, the AWS activity declined, while remaining 70% more active than bare Mo_2C. In contrast, the AWS activity of K/Mo_2C catalyst was similar to the Mo_2C; no enhancement was observed with K deposition. Comparing to K/Mo_2C, Cu/K/Mo_2C had a slightly higher activity for AWS, which could be attributed to the presence of Cu. By deconvoluting the AWS activity of the exposed Mo_2C surface from Cu/Mo_2C using CO uptake results, the AWS activity attributed to Cu admetal were estimated using the method described in Method Section 4.2.3.

Table 4.4 AWS 240°C rates, Cu normalized rate, and activation energy

Catalysts	240°C H_2 Rate ($nmol/s/m^2$)	Cu Activity ($mol\ H_2/s/mol_{Cu} \times 10^3$)	Apparent E_a (kCal/mol)
Mo_2C	49.4	---	14
Cu-Zn-Al	28	3.4	23
0.1 ML Cu/CeO_2	14	8.8	19
0.1 ML Cu/Mo_2C	87.8	14.1	15
0.25 ML Cu/Mo_2C	90.2	8.1	14
0.50 ML Cu/Mo_2C	96.4	5.9	15
0.75 ML Cu/Mo_2C	99.5	4.1	16
1.0 ML Cu/Mo_2C	100.9	3.4	15
2.0 ML Cu/Mo_2C	85.5	1.5	14
0.50 ML K/Mo_2C	52.3	---	13
0.5 ML Cu/0.5 ML K/Mo_2C	58.8	---	12

In comparison to Cu supported on CeO_2 and in Cu-Zn-Al, the Cu on Mo_2C (0.1 ML) was 60-300% more active. This demonstrated the importance of the support and implies there may exist synergies between Cu admetal and Mo_2C support. To understand the characteristic of active sites for Cu on Mo_2C, the Cu activities were plotted as a function of Cu loading (see Figure 4.4), and fitted with perimeter and surface active site models using a least squares method. As shown in Figure 4.4, the perimeter active site model well predicted the Cu rates. The R^2 value and root mean square error (RMSE) for the perimeter site model are 0.97 and 0.82, respectively; the R^2 value and RMSE for the surface site model are 0.75 and 2.23, respectively. This suggests the perimeter of Cu particles (i.e. the interface between Cu admetal and Mo_2C support) were the key to high activity. The apparent activation energies (E_a) of Cu/Mo_2C and representative Arrhenius plots were provided in Table 4.4.In general, the E_a of Cu/Mo_2C were similar for all Mo_2C based catalysts. See Arrhenius plots for all catalysts in Figure 4.5.

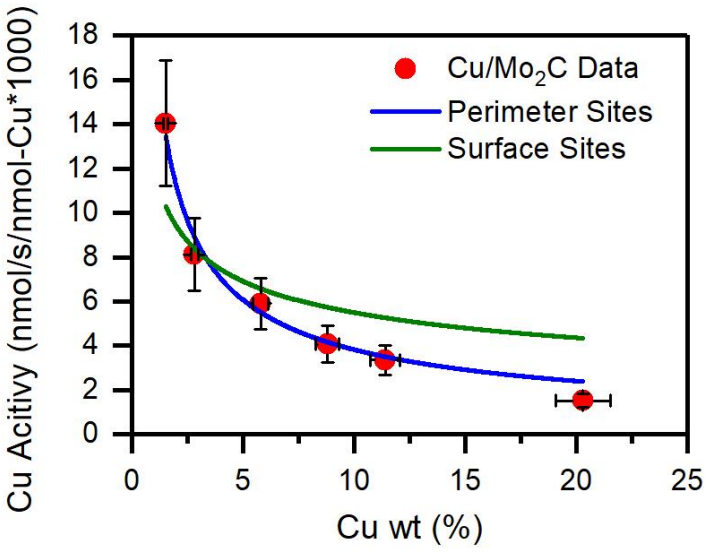

Figure 4.4 AWS rates 240°C for Cu on Mo_2C as a function of Cu loading; predicted rates using the perimeter site and surface site models were included.

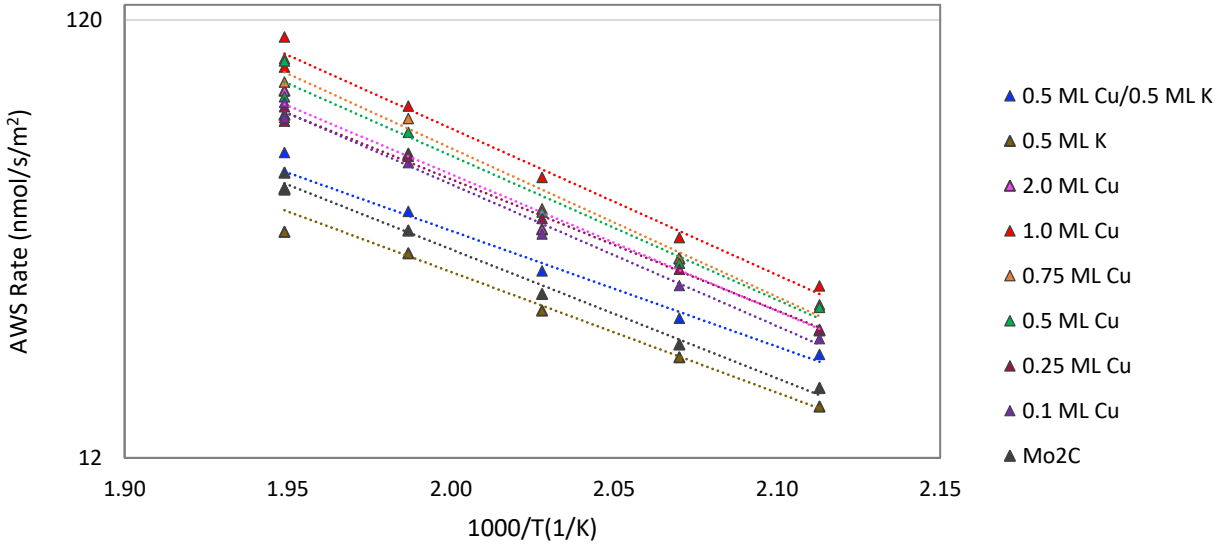

Figure 4.5 Arrhenius plots showing the A WS areal rates for all Mo2C-based catalysts.

As mentioned earlier in this section, fouling was speculated to be the cause of catalyst deactivation, which can often be regenerated [26]. To investigate this possibility, bare Mo_2C, 1.0 ML Cu/Mo_2C, and 2.0 ML Cu/Mo_2C catalysts were evaluated for catalytic regeneration. For

Mo_2C, reaction rates for the fresh and regenerated were nearly identical (53 nmol/s/m^2 and 51 nmol/s/m^2 at 240 °C). CO uptake of the regenerated material (381 μmol/g) was also similar to the fresh Mo_2C catalyst (417 μmol/g). Similar observations were made for the 1.0 ML and 2.0 ML Cu/Mo_2C catalysts (see Table 4.5). Together, these results are consistent with a surface fouling mechanism, rather than irreversible degradation such as sintering and poisoning.

Table 4.5 AWS activity and CO uptake results for selective fresh and regenerated catalysts

Catalysts	**Fresh**		**Regenerated**	
	AWS Rate (nmol/s/m^2)	CO uptake (μmol/g)	AWS Rate (nmol/s/m^2)	CO uptake (μmol/g)
Mo_2C	53	417	51	381
1.0 ML Cu/Mo_2C	104	178	99	182
2.0 ML Cu/Mo_2C	83	166	70	148

4.3.3 Sides Reactions and Selectivity

In addition to acetic acid and H_2, considerable amounts of ethanol and small amounts of crotonaldehyde were produced by all catalysts. The production rates of the two side products along with acetic acid are listed in Table 4.6 and selectivities to the carbon-containing products are shown in Figure 4.6.

Table 4.6 Stabilized production rates of acetic acid, ethanol, and crotonaldehyde at 240 °C.

Catalysts	Acetic Acid Rate (nmol/s/m^2)	Ethanol Rate (nmol/s/m^2)	Crotonaldehyde Rate (nmol/s/m^2)
Mo_2C	95.1	48.3	2.9
0.1 ML Mo_2C	107.9	45.0	1.0
0.25 ML Cu/Mo_2C	108.6	41.3	0.9
0.50 ML Cu/Mo_2C	110.2	42.8	1.5
0.75 ML Cu/Mo_2C	104.0	38.3	1.3
1.0 ML Cu/Mo_2C	121.7	38.9	1.7
2.0 ML Cu/Mo_2C	92.0	31.9	1.0
0.50 ML K/Mo_2C	32.2	9.3	0.9
0.5 ML Cu/0.5 ML K/Mo_2C	35.1	9.8	1.2

As acetaldehyde hydrogenation could potentially be the source of ethanol, H_2 and acetaldehyde were co-fed to the Mo_2C catalyst in a control experiment. In the experiment, very little ethanol was formed, and there was no evidence of H_2 consumption. This suggests that acetaldehyde hydrogenation was not the major source of ethanol. Instead, we believe that the ethanol was produced via the Cannizzaro reaction [27,28]. Note that acetic acid is a common product of AWS and Cannizzaro reaction, so ethanol production was used as the measure of the rate of Cannizzaro reaction. In general, the amount of acetic acid measured (AWS and Cannizzaro) matched summation of the productions of H_2 (AWS) and ethanol (Cannizzaro). Crotonaldehyde is likely a product of aldol condensation [29–32].

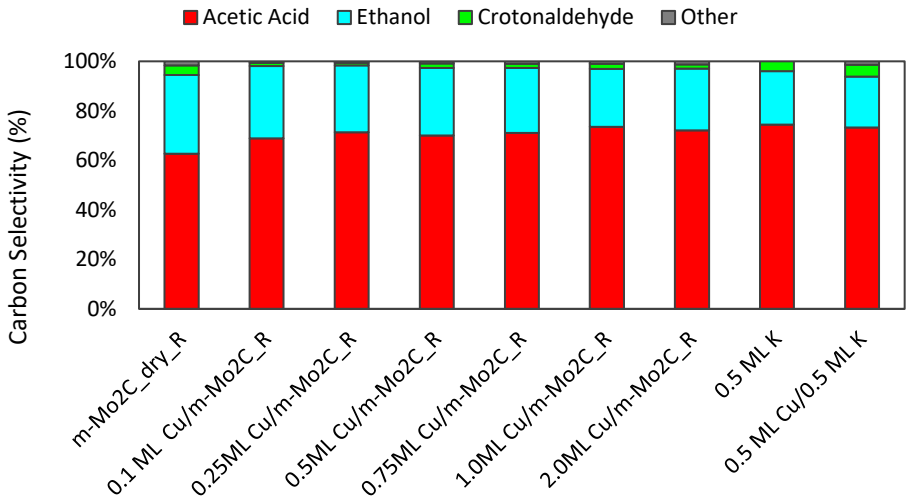

Figure 4.6 Carbon selectivities for catalysts.

As shown in Table 4.6, the ethanol production rates slightly decreased with the increase of Cu loading, and the reaction rates were significantly suppressed upon the deposition of K. Recall that the acid site density had a similar trend of decrease. By plotting the Cannizzaro rates with the acid site density, the rates of Cannizzaro reaction were found to be highly correlated with the surface acid sites density (see Figure 4.7); the TOF is approximately 0.033±0.004 1/s. While CO uptakes also decayed with the addition of Cu and K, however, the Cannizzaro reaction rates and CO site density did not correlate well; the TOF was approximately 0.022±0.019 1/s. While aldol condensation was noted to be a minor side reaction, no correlation between the reaction rates and catalytic properties was observed.

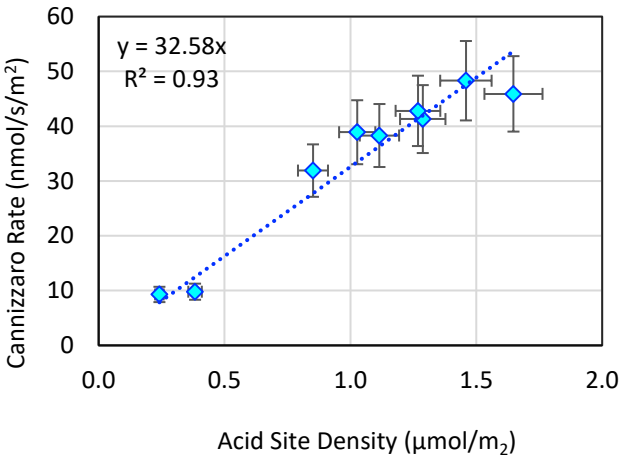

Figure 4.7 Cannizzaro reaction rates versus acid sites density of Mo_2C-based catalysts.

4.3.4 Reaction Pathway Calculations

As discussed earlier, the rates of AWS reaction and Cannizzaro reaction discussed in this research were measured by the produced rates H_2 and ethanol, respectively. As acetic acid is a common product of the AWS reaction and the Cannizzaro reaction, the production rate of acetic acid theoretically should be the sum of the AWS (H_2) and Cannizzaro reaction rates (ethanol). To confirm the proposed reaction pathway, the theoretical rates for each reaction were calculated AWS and Cannizzaro reaction are the only source of H_2, acetic acid, and ethanol. Specifically, if the H_2 rate measured was "x_{exp}" (with theoretical rate x_{Theo}), and the ethanol rate measured was "y_{exp}" (with theoretical rate y_{Theo}), and the acid production rate measured was "z_{exp}" (and theoretical rate z_{Theo}, which $z_{Theo}= x_{Theo} + y_{Theo}$). The x_{Theo}, y_{Theo}, and z_{Theo} was then calculated by using the least squares method, which is the sum of $[(x_{exp}-x_{Theo})/x_{Theo}]^2$, $[(y_{exp}-y_{Theo})/y_{Theo}]^2$, and $[(z_{exp}-z_{Theo})/z_{Theo}]^2$, and solved numerically. The measured and calculated results are provided in Table 4.7. In the table, the theoretical rates are noted as "Calculated" in the errors were then determined. Note that there was approximately 15-20% error in the H_2 and ethanol measurements by GC-TCD and FID, respectively, resulting in a maximum error of 40%.

Table 4.7 The error calculation for the production rates of H_2, ethanol, and acetic acid.

Catalysts	Average Production Rate (nmol/s/m_2)	H_2	Ethanol	Acetic Acid
Mo_2C	Measured	49.5	48.3	95.1
	Calculated	49.1	47.8	96.9
	Error	0.9%	1.8%	0.9%
0.1 ML Cu/Mo_2C	Measured	87.8	45.9	107.9
	Calculated	81.8	44.1	125.9
	Error	7.4%	4.1%	14.3%
0.25 ML Cu/Mo_2C	Measured	89.9	41.3	108.6
	Calculated	84.1	39.9	123.9
	Error	6.9%	3.4%	12.4%
0.5 ML Cu/Mo_2C	Measured	96.7	42.8	110.2
	Calculated	89.3	41.2	130.5
	Error	8.3%	4%	15.6%
0.75 ML Cu/Mo_2C	Measured	99.5	38.3	104.0
	Calculated	90.7	36.8	127.4
	Error	9.7%	4.2%	18.4%
1.0 ML Cu/Mo_2C	Measured	100.9	38.9	121.7
	Calculated	117.1	36.6	153.7
	Error	13.8%	6.4%	20.8%
2.0 ML Cu/Mo_2C	Measured	85.5	31.8	92.0
	Calculated	83.1	28.0	111.1
	Error	2.9%	13.9%	17.2%
0.5 ML K/ Mo_2C	Measured	50.3	9.3	32.2
	Calculated	42.9	9.0	51.8
	Error	16.7%	3.9%	38.0%
	Measured	58.9	9.8	35.1

0.5 ML	Calculated	50.2	9.5	59.7
Cu/0.5 ML K/ Mo_2C	Error	17.4%	3.7%	41.1%

4.4 Discussion

In this Chapter, we describe the physical, chemical and catalytic properties of the Mo_2C and Mo_2C supported Cu and K catalysts for the AWS reaction as well as the side reactions. The catalysts were designed based on the idea of the bifunctional mechanism, in which a catalyst possess distinct sites for H_2O dissociation and acetaldehyde oxidation.

The Mo_2C supported metal catalysts were found to be highly active for AWS. The bare Mo_2C showed an AWS rate twofold higher in comparison Cu-Zn-Al, and the AWS activities of Mo_2C catalysts were further enhanced by 60-100% upon the Cu deposition. At similar Cu loading (0.1 ML), the AWS activity of Cu on Mo_2C (mol/s/mol-Cu) was 2-4 times higher than those reported for Cu on Ce/CeO_2 and Cu-Zn-Al. These results suggest that not only the surface Cu was critical, the Mo_2C support was also playing an essential role in catalyzing AWS reaction. We believe that the high activity of the Mo_2C is due to its unique ability to dissociate H_2O. In research for WGS reaction, the H_2O could easily be dissociated on Mo_2C [33], which the H_2O dissociation was reported to be the rate determining step (RDS) of WGS for many Cu-based catalysts [34,35]. The activation energies for all Mo_2C catalysts were similar, indicating the RDS specific to the Mo_2C support regardless of metal addition. The identification of this RDS is a matter of future research, however, with the similarity between the AWS and WGS, we presume the RDS for AWS to be water splitting or surface reaction, which are the RDS reported for the WGS reaction [4,33,36].

For Mo_2C supported Cu catalysts, we speculated the deposited Cu created additional sites for aldehyde adsorption [37]; the aldehyde adsorbed on admetal could react with the oxygen released from water dissociation on the Mo_2C, which results in higher reaction turnover. Meanwhile, the Cu-Mo_2C interaction slightly altering the catalyst surface properties. Such interaction between Cu and Mo_2C was previously reported to enhance the methanol reforming activity of catalysts [38]. As Cu loading increased, the AWS activity increased and peaked at the loading of 0.75 ML and 1.0 ML, which the estimated Cu coverages were approximately 50%. The observed trend implies that the Cu-Mo_2C interfacial site is critical for catalyzing the AWS reaction; when loading increased to 2.0 ML, less the Cu atoms are in contact with the Mo_2C surface [39,40]. To further understand the nature of the active sites, the AWS activities attributed to Cu admetal and Mo_2C support were isolated by mathematical deconvolution. As stated previously, the majority of CO appeared to adsorb on Mo_2C and exposed Mo_2C surface was estimated using the CO uptake results. After deconvoluting the AWS activity of Cu admetal and Mo_2C support, the Cu activity was found to be well predicted by the perimeter active site model. This suggests that majority of the active sites for the AWS reaction on Cu particle located at the particle perimeters (i.e. the interface between the Cu admetal and the Mo_2C support). These results further support our previous speculation that the Cu-Mo interfacial site played a key role in catalyzing the AWS reaction, which was also consistent with the bifunctional mechanism. A schematic of reaction mechanism that is consistent with our results and what is known about Mo_2C and Cu surfaces is shown in Figure 4.8. We believe two different types of sites were involved, and intimacy between these sites would lead to high AWS rates. This mechanism resembles reports for the WGS reaction and steam reforming for Mo_2C-based catalysts [1,2,4,5,38].

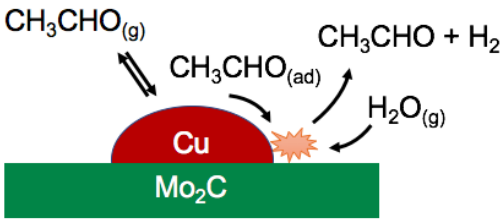

Figure 4.8 Schematic of the reaction mechanism on Cu/Mo_2C catalyst.

Aside from evaluations activity for AWS, examinations of the deactivation also yielded important insights regarding the catalysts. For all catalysts investigated, the results of the regression analysis indicate that deactivations were likely consequences of surface fouling. For a methanol steam reforming (MSR) over Mo_2C, Lausche et al. reported that C=O and C-O species accumulated on the surface perhaps due to carbonate or formate formation, basing on characterization using x-ray photoelectron spectroscopy [25]. Schaidle et al. also proposed that carbonate and formate formation caused the deactivation of Mo_2C during WGS reaction [41]. Similarly, we believe the formation of carbonate and acetate may cause the surface fouling and could explain the deactivation of Mo_2C during AWS. The successful regeneration of Mo_2C-based catalyst supported the speculation that the deactivation was due to surface fouling, as poisoning and sintering mechanisms are considered not reversible [24]. With the high activity and regenerability, Mo_2C supported Cu catalyst could be an ideal catalyst for industrial AWS application.

Beside the acetic acid, all the catalysts produced ethanol as the major side product via Cannizzaro reaction, and the Cannizzaro reaction rates were found to be a strong function of acid site densities of the catalysts. This correlation implies that acid sites could be the active site for the Cannizzaro reaction and allowed us to deduct the reaction mechanism. Siaj et al. reported that aldehyde could adsorb on the Mo site via the O lone pair [42], and Bej et al. contributed the acid

character of Mo_2C to the Mo sites due to electron deficiency [11]. Consequently, it is likely that the Mo sites were the location where aldehyde adsorptions take place. Given this and the report that H_2O is most likely to be activated on the C sites [33], which provide the activated hydroxyl, a mechanism of the Cannizzaro reaction consistent with the results was speculated. A schematic of speculated reaction mechanism is shown in Figure 4.9.

$H_2O + 2^* \rightarrow H^* + OH^*$

$CH_3CHO + OH^* + ^* \rightarrow CH_3CHOOH^{**}$

$CH_3CHOOH^{**} + CH_3CHO^* \rightarrow CH_3COOH\ ^* + CH_3CH_2O^*$

$CH_3CH_2O^* + H^* \rightarrow CH_3CH_2OH^*$

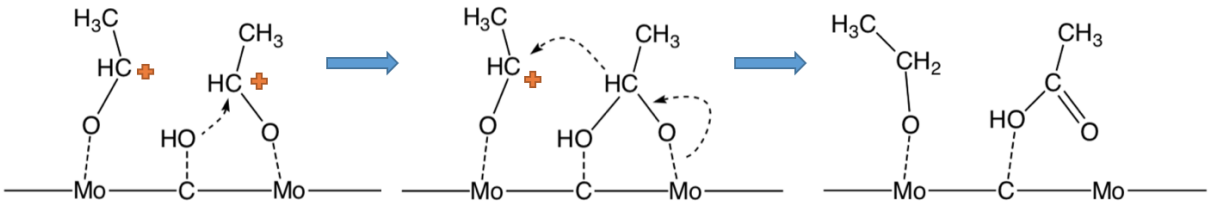

Figure 4.9 Schematic of the speculated Cannizzaro reaction mechanism on Mo_2C-based catalysts.

In the mechanism study for the Cannizzaro reaction on MgO, X. Peng and M. Barteau proposed a base-acid coupling mechanism, which the oxygen in the aldehyde group interact with the weak acid site (Mg^{2+} ion), and carbonyl carbon of the aldehyde attached to the based site (O^{2-} ion) [43]. While no oxygen is available from the Mo_2C lattice, the hydroxyl dissociated from H_2O could serve the role of the O^{2-} ion in MgO when catalyzing the Cannizzaro reaction, which is similar to the report of hydroxyl assisted Cannizzaro reaction on Ag cluster [44].

4.5 Conclusion

In this chapter, we examined the catalytic properties and evaluated the reactivities of Mo_2C supported Cu and K catalysts for the AWS reaction. The characteristics of the active sites for AWS as well as the side reactions were also investigated. For Mo_2C-based catalysts, the bare Mo_2C outperformed the metal oxide supported Cu catalysts with a 2-fold or higher areal rates. For Cu loading of 0.1 ML, the Cu-activity on Mo_2C was ~78% and ~320% more active than those for Cu supported on CeO_2 and Cu-Zn-Al, respectively. Given that Mo_2C is known for its ability to dissociate water, these results reemphasize the importance of the support, and imply there may exist synergies between Cu admetal and Mo_2C support.

When Cu loading was increased from 0.1 to 2.0 ML, the AWS activity increased and peaked at 1.0 ML Cu, which the areal rate was 2-fold compared to that of the bare Mo_2C. The AWS rates of Cu predicted by the perimeter model agreed well with experimental rate results. This suggests that the Cu-Mo_2C interfacial site is critical for catalyzing the AWS reaction. These results are consistent with the bifunctional mechanism, in which the Mo_2C support could catalyze H_2O dissociation easily and the supported Cu could facilitate aldehyde oxidation using oxygen released from H_2O. With the observation that apparent activation energies were found to be a function of Cu loading, it is likely that the RDS took place on the Mo_2C support. Given the similarity between the AWS and the WGS reaction, we speculated the RDS to be water dissociation or surface reaction. Via the investigation of deactivation and regeneration experiments, it was shown that the decay of AWS activity may due to surface fouling, and the catalysts' activities can be successfully retrieved under proper reactivation process. With the high activity and regenerability, Mo_2C could be an excellent AWS catalyst for industrial application.

For all of the Mo_2C-based catalysts, the selectivity to acid was 63-74% to acetic acid, which is similar to Cu-Zn-Al, the benchmark catalysts. On the other hand, ethanol was produced as the major side product via Cannizzaro reaction, and the selectivity to ethanol was 32-24%. The Cannizzaro reaction rates were found to be well correlated with the acid site density of catalysts. This indicates that the Cannizzaro reaction could be catalyzed by the acid sites. Specifically, it is speculated the aldehyde adsorbed on the acid site interacts with the hydroxyl dissociated from water and forms a surface acetate. The acetate then reacts with another aldehyde adsorbed on the adjacent acid site to produce ethanol and acetic acid. These findings will guide the development of productive catalysts for the AWS reaction. To gain further insight into the reaction mechanism, microkinetic modeling was examined in the next chapter. Additionally, the reactivities of different phases of Mo_2C were investigated.

4.6 References

[1] N. M. Schweitzer, J. A. Schaidle, O. K. Ezekoye, X. Pan, S. Linic, L. T. Thompson, J. Am. Chem. Soc. 133 (2011) 2378–2381.
[2] K. D. Sabnis, Y. Cui, M. C. Akatay, M. Shekhar, W. S. Lee, J. T. Miller, W. N. Delgass, F. H. Ribeiro, J. Catal. 331 (2015) 162–171.
[3] K. D. Sabnis, M. C. Akatay, Y. Cui, F. G. Sollberger, E. A. Stach, J. T. Miller, W. N. Delgass, F. H. Ribeiro, J. Catal. 330 (2015) 442–451.
[4] S. Yao, X. Zhang, W. Zhou, R. Gao, W. Xu, Y. Ye, L. Lin, X. Wen, B. Chen, E. Crumlin, J. Guo, Z. Zuo, W. Li, J. Xie, L. Lu, C.J. Kiely, L. Gu, C. Shi, J. A. Rodriguez, D. Ma, Science. 4321 (2017) 1–10.
[5] L. Lin, W. Zhou, R. Gao, S. Yao, X. Zhang, W. Xu, S. Zheng, Z. Jiang, Q. Yu, Y.-W. Li, C. Shi, X.-D. Wen, D. Ma, Nature. 544 (2017) 80–83.
[6] M. Cargnello, V. V. T. Doan-nguyen, T.R. Gordon, R.E. Diaz, E.A. Stach, R.J. Gorte, P. Fornasiero, C.B. Murray, Science 341 (2013) 771–774.
[7] J. Raskó, J. Kiss, Appl. Catal., A. 287 (2005) 252–260.
[8] Y. Chen, S. Choi, L. T. Thompson, J. Catal. 343 (2016) 147–156.
[9] Y. Chen, S. Choi, L. T. Thompson, ACS Catal. 5 (2015) 1717–1725.
[10] J. A. Schaidle, N. M. Schweitzer, O. T. Ajenifujah, L. T. Thompson, J. Catal. 289 (2012) 210–217.
[11] S. K. Bej, C. A. Bennett, L. T. Thompson, Appl. Catal. A 250 (2003) 197–208.
[12] C. Ratnasamy, J. P. Wagner, Catal. Rev. 51 (2009) 325–440.
[13] L. M. Orozco, M. Renz, A. Corma, ChemSusChem. 9 (2016) 2430–2442.
[14] L. M. Orozco, M. Renz, A. Corma, Green Chem. 19 (2017) 1555–1569.

[15] N. Xiang, P. Xu, N. Ran, T. Ye, RSC Adv. 7 (2017) 38586–38593.
[16] B. M. Wyvratt, J. R. Gaudet, L. T. Thompson, J. Catal. 330 (2015) 280–287.
[17] X. Liu, S.J. Ardakani, K.J. Smith, Catal. Commun. 12 (2011) 454–458.
[18] L. Bugyi, F. Solymosi, J. Phys. Chem. B. 105 (2001) 4337–4342.
[19] A. Verdaguer-Casadevall, C. W. Li, T. P. Johansson, S. B. Scott, J. T. McKeown, M. Kumar, I. E. L. Stephens, M. W. Kanan, I. Chorkendorff, J. Am. Chem. Soc. 137 (2015) 9808–9811.
[20] S. Posada-Pérez, P.J. Ramírez, R.A. Gutiérrez, D.J. Stacchiola, F. Viñes, P. Liu, F. Illas, J. A. Rodriguez, Catal. Sci. Technol. 6 (2016) 6766–6777.
[21] S. Posada-Pérez, F. Viñes, J. A. Rodríguez, F. Illas, J. Chem. Phys. 143 (2015) 114704
[22] K. Weissermel, A. Hans-Jürgen, Industrial Organic Chemistry, WILEY-VCH Verlag GrnbH & Co. KGaA, Weinheim, 2003
[23] M. E. Sad, M. Neurock, E. Iglesia, J. Am. Chem. Soc. 133 (2011) 20384–20398.
[24] H.S. Fogler, Elements of Chemical Reaction Engineering, forth ed., Pearson Education, Inc. Upper Saddle River, New Jersey, 2006
[25] A. C. Lausche, J. A. Schaidle, L. T. Thompson, Appl. Catal., A. 401 (2011) 29–36.
[26] M. D. Argyle, C. H. Bartholomew, Catalysts 5 (2015) 145–269.
[27] T. P. Brewster, W. C. Ou, J. C. Tran, K. I. Goldberg, S. K. Hanson, T. R. Cundari, D. M. Heinekey, ACS Catal. 4 (2014) 3034–3038.
[28] M. Watanabe, M. Osada, H. Inomata, K. Arai, A. Kruse, Appl. Catal., A. 245 (2003) 333–341.
[29] J.E. Rekoske, M. A. Barteau, Langmuir. 15 (1999) 2061–2070.
[30] M. J. Climent, A. Corma, V. Fornés, R. Guil-Lopez, S. Iborra, Adv. Synth. Catal. 344 (2002) 1090–1096.
[31] H. Idriss, K.S. Kim, M. A. Barteau, J. Catal. 139 (1993) 119–133.
[32] H. Idriss, C. Diagne, J.P. Hindermann, A. Kiennemann, M.A. Barteau, J. Catal. 155 (1995) 219–237.
[33] P. Liu, J. A. Rodriguez, Phys. Chem. B. 110 (2006) 19418–19425.
[34] M. J. L. Ginés, N. Amadeo, M. Laborde, C. R. Apesteguía, Appl. Catal., A. 131 (1995) 283–296.
[35] A. A. Gokhale, J. a. Dumesic, M. Mavrikakis, J. Am. Chem. Soc. 130 (2008) 1402–1414.
[36] H. Tominaga, M. Nagai, J. Phys. Chem. B. 109 (2005) 20415–20423.
[37] M. Bowker, R. J. Madix, Appl. Surf. Sci. 8 (1981) 299–317.
[38] Y. Ma, G. Guan, X. Hao, Z. Zuo, W. Huang, P. Phanthong, K. Kusakabe, A. Abudula, RSC Adv. 4 (2014) 44175–44184.
[39] J. A. Rodriguez, D. C. Grinter, Z. Liu, R. M. Palomino, S. D. Senanayake, Chem. Soc. Rev. 46 (2017) 1824–1841.
[40] J. A. Rodriguez, P. Liu, J. Hrbek, J. Evans, M. Pérez, Angew. Chem. 119 (2007) 1351–1354.
[41] J. A. Schaidle, A. C. Lausche, L. T. Thompson, J. Catal. 272 (2010) 235–245.
[42] M. Siaj, I. Temprano, N. Dubuc, P. H. Mcbreen, J. Organomet. Chem.691 (2006) 5497–5504.
[43] X. D. Peng, M. A. Barteau, Langmuir. 5 (1989) 1051–1056.
[44] Wang, X., Catalysis Today (2018), https://doi.org/10.1016/j.cattod.2018.06.021

Chapter 5

Reaction Kinetics of α-MoC_{1-x} and β-Mo_2C Supported Metal Catalysts

5.1 Introduction

In previous chapters, the catalytic properties and reactivities of metal oxide and Mo_2C supported metal catalysts were evaluated. Among all supported metal catalysts examined in this dissertation, Mo_2C is the most active support. Also, the deposition of Cu on Mo_2C effectively enhanced the aldehyde water shift (AWS) activity of catalysts. When increasing Cu loading on Mo_2C from 0.1 ML to 2.0 ML, the AWS activity peaked at 1.0 ML and the areal AWS rate was enhanced by 100% compared to the bare Mo_2C. The active site of the Cu admetal was found to be located on the periphery of the Cu particles. These results and the known chemistry of Mo_2C and Cu are consistent with the presence of a bifunctional mechanism. In this bifunctional mechanism, water is dissociated on Mo_2C, and activated oxygen or hydroxyl released from water reacts with the acetaldehyde adsorbed on the Cu domain. As described in previous chapters, the Mo_2C investigated was a mixture of face-center-cubic (fcc) α-MoC_{1-x} and hexagonal-close-packed (hcp) β-Mo_2C.

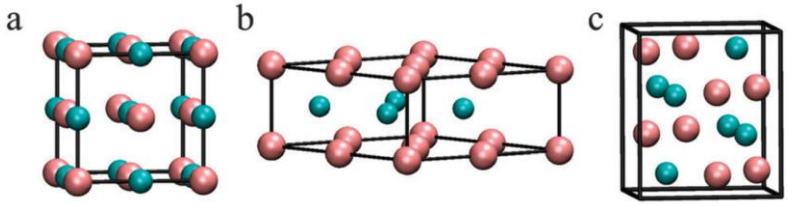

Figure 5.1 Bulk crystallographic structures of (a) face-center-cubic, (b) the hexagonal-close-packed (hcp), and (c) orthorhombic carbide. Turquoise and magenta spheres denote C and Mo atoms, respectively. Adopted from [1].

While the structures of molybdenum carbide are well known [1–3] (shown in Figure 5.1), the designations for each carbide structures have varied considerably in the field (see Table 5.1). For instance, all the orthorhombic, hcp, and fcc structure of carbide have been denoted as the α-phase carbide. Another example, some reports in the literature denoted the fcc α-MoC_{1-x} as fcc α-MoC [4,5]. Due to lack of consistency in the terminology, it is critical to first define the designations that I use to avoid confusion in later discussions. In this dissertation, the fcc and hcp structures of the carbide are designate as α-MoC_{1-x} and β-Mo_2C, respectively. This designation is consistent with previous publications from the Thompson group [6,7] and is commonly seen in the literature.

Table 5.1 Examples of different designations of different structure of the molybdenum carbide in the literature.

Structure / **Phase Designation**	**Orthorhombic**	**Hexagonal Close Packed (hcp)**	**Face Center Cubic (fcc)**
α	[8]	[1]	[3–6,9,10]
β	[1,11,12]	[3–6,8–10]	---
δ	---	---	[1,12]

Previously, research has shown that catalytic properties of molybdenum carbide and their supported metal catalysts are structure dependent. Politi et al. pointed out that the stabilities of the catalysts are structure dependent, following the order of orthorhombic structure > hcp structure > fcc structure; this difference is attributed to factors including Bader charges, d-band center, and cohesive energies [1]. Some reports also indicated that the structures of the carbide are critical to reactivity for numerous reactions, including CO hydrogenation, ammonia synthesis, water gas shift (WGS) reaction, and steam reforming of alcohol [3–5,9,13]. In particular, for reactions that use water as an oxidant and parallel AWS, such as WGS and steam reforming, the reactivity of

molybdenum carbide supported metal catalysts was highly structure-dependent. For WGS reaction, S. Yao et al. reported that the 2 wt% Au/α-MoC showed a mass specific activity that was over 13-folds of that for 2 wt% Au/β-Mo_2C at 200 °C [5]. For aqueous-phase reforming of methanol, L. Lin et al. reported a the mass specific activity of 2 wt% Pt/α-MoC at 190 °C were almost 26-folds of that for 2 wt% Pt/β-Mo_2C [4]. In both papers, the authors attribute the higher activity observed in M/α-MoC to the stronger interaction between the admetal (Pt and Au) and the α-MoC support.

Based on these findings, we could also expect the phase-pure α-MoC_{1-x} and β-Mo_2C to result in different AWS activities. To further explore the use of molybdenum carbide as a catalyst for the AWS reaction, the research described in this chapter evaluated pure phase α-MoC_{1-x} and β-Mo_2C supported Cu catalysts to access the effect of carbide structures on the catalytic properties and reaction kinetics. The phenomenological-based kinetic models examined included Redox, Eley-Rideal, and Langmuir-Hinshelwood type of mechanisms. As we proposed that distinct sites for water dissociation and aldehyde oxidation exist on the Mo_2C-based catalysts, the AWS reaction is speculated to proceed via the Langmuir-Hinshelwood with two types of site. The targeted nominal loading of Cu for both α-MoC_{1-x} and β-Mo_2C was 1.0 ML, which was found to be the optimal loading for the mixed-phase Mo_2C in Chapter 4.

The primary objectives of the experiments described in this chapter are to: (1) evaluate the effect of molybdenum carbide structures on the reactivity for AWS reaction and (2) investigate kinetic modeling to gain more insights into the reaction kinetics and the reaction mechanism.

5.2 Experimental Methods

5.2.1 Catalyst Synthesis

The pure phase α-MoC_{1-x} (fcc) and the β-Mo_2C (hcp) were synthesized via the temperature-programmed reaction method, and the metal was deposited onto the carbide surface by either wet

impregnation or incipient wetness impregnation as previously described [14,15]. In general, the preparation methods were similar to the techniques described earlier in Chapter 2 and Chapter 3, with variations in the temperature programs and the reaction gases used depending on the targeted phase of the carbide.

For α-MoC_{1-x}, the preparation involves the nitridation of ammonium paramolybdate precursor (AM; $(NH_4)_6Mo_7O_{24}$•4 (H_2O), Alfa Aesar) as the first step, followed by carburization of the materials. Approximately 1.3 g of AM, with a particle size range from 125 to 250 μm, was loaded into the quartz reactor, supported by quartz wool, and heated in anhydrous NH_3 (400 mL/min, Cryogenic Gases) using a temperature program. The precursor was first heated to 350 °C (T_1) at a ramp rate of 10 °C /min (β_1) and then to 450 °C (T_2) at a ramp rate of 0.66 °C /min (β_2). The sample was then heated to 700 °C (T_3) at a ramp rate of 1.66 °C /min (β_3) and was held at 700 °C for 2 h (t_{soak}) to form γ-Mo_2N. Upon the completion of soaking, the reactor removed from furnace and quenched to room temperature (< 30 °C). After the reactant temperature dropped to room temperature, the reaction gas was switched from anhydrous NH_3 to 15% CH_4 in H_2 (250 mL/min, Cryogenic Gases) for carburization. In the 15% CH_4/H_2 mixture gas, the γ-Mo_2N material was first heated to 200 °C (ramp rate 10.3 °C/min), and to 590 °C (ramp rate 1.0 °C/min), and then held for 2 h at 590 °C. After soaking, the as-prepared material was quenched to room temperature.

For β-Mo_2C, the material was synthesized directly via carburization of AM. Approximately, 1.3 g AM precursor was first loaded into reactor, similar to the procedure described for α-MoC_{1-x}. In a 15% CH_4/H_2 mixture gas (250 mL/min, Cryogenic Gases), the AM was first heated to 300 °C (ramp rate 5.0 °C/min), and to 700 °C (ramp rate 1.0 °C/min), and then held at 700 °C for 2 h [4]. Upon the completion of soaking, the material was removed from the furnace and quenched to room temperature. Synthesis protocols for the two carbide phases were summarized in Table 5.2.

Table 5.2. Synthesis temperature program protocols for α-MoC_{1-x} and β-Mo_2C [4,16].

Materials	Precursor Weight (g)	Reaction gas	Flow rate (mL/min)	T_1 (°C)	β_1 (°C /min)	T_2 (°C)	β_2 (°C /min)	T_3 (°C)	β_3 (°C /min)	t_{soak} (min)
α-MoC_{1-x}	1.3	NH_3	400	350	10.00	450	0.66	700	1.66	120
		15% CH_4/H_2	250	200	10.30	590	1.00	-	-	120
β-Mo_2C	1.3	15% CH_4/H_2	250	300	5.00	700	1.00	-	-	120

After the final quenching, when the reactor had cooled to below 30 °C, the material was treated in one of the three ways, depending on the targeted products. (1) For bare carbide, the material was passivated in 1% O_2/He (20 mL/min, Cryogenic Gases) at room temperature for ~7 hours. (2) For Cu deposited onto α-MoC_{1-x} and β-Mo_2C via wet impregnation using the procedure described in Chapter 3, the material was passivated after impregnation. (3) For Cu deposited onto α-MoC_{1-x} and β-Mo_2C via incipient wetness impregnation using the procedure described in Chapter 4, the material was reduced in H_2 at 450 °C and then passivated. The as-prepared catalysts were designated as [Metal]/α-MoC_{1-x} and [Metal]/β-Mo_2C.

5.2.2 Material Characterizations

5.2.2.1 X-ray Diffraction

The bulk crystal structures of the catalyst were determined by x-ray diffraction using a Rigaku Miniflex diffractometer equipped with a Cu Kα (λ = 0.15404 nm) radiation source and a Ni filter. Detailed experiment procedures are previously described in Chapter 2.

5.2.2.2 N_2 Physisorption Analysis

The surface area of all catalysts was obtained using the N_2 physisorption isotherm and the Brunauer-Emmett-Teller (BET) theory, using a Micromeritics 2020 instrument. Approximately

100 mg of sample was loaded into a BET tube, degassed at 350 °C for 4 hours prior to performing the analysis. Detailed experimental procedures are described in Chapter 2.

5.2.2.3 Elemental Analysis

The compositions of the molybdenum carbide catalysts were determined via elemental analysis performed with Inductively Coupled Plasma-Optical Emission Spectroscopy (ICP-OES) using a Varian 710-ES spectrometer. Catalysts were first dissolved in 3 mL of aqua regia (0.75 mL of hydrochloric acid and 2.25 mL of nitric acid), the as-prepared solution was then diluted, and the composition was analyzed by comparing the wavelength intensities of the elements of interest with the intensities of known concentration standard solutions. Detailed experiment procedures are described in Chapter 2.

5.2.2.4 CO Chemisorption

The CO chemisorption experiment was carried out to probe the surface acid characters using a Micromeritics ASAP 2920 instrument [17]. In a CO chemisorption experiment, the catalyst was first pretreated with 15% CH_4/H_2 (Cryogenic Gases) at 590 °C for 4 h to remove the passivation layer; this process was identical to the treatment procedures prior to the reactivity evaluation of the catalyst. Following the pretreatment, the material was degassed in He (Cryogenic Gases) at 600 °C for 0.5 h and cooled to 40 °C. The catalyst was then dosed with pulses of 5% CO/He (Cryogenic Gases); where exposure was repeated until surface saturation, at which point the active site densities were determined.

5.2.2.5 NH_3 Chemisorption

The NH_3 chemisorption technique was applied to determine the surface acid character using a Micromeritics ASAP 2920 instrument [18]. The catalysts were pretreated, degassed, and cooled to 40 °C as described in the active sites density measurement procedures before exposure

to NH_3. The sample was then saturated with anhydrous NH_3 (Cryogenic Gases) for 1 hour. The physisorbed/excess amount of NH_3 was removed by purging the sample in flowing He for 30 min. The sample temperature was then heated from 40 °C to 800 °C at a ramp rate of 10 °C/min. The desorbed gases were monitored using a ThermoStar 300 mass spectrometry, which continuously sampled the post reactor stream on the ASAP 2920.

5.2.2.6 Point-of-Zero Charge Measurement

The point-of-zero charge (PZC) of materials were determined using the experiment procedures previously described by Park et al., Schaidle et al., and Wyvratt et al. [7,14,19]. Approximately 20 mL of deaerated water was prepared as the starting solution and was continuously bubbled with inert gas. The volume of deaerated water was chosen based on the desired surface loading of ~500 m^2/L, similar to the value reported by Wyvratt et al [7]. The pH of the starting solution was adjusted with concentrated hydrochloric acid (HCl) or ammonium hydroxide (NH_4OH) to meet the target starting pH value. The pH values of the solution were measured and recorded, using a Mettler Toledo sevenexcellence multiparameter with a Fisher Scientific accumet pH electrodes.

Appropriate amounts of native α-MoC_{1-x} or β-Mo_2C were transferred from the inert atmosphere glovebox (place of storage) and added to the starting solution. Note that the solution was continuously bubbled with an inert gas at all time with special precautions adopted to prevent exposure to air during transfer. The sample was allowed to interact with the solution for 12 hours to ensure the stabilization of the pH value. After the pH value was stabilized, the final pH was determined and recorded. By plotting the final pH value as a function of the initial pH value, the PZC of the catalyst was determined. An example of PZC determination for the mixed phase Mo_2C is shown in Figure 5.2.The flat regions in the plot corresponded to the PZC of the materials, which

was pH ~5, pH ~3, and pH ~3 for unpassivated Mo_2C (Mo_2C), passivated Mo_2C (p-Mo_2C), and MoO_2 materials, respectively [7].

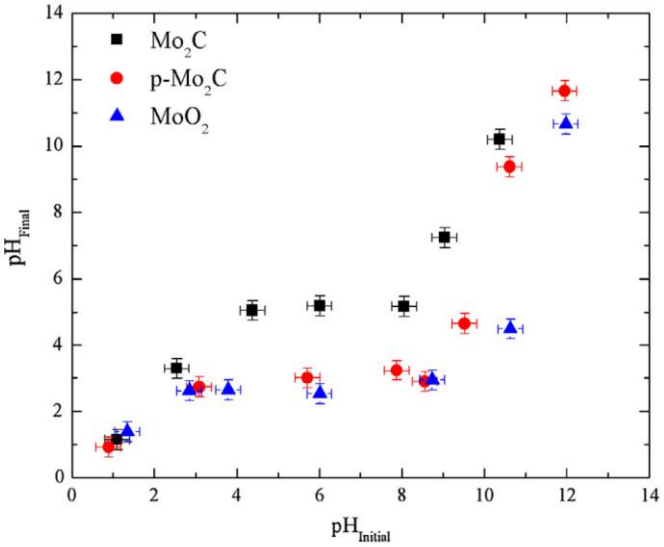

Figure 5.2 Point of zero charge determination for the unpassivated Mo_2C, passivated Mo_2C, and MoO_2 materials. Adopted from [7].

5.2.3 Reaction Rate and Selectivity Measurement

5.2.3.1 Reactivity Evaluation and Arrhenius Plot

Approximately 15 to 25 mg of α-MoC_{1-x}- and β-Mo_2C- based catalysts was used in each experiment during performance evaluation. The catalysts were loaded into a U-shape quartz reactor, supported by quartz wool, and diluted with low surface area SiO_2 (Alfa Aesar; surface area of ~2 m^2/g) to maintain the same bed height for all experiments. Prior to performance evaluation, all catalysts were pretreated with 15% CH_4/H_2 (100 mL/min, Cryogenic Gases) at 590 °C (reached at a ramp rate of 9.4 °C/min) for 4 hours to remove the passivation layer. After the pretreatment, the reactor was cooled to 240 °C. Once reaching 240 °C, the gas stream flowed through the reactor was switched from 15% CH_4/H_2 to the reaction gas mixture, with feed composition consisting of 9% acetaldehyde, 15% water, and 76% N_2 at approximately 60 mL/min (wet basis). The reaction was first held at 240 °C for 10 hours to reach steady state after

deactivation, and followed one of the two ways, depending on the purpose of the experiments: (1) To acquiring carbon balance and stable rate, the reaction was held at 240 °C for another 3 hours to collect the reaction rates data in the pseudo-steady-state regime. Liquid products produced in the pseudo-steady-state was collected with a separate round flask purged with N_2 prior to installation. (2) To acquire the Arrhenius plot and apparent activation energies, the reaction temperature was varied following the order of 200 °C, 230 °C, 210 °C, 220 °C, and back to 240 °C. At each temperature, the reaction was held for 2 hours before returning to 240 °C. After returning to 240 °C, the reaction was held for 3 hours before the termination of experiment. The liquid products produced during deactivation (240 °C) and final pseudo-steady-state regime (240 °C) were collected and analyzed separately.

5.2.3.2 Kinetic Experiments

For all kinetic experiments, the reaction temperature was held at 240 °C. Approximately 15 to 25 mg of catalyst was loaded into the reactor, pretreated, and deactivated on stream for 17 hours under the standard reaction feed composition, which consisted of approximately 0.09 atm acetaldehyde, 0.15 atm water, and 0.76 atm N_2. The standard feed composition is noted as A1W1. The A and W stand for acetaldehyde and water, respectively, and the number indicate the ratio of employed partial pressure to the standard partial pressure. Afterwards, the composition of the feed was varied following a sequence illustrated in Figure 5.3, while maintaining ambient pressure and a constant total flow of approximately 60 mL/min (wet basis). Note that only the partial pressure of one reactant was adjusted (e.g. acetaldehyde) in each set of experiment; the partial pressure of the other reactant remains constant (e.g. water).

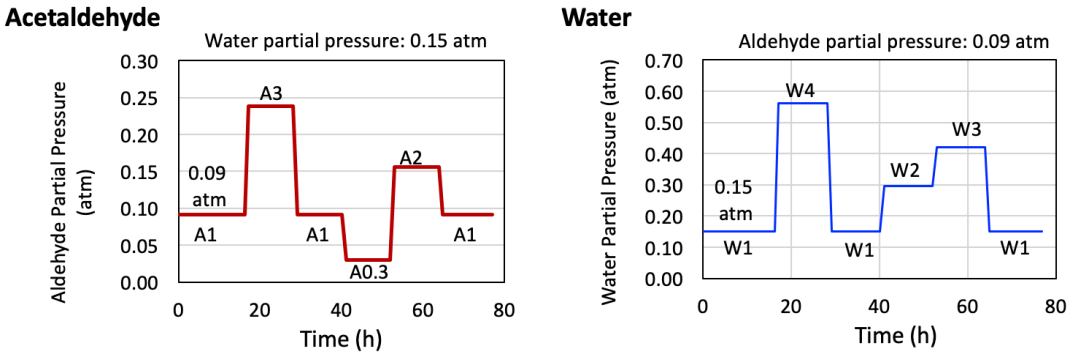

Figure 5.3 The order of partial pressure variations of acetaldehyde and water.

For experiments varying acetaldehyde partial pressure, the partial pressure was varied following in the order of 0.26 atm (A3), 0.09 atm (A1), 0.03 atm (A03), 0.17 atm (A2), and 0.09 atm (A1). Note that the partial pressure of water remained constant. For experiments varying the water partial pressure, the partial pressure was varied following in the order of 0.56 atm (W4), 0.15 atm (W1), 0.30 atm (W2), 0.43 atm (W3), and 0.15 atm (W1). Again, the partial pressure of acetaldehyde remained constant. At each partial pressure, the reaction was held for 12 h, and a new round flask was installed at the beginning of each 12 h period to collect the liquid products produced during each reaction condition. A summary of partial pressures used for the kinetic study is provided in Table 5.3. For all feed compositions, acetaldehyde conversions for all the catalysts were limited to 10% to maintain the differential reaction condition.

Table 5.3 Acetaldehyde and water partial pressure variations used in the kinetic study over α-MoC_{1-x}, β-Mo_2C, 1.0 ML Cu/α-MoC_{1-x}, and 1.0 ML Cu β-Mo_2C.

Varied Component	Notation	Aldehyde		Water	
		Partial Pressure (atm)	Ratio to Standard Composition	Partial Pressure	Ratio to Standard Composition
Acetaldehyde	A03	0.03	0.3	0.15	1
	A1 (Standard Composition)	0.09	1	0.15	1
	A2	0.17	1.8	0.15	1
	A3	0.26	2.9	0.15	1
Water	W1 (Standard Composition)	0.09	1	0.15	1
	W2	0.09	1	0.30	2
	W3	0.09	1	0.43	2.9
	W4	0.09	1	0.56	3.7

*Balanced by N_2. Aldehyde concentration verified by GC-TCD (bypass reactor)

As each set of experiment took four days to complete, acetaldehyde was required to be replenished during the experiment. When acetaldehyde level in the bubbler dropped to approximately 40% of the starting level, acetaldehyde was replenished using a syringe via a septum on the bubbler.

5.2.4 Rate Expressions for Kinetic Study

In this study, reaction rate data was fitted using power law and phenomenological-based kinetics models. The kinetics models evaluated were Redox, Ely-Rideal (E-R), and Langmui-Hinshelwood (L-H) mechanism. For the L-H model, the mechanism involving single and different/two adsorption sites were both evaluated.

- Redox

$$H_2O + s \rightarrow H_2 + s \cdot O \text{ (Equation 5.1)}$$

$$CH_3CHO + s \cdot O \rightarrow CH_3COOH + s \text{ (Equation 5.2)}$$

- Eley-Rideal (E-R), aldehyde adsorb

$$CH_3CHO + s \rightarrow CH_3CHO \cdot s \text{ (Equation 5.3)}$$

$$CH_3CHO \cdot s + H_2O \rightarrow CH_3COOH \cdot s + H_2 \text{ (Equation 5.4)}$$

$$CH_3COOH \cdot s \rightarrow CH_3COOH + s \text{ (Equation 5.5)}$$

- Eley-Rideal (E-R), water adsorb

$$H_2O + s \rightarrow H_2O \cdot s \text{ (Equation 5.6)}$$

$$H_2O \cdot s + CH_3CHO \rightarrow H_2 \cdot s + CH_3COOH \text{ (Equation 5.7)}$$

$$H_2 \cdot s \rightarrow H_2 + s \text{ (Equation 5.8)}$$

- Langmuir-Hinshelwood (L-H), single type of sites

$$CH_3CHO + S_1 \rightarrow CH_3CHO \cdot S_1 \text{ (Equation 5.9)}$$

$$H_2O + S_1 \rightarrow H_2O \cdot S_1 \text{ (Equation 5.10)}$$

$$CH_3CHO \cdot S_1 + H_2O \cdot S_1 \rightarrow CH_3COOH \cdot S_1 + H_1 \cdot S_1 \text{ (Equation 5.11)}$$

$$CH_3COOH \cdot S_1 \rightarrow CH_3COOH + S_1 \text{ (Equation 5.12)}$$

$$H_2 \cdot S_1 \rightarrow H_2 + S_1 \text{ (Equation 5.13)}$$

- Langmuir-Hinshelwood (L-H), two type of sites

$$CH_3CHO + S_1 \rightarrow CH_3CHO \cdot S_1 \text{ (Equation 5.14)}$$

$$H_2O + S_2 \rightarrow H_2O \cdot S_2 \text{ (Equation 5.15)}$$

$$CH_3CHO \cdot S_1 + H_2O \cdot S_2 \rightarrow CH_3COOH \cdot S_1 + H_2 \cdot S_2 \text{ (Equation 5.16)}$$

$$CH_3COOH \cdot S_1 \rightarrow CH_3COOH + S_1 \text{ (Equation 5.17)}$$

$$H_2 \cdot S_2 \rightarrow H_2 + S_2 \text{ (Equation 5.18)}$$

To derive the raw law expression for each phenomenological based kinetic model, a rate-determining-step (RDS) was first speculated. Note that the reverse reaction for the RDS was neglected. The RDS examined were aldehyde adsorption limiting, H_2O adsorption limiting, and surface reaction limiting. All other steps were assumed to be in pseudo-steady states [20,21]. Given that all reactions were run under differential condition, it was also assumed that the surface coverages of products were negligible in comparison with the surface coverage of the reactants. The rate law expressions derived based on these principles are listed in Table 5.4.

Table 5.4 Redox, Eley-Rideal (ER), Langmuir-Hinshelwood (L-H, single and two sites) models used for kinetic data fittings.

Model Description	Equation	Rate Law Expression
Power Law		$r = [P_{CH_3CHO}]^a \cdot [P_{H_2O}]^b$
Redox, water reduction limiting	5.1	$r = \frac{k_1 \cdot P_{H_2O}}{1 + K_2' \cdot P_{CH_3COOH}/P_{CH_3CHO}}, K_2' = 1/K_2$
Redox, aldehyde oxidation limiting	5.2	$r = \frac{k_2 \cdot P_{CH_3COOH}}{1 + K_1' \cdot P_{H_2}/P_{H_2O}}, K_1' = 1/K_1$
E-R, aldehyde adsorb, aldehyde adsorption limiting	5.3	$r = \frac{k_1 \cdot P_{CH_3CHO}}{1 + K_2' \cdot P_{CH_3COOH} \cdot P_{H_2}/P_{H_2O}}, K_2' = 1/K_2$
E-R, aldehyde adsorb, surface reaction limiting	5.4	$r = \frac{K_1 \cdot k_2 \cdot P_{CH_3CHO} \cdot P_{H_2O}}{1 + K_1 \cdot P_{CH_3CHO}}$
E-R, water adsorb, water adsorption limiting	5.6	$r = \frac{k_1 \cdot P_{H_2O}}{1 + K_2' \cdot P_{CH_3COOH} \cdot P_{H_2}/P_{CH_3CHO}}, K_2' = 1/K_2$
E-R, water adsorb, surface reaction limiting	5.7	$\mathrm{r} = \frac{K_1 \cdot k_2 \cdot P_{CH_3CHO} \cdot P_{H_2O}}{1 + K_1 \cdot P_{H_2O}}$
L-H, single type of site, aldehyde adsorption limiting	5.9	$r = \frac{k_1 \cdot P_{CH_3CHO}}{1 + K_2 \cdot P_{H_2O} + K_3' \cdot P_{CH_3COOH} \cdot P_{H_2}/P_{H_2O}}, K_3' = 1/K_2K_3K_4K_5$
L-H, single type of site, water adsorption limiting	5.10	$r = \frac{k_2 \cdot P_{H_2O}}{1 + K_1 \cdot P_{CH_3CHO} + K_3' \cdot P_{CH_3COOH} \cdot P_{H_2}/P_{CH_3CHO}}, K_3' = 1/K_1K_3K_4K_5$
L-H, single type of site, surface reaction limiting	5.11	$\mathrm{r} = \frac{K_1 \cdot K_2 \cdot k_3 \cdot P_{CH_3CHO} \cdot P_{H_2O}}{(1 + K_1 \cdot P_{CH_3CHO} + K_2 \cdot P_{H_2O})^2}$
L-H, two type of site, aldehyde adsorption limiting	5.14	$r = \frac{k_1 \cdot P_{CH_3CHO}}{1 + K_2' \cdot P_{CH_3COOH} \cdot P_{H_2}/P_{H_2O}}, K_2' = 1/K_2K_3K_4K_5$
L-H, two type of site, water adsorption limiting	5.15	$r = \frac{k_2 \cdot P_{H_2O}}{1 + K_2' \cdot P_{CH_3COOH} \cdot P_{H_2}/P_{CH_3CHO}}, K_2' = 1/K_1K_3K_4K_5$
L-H, two type of site, surface reaction limiting	5.16	$\mathrm{r} = \frac{K_1 \cdot K_2 \cdot k_3 \cdot P_{CH_3CHO} \cdot P_{H_2O}}{(1 + K_1 \cdot P_{CH_3CHO}) \cdot (1 + K_2 \cdot P_{H_2O})}$

The reaction rate data was fitted to the rate law expressions using Minitab 18, a commercial statistical software. An unconstrained non-linear regression method was used for fitting, and the Levenberg-Marquard algorithm was applied during the analysis. The maximum number of iterations and the convergence tolerance were set to 10^3 and 10^{-8}, respectively.

Root-mean-square error (RMSE), which is also known as standard error of residuals (S), is used to evaluate the goodness of fit for each model. The RMSE is normally used to compare statistics models with different degrees of freedom, including evaluation of different kinetic models [22–24]. The quantity of RMSE is the square root of mean square error (MSE). The MSE is calculated by dividing the residual sum of squares by the number of degrees of freedom.

$$\text{RMSE} = \sqrt{MSE} = \sqrt{\frac{Residual\ Sum\ of\ Squares}{Degree\ of\ Freedoms}}$$

To confirm the results derived by using RMSE, Akaike information criterion (AIC), another quantity commonly used for model comparison and evaluation was also calculated. Similar to the RMSE, the lowest AIC value identifies the most justified model. The AIC equation is as follows:

$$\text{Akaike information criterion (AIC)} = \text{n} \cdot \ln\left(\frac{Residual\ Sum\ of\ Squares}{n}\right) + 2(\text{P} + 1)$$

where, n is the number of data points and P is the number of estimated parameters in the model [25].

The model discrimination was performed on the basis of statistical significance measured by RMSE, AIC, and the physical meaning of the parameters estimated [22,23]. Models were discarded if the resulting parameter estimates were negative or have high RMSE/AIC values.

5.3 Results

5.3.1 Catalyst Characterization

When prepared using the wet impregnation method (target loading: 0.7ML Cu), the Cu deposition reached surface saturations of 0.24 ML and 0.56 ML of Cu on α-MoC_{1-x} and β-Mo_2C, respectively. Recall in Chapter 3, the Mo_2C supported Cu catalyst, where the Mo_2C was a mixture of α-MoC_{1-x} and β-Mo_2C, reached the Cu surface saturation at 0.47 ML (target loading: 0.7ML Cu). Given that J. Schaidle et al., and B. Wyvratt et al., reported that the PZC value plays a determining role during the wet impregnation on Mo_2C [7,14], the PZC values for the α-MoC_{1-x} and β-Mo_2C were determined. As shown in Figure 5.4, the PZC values for α-MoC_{1-x} and β-Mo_2C are approximately 6.1 and 5, respectively. The initial pH values of the Cu precursor solution used for α-MoC_{1-x} and β-Mo_2C were measured to be 4.62 and 4.97, respectively.

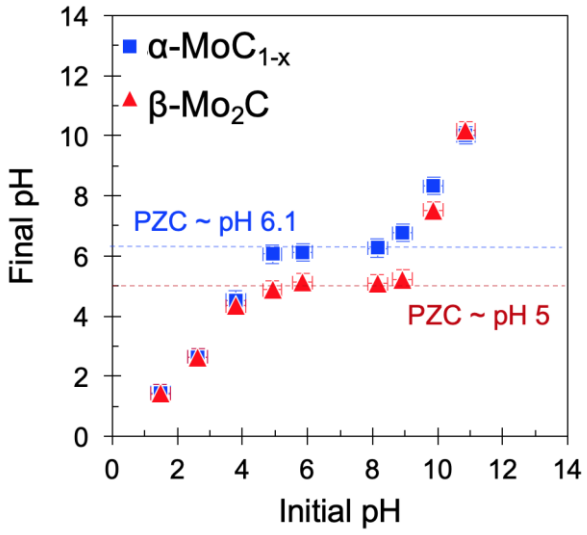

Figure 5.4 Point of zero charge determination for the native α-MoC_{1-x} and β-Mo_2C.

Given that high Cu loading cannot be achieved via wet impregnation, the technique of incipient wetness impregnation was adopted to deposit Cu on both α-MoC_{1-x} and β-Mo_2C. Note that when using incipient wetness impregnation, the target Cu loading is 1.0 ML on both α-MoC_{1-}

$_x$ and β-Mo_2C. In this chapter, the results and discussion will focus on the α-MoC_{1-x} and β-Mo_2C as well as its supported Cu catalysts prepared via incipient wetness impregnation.

The surface area, metal loading, CO chemisorption uptake, and NH_3 chemisorption uptake for α-MoC_{1-x}- and β-Mo_2C-based catalysts are summarized in Table 5.5. The preparation method of the α-MoC_{1-x}- and β-Mo_2C- supported Cu catalysts are also noted in the table. The α-MoC_{1-x} had a larger surface area than β-Mo_2C, and the surface areas of both phases of carbide are similar to values measured previously in the Thompson group [16,26]. While the CO site densities (μmol/m^2) are similar for α-MoC_{1-x} and β-Mo_2C, the β-Mo_2C had a slightly higher acid site density. Upon the deposition of 1.0 ML Cu, the surface areas of α-MoC_{1-x} and β-Mo_2C, and their acid site densities dropped.

Table 5.5 Surface and physical properties for α-MoC_{1-x} and β-Mo_2C and their supported Cu catalysts. Results for supported Cu catalysts prepared by wet impregnation are also included for reference.

Catalysts and Nominal Loading	Surface Area (m^2/g)	Metal Loading (wt%)	CO Uptake (μmol/g)	CO Uptake (μmol/m^2)	NH_3 Uptake (μmol/g)	NH_3 Uptake (μmol/m^2)
α-MoC_{1-x}	135	-	525	3.89	258	1.91
1.0 ML Cu/α-MoC_{1-x} (Incipient wetness)	103	12.1 (1.00 ML[a])	336	3.26	89	0.86
0.7 ML Cu/α-MoC_{1-x} (Wet impregnation)	161	3.1 (0.24 ML[b])	350	2.17	371	2.30
β-Mo_2C	64	-	228	3.56	165	2.58
1.0 ML Cu/β-Mo_2C (Incipient wetness)	35	6.1 (1.02 ML[a])	136	3.89	53	1.51
0.7 ML Cu/β-Mo_2C (Wet impregnation)	41	3.4 (0.56 ML[b])	161	3.93	107	2.61

[a] Determined by the amount of precursor used.
[b] Determined by elemental analysis.

From the XRD patterns of the catalysts, the obtained materials were confirmed to be the desired structure, which are the fcc α-MoC_{1-x} and the hcp β-Mo_2C [4,6]. The XRD patterns are shown in Figure 5.5. For carbide supported Cu catalysts, the Cu peaks could clearly be identified in the XRD patterns on both the α-MoC_{1-x} and the β-Mo_2C. However, the Cu peak at around 43 degree overlap with α-MoC_{1-x} and the Cu dimensions on β-Mo_2C were too small to be quantified using peak-broadening (Scherrer) fitting.

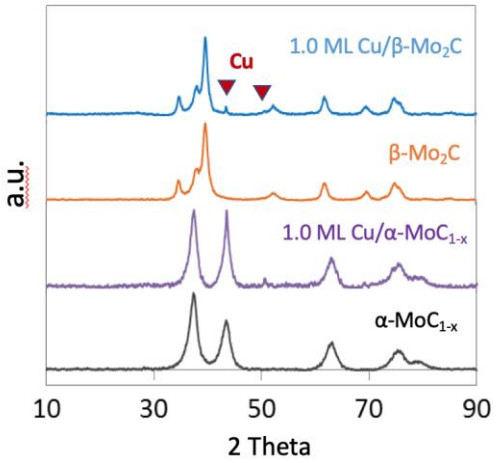

Figure 5.5 Diffraction patterns for α-MoC_{1-x}, β-Mo_2C, 1.0 ML Cu/α-MoC_{1-x}, and 1.0 ML Cu/β-Mo_2C.

Before the evaluation of catalysts, all the materials were pretreated in 15% CH_4/H_2 at 590 °C. To ensure the bulk structure of the catalysts were not altered by the pretreatment, control experiments were conducted. The α-MoC_{1-x} and β-Mo_2C catalysts were loaded into reactor, pretreated as described, quenched, and passivated. The bulk structures of the resulting materials were then examined again by XRD. The XRD patterns suggest that the bulk structures of the catalysts were intact and there was no detectable phase change during the pretreatment.

5.3.2 Aldehyde Water Shift Activity

For all of the catalysts, the activity decayed during the first few hours on stream, and pseudo-steady-state rates were reached after approximately 10 h at 240 °C. The pseudo-steady-

state AWS rates for α-MoC_{1-x}- and β-Mo_2C-based catalysts are provided in Table 5.6. Comparing the AWS activity, β-Mo_2C was more active, showing ~150% higher rate than that of α-MoC_{1-x}.

Table 5.6 H_2 production rates and turnover frequencies at 240 °C and activation energies for α-MoC_{1-x}, β-Mo_2C, and their supported Cu catalysts prepared via incipient wetness impregnation.

Catalysts	H_2 Production Rate (nmol/s/m^2)	Activation Energy (kCal/mol)
α-MoC_{1-x}	20.8	15
1.0 ML Cu/α-MoC_{1-x} (Incipient wetness)	49.3	15
β-Mo_2C	51.6	13
1.0 ML Cu/β-Mo_2C (Incipient wetness)	110.2	14

Upon the deposition of Cu via incipient wetness impregnation, the activity for AWS of both phases were enhanced. For α-MoC_{1-x} and β-Mo_2C, the deposition of 1.0 ML Cu elevated the activity by approximately 137% and 114%, respectively. The activation energies for all of the catalysts were very similar despite variations in their activities (see Table 5.6 and Figure 5.6).

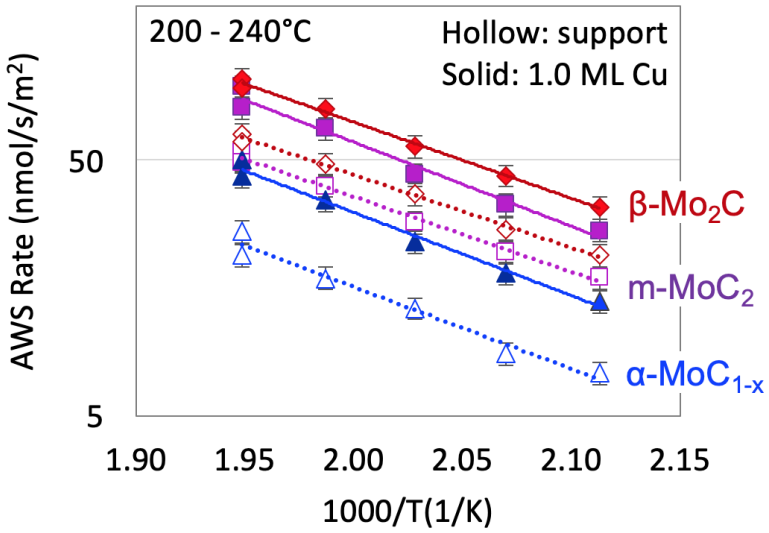

Figure 5.6 Arrhenius plots for the α-MoC_{1-x}, β-Mo_2C, 1.0ML Cu/α-MoC_{1-x}, and 1.0ML Cu/β-Mo_2C catalysts. Data m-Mo_2C and 1.0 ML Cu/m-Mo_2C are also included. Given that the m-Mo_2C is a mixture of α-MoC_{1-x} and β-Mo_2C, it is not surprising that the m-Mo_2C shows an activity in between α-MoC_{1-x} and β-Mo_2C.

5.3.3 Selectivity

The pseudo-steady-state rates of the side reactions are provided in Table 5.7. The rate of Cannizzaro reaction and the aldol condensation were measured by the production of ethanol and crotonaldehyde, respectively.

Table 5.7 Stabilized acetic acid, ethanol and crotonaldehyde production rates at 240 °C for α-MoC_{1-x}- and β-Mo_2C-based catalysts.

Catalysts	Acetic Acid	Cannizzaro Reaction Rate (Ethanol) (nmol/s/m^2)	Aldol Condensation Rate (Crotonaldehyde) (nmol/s/m^2)
α-MoC_{1-x}	38.7	13.6	2.8
1.0 ML Cu/α-MoC_{1-x} (Incipient wetness)	45.8	14.1	2.1
β-Mo_2C	95.3	56.4	3.2
1.0 ML Cu/β-Mo_2C (Incipient wetness)	152.7	79.8	2.9

The carbon selectivity for α-MoC_{1-x}, β-Mo_2C, 1.0 ML Cu/α-MoC_{1-x}, and 1.0 ML Cu/β-Mo_2C are shown in Figure 5.7. Selectivity data for the mixed-phase Mo_2C (m-Mo_2C) was also included for comparison (data were presented previously in Chapter 4). The α-MoC_{1-x} appeared to be slightly more selective (~5%) than β-Mo_2C. The deposition of 1.0 ML Cu on the α-MoC_{1-x} and β-Mo_2C slightly improved the selectivity to acetic acid. This is because the promotion effect of Cu admetal on AWS was more significant than that for the Cannizzaro reaction.

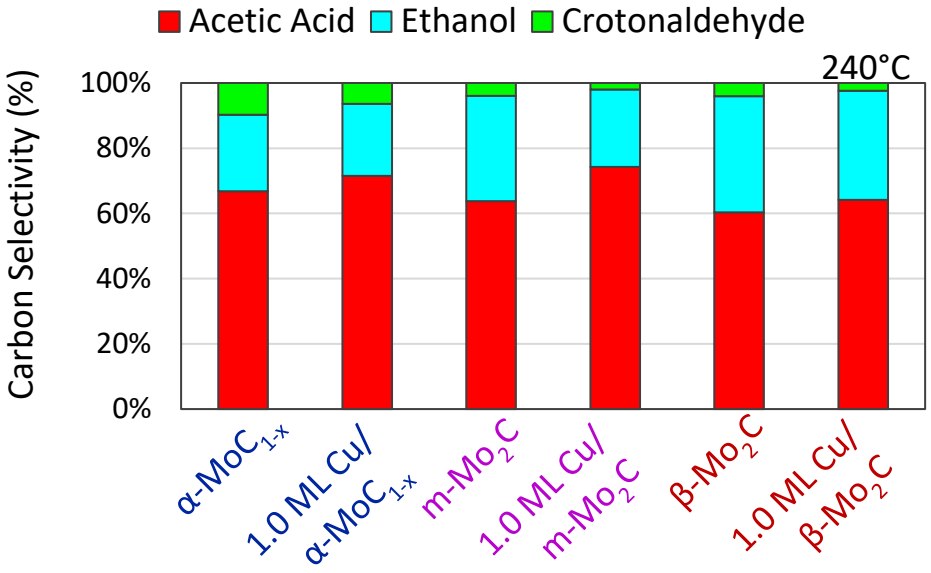

Figure 5.7 Carbon selectivity for α-MoC_{1-x}, β-Mo_2C, 1.0 ML Cu/α-MoC_{1-x}, and 1.0 ML Cu/β-Mo_2C. The data was collected during the pseudo-steady-state regime at 240 °C.

5.3.4 Reaction Kinetic and Mechanism

5.3.4.1 Power Law

The feed composition for the activity measurements was varied from the standard feed composition to obtain further insight into the reaction kinetics and mechanisms. Note that for the standard feed composition, the partial pressures of acetaldehyde and water are noted as A1 and W1 (reference partial pressure of acetaldehyde and water, being 0.09 atm and 0.15 atm, respectively). When varying the partial pressure, the number after A (acetaldehyde) or W (water) indicated the ratio to the standard feed composition (e.g. A03 stands for the partial pressure of acetaldehyde is 0.3 time of the standard feed composition). Reaction rates of AWS, Cannizzaro, and aldol condensations for each feed composition were shown in Figure 5.8 and Figure 5.10; selectivities are shown in Figure 5.9 and Figure 5.11.

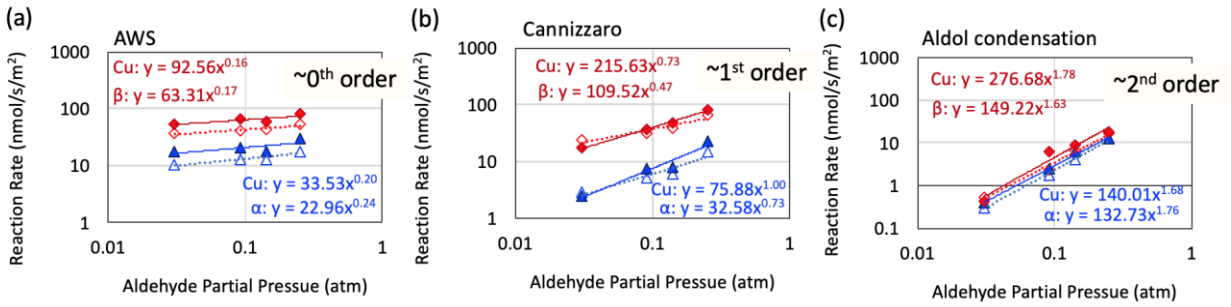

Figure 5.8 Reaction rates (a) AWS reaction, (b) Cannizzaro reaction, and (c) aldol condensation as a function of acetaldehyde partial pressure. The partial pressure of water was kept at a constant of 0.15 atm. The data was collected during the pseudo-steady-state regime at 240 °C. The data points in color blue is the results for α-MoC_{1-x} and the data points in color red is the results for β-Mo_2C. The hollow symbols stand for the data points for the bare supports, and the solid symbols represent the data points for the supported 1.0 ML Cu catalysts.

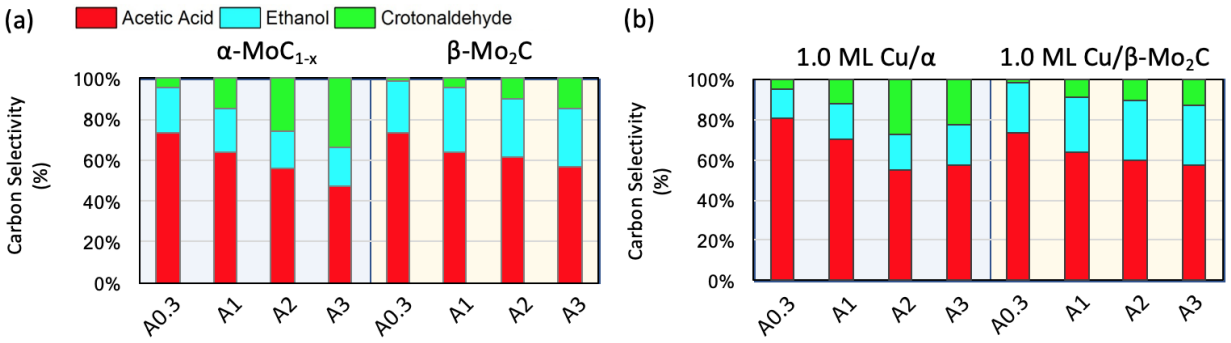

Figure 5.9 Selectivity of (a) α-MoC_{1-x} and β-Mo_2C (b)1.0 ML Cu/α-MoC_{1-x}, and 1.0 ML Cu/β-Mo_2C as a function of acetaldehyde partial pressure. The partial pressure of water was kept at a constant of 0.15 atm. The data was collected during the pseudo-steady-state regime at 240 °C.

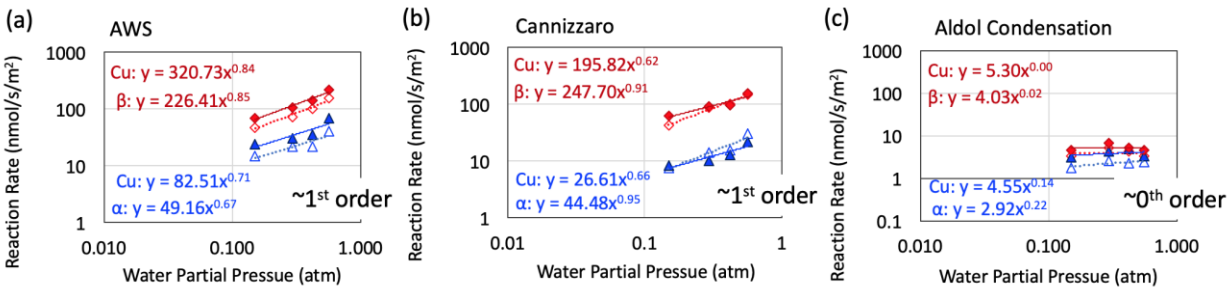

Figure 5.10 Reaction rates (a) AWS reaction, (b) Cannizzaro reaction, and (c) aldol condensation as a function of water partial pressure. The partial pressure of water was kept at a constant of 0.15 atm. The data was collected during the pseudo-steady-state regime at 240 °C. The data points in color blue is the results for α-MoC_{1-x} and the data points in color red is the results for β-Mo_2C. The hollow symbols stand for the data points for the bare supports, and the solid symbols represent the data points for the supported 1.0 ML Cu catalysts.

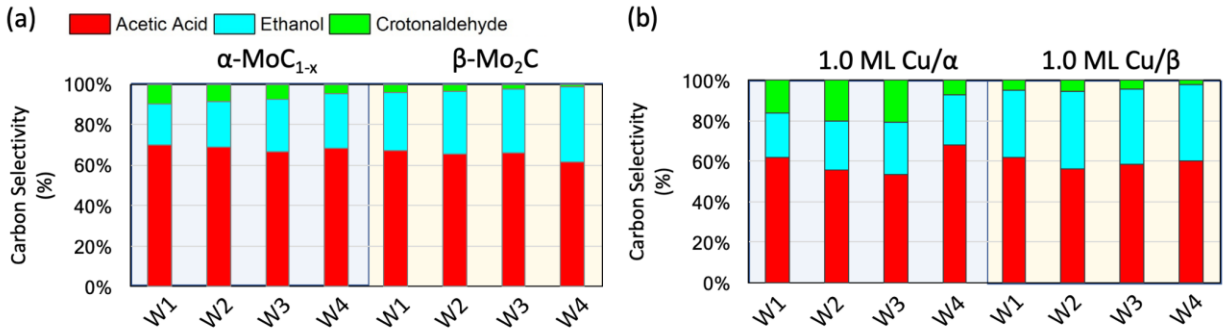

Figure 5.11 Selectivity of (a) α-MoC_{1-x} and β-Mo_2C (b)1.0 ML Cu/α-MoC_{1-x}, and 1.0 ML Cu/β-Mo_2C as a function of water partial pressure. The partial pressure of water was kept at a constant of 0.15 atm. The data was collected during the pseudo-steady-state regime at 240 °C.

From Figure 5.8 and Figure 5.10, it can be seen that each reaction had different orders to acetaldehyde and water, which drove the shifts in carbon selectivities as shown in Figure 5.9 and Figure 5.11. While varying the partial pressure of acetaldehyde, for both α-MoC_{1-x}- and β-Mo_2C-based catalysts, the AWS reaction showed weak dependencies (an order of ~0.15 to ~0.25) to acetaldehyde partial pressures. The Cannizzaro reaction had stronger dependencies (an order of ~0.5 to ~1.0), while the aldol condensation had the strongest dependencies to acetaldehyde partial pressures (an order of ~1.6 to ~1.8). When comparing the acetic acid selectivities between

aldehyde partial pressure of 0.03 atm and 0.26 atm, the selectivities to acid dropped 20 to 30% for all catalysts.

When varying the partial pressure of water, for both α-MoC_{1-x}- and β-Mo_2C-based catalysts, the AWS reaction and the Cannizzaro reaction both showed strong dependencies (an order of ~0.7 to 1.0) to water. In contrast, the Cannizzaro reaction had weak dependencies to water (an order of 0 to ~0.2). Unlike the selectivity results obtained when varying aldehyde partial pressure, the selectivities to acid were relatively consistent among all the catalysts and were not a function of water partial pressure. The reaction rate data for the three reaction were also fitted using power law; the fitted results are provided in Table 5.8.

Table 5.8 Fitting results for α-MoC_{1-x}, β-Mo_2C, 1.0 ML Cu/α-MoC_{1-x}, and 1.0 ML Cu/β-Mo_2C using power law. Rate data for AWS reaction, Cannizzaro reaction, and aldol condensation were fitted with Matlab: Rate = k $[aldehyde]^a[water]^w$, all $R^2 > 0.92$.

Catalysts	AWS Reaction			Cannizzaro Reaction			Aldol Condensation		
	Rate constant, k	Reaction Order		Rate constant, k	Reaction Order		Rate constant, k	Reaction Order	
		CH_3CHO	H_2O		CH_3CHO	H_2O		CH_3CHO	H_2O
α-MoC_{1-x}	113	0.26	0.84	632	0.98	1.31	274	1.9	0.25
1.0 ML Cu/ α-MoC_{1-x}	217	0.31	0.90	813	1.31	0.86	119	1.3	0.22
β-Mo_2C	403	0.19	0.97	938	0.51	1.06	206	1.59	0.17
1.0 ML Cu /β-Mo_2C	565	0.18	0.95	1156	0.62	0.96	94	1.21	-0.01

5.3.4.2 Phenomenological Based Kinetics

A summary of the model fitting for the redox, E-R, and L-H models are provided in Table 5.9. The model discrimination was performed based on the minimization of Root-mean-square error (RMSE) and Akaike information criterion (AIC), as well as physical meaning of the parameters estimated. Models were discarded if the resulting parameter estimates were negative

or have high RMSE/AIC values. The model discrimination results using RMSE and AIC are consistent.

Table 5.9 Model discrimination results for α-MoC_{1-x}, β-Mo_2C, 1.0 ML Cu/α-MoC_{1-x}, and 1.0 ML Cu/β-Mo_2C using redox, E-R, and L-H models. The presented figures follow the order of standard error of residuals (S), Akaike information criterion (AIC) (residual sum of squares, degree of freedoms). Models that produced the top-three best fits for each catalyst are highlighted.

Fitted Model and Rate Limiting Step	α-MoC_{1-x}	1.0 ML Cu/ α-MoC_{1-x}	β-Mo_2C	1.0 ML Cu/β-Mo_2C
Redox				
Water reduction	4.3, 26.9 (108.4, 6)	8.2, 37.4 (404.5, 6) Negative Parameter	9.2, 39.4 (521.1, 6)	14.0, 45.9 (1178.3, 6)
Aldehyde oxidation	11.1, 42.2 (734.2, 6)	19.2, 51.0 (2217.6, 6)	50.0, 66.3 (14970.6 ,6)	57.6, 68.6 (19902.3, 6) Negative Parameter
E-R, aldehyde adsorb				
Aldehyde adsorption	12.1, 43.6 (881.0, 6) Negative Parameter	21.9, 53.1 (2873.1, 6)	40.1, 62,8 (9665.0, 6) Negative Parameter	55.2, 67.9 (18252.6, 6)
Surface reaction	3.7, 24.6 (81.5, 6)	8.5, 37.9 (430.8, 6)	9.0, 38.9 (486.8, 6)	15.2, 47.2 (1385.2, 6)
E-R, water adsorb				
Water adsorption	4.4, 48.6 (114.9, 6)	8.3, 69.2 (414.7, 6) Negative Parameter	9.9, 74.7 (586.1, 6) Negative Parameter	16.0, 90.1 (1537.5, 6) Negative Parameter
Surface reaction	5.0, 52.8 (148.9, 6)	24.4, 103.6 (3564.4, 6)	21.0, 98.8 (2646.8, 6)	29.6, 109.8 (1537.5, 6)
L-H, single-type-site				
Aldehyde adsorption	5.5, 31.4 (148.4, 5) Negative Parameter	8.0, 37.4 (315.9, 5) Negative Parameter	17.5, 50.0 (1525.1, 5) Negative Parameter	23.0, 54.4 (2636.3, 5) Negative Parameter
Water adsorption	3.1, 22.3 (47.9, 5) Negative Parameter	6.0, 33.0 (181.3, 5) Negative Parameter	6.7, 34.6 (223.2, 5) Negative Parameter	10.9, 42.4 (590.8, 5) Negative Parameter
Surface reaction	4.0, 26.3 (78.7, 5)	9.4, 40.1 (441.7, 5)	11.4, 43.2 (654.3, 5)	18.6, 51.0 (1726.6, 5)

L-H, two-type-site				
Aldehyde adsorption	12.1, 43.6 (881.0, 6) Negative Parameter	21.9, 53.1 (2873.1, 6)	40.1,62.8 (9665.0, 6) Negative Parameter	55.2, 67.9 (18252.6, 6)
Water adsorption	4.4, 27.3 (114.9, 6)	8.3, 37.6 (414.7, 6) Negative Parameter	9.9, 40.4 (586.1, 6) Negative Parameter	16.0, 48.1 (1537.5, 6) Negative Parameter
Surface reaction	3.7, 25.1 (68, 5)	9.3, 39.9 (430.8, 5)	9.8, 40.8 (480.4, 5)	16.3, 48.9 (1334.0, 5)

As shown in Table 5.9, several models that has surface reaction as RDS fit the rate data reasonably well. Specifically, the E-R model (aldehyde adsorb, RDS: surface reaction) and L-H model (two types of adsorption site, RDS: surface reaction) produced a good fit for all of the catalysts. For α-MoC_{1-x} and 1.0 ML Cu/α-MoC_{1-x}, the L-H model (single type of adsorption site, RDS: surface reaction) also fitted the data reasonably well. For β-Mo_2C and 1.0 ML Cu/β-Mo_2C, the redox model (RDS: water reduction) fitted the data. Constants for each model that produced good fits are listed in Table 5.10, Table 5.11, Table 5.12, and Table 5.13.

Table 5.10 AWS kinetic parameters for the best-fit E-R model (aldehyde adsorb, RDS: surface reaction), $r = \frac{K_1 \cdot k_2 \cdot P_{CH_3CHO} \cdot P_{H_2O}}{1+K_1 \cdot P_{CH_3CHO}}$. K is the adsorption equilibrium constants for each species, and k is the forward rate constant.

Parameter	α-MoC_{1-x}	1.0 ML Cu/ α-MoC_{1-x}	β-Mo_2C	1.0 ML Cu/β-Mo_2C
K_1	7.12	7.26	48.42	46.36
k_2	181.05	281.5	323.76	467.40

Table 5.11 AWS kinetic parameters for the best-fit L-H model (single type of site, RDS: surface reaction) for α-MoC_{1-x}-based catalysts, $r = \frac{K_1 \cdot K_2 \cdot k_3 \cdot P_{CH_3CHO} \cdot P_{H_2O}}{(1+K_1 \cdot P_{CH_3CHO}+K_2 \cdot P_{H_2O})^2}$. K is the adsorption equilibrium constants for each species, and k is the forward rate constant.

Parameter	α-MoC_{1-x}	1.0 ML Cu/ α-MoC_{1-x}
K_1	3.35	1.96
K_2	0.26	2.23×10^{-7}
k_3	1806.19	3.90×10^{8}

Table 5.12 AWS kinetic parameters for the redox model with water reduction as the RDS for β-Mo_2C-based catalysts, $r = \frac{k_1 \cdot P_{H_2O}}{1+K_2' \cdot P_{CH_3COOH}/P_{CH_3CHO}}, K_2' = 1/K_2$. K is the adsorption equilibrium constants for each species, and k is the forward rate constant.

Parameter	β-Mo_2C	1.0 ML Cu/β-Mo_2C
k_1	297.08	625.80
K_2'	3.60	45.67

Table 5.13 AWS kinetic parameters for the best-fit L-H model (two types of site, RDS: surface reaction), $r = \frac{K_1 \cdot K_2 \cdot k_3 \cdot P_{CH_3CHO} \cdot P_{H_2O}}{(1+K_1 \cdot P_{CH_3CHO}) \cdot (1+K_2 \cdot P_{H_2O})}$. K is the adsorption equilibrium constants for each species, and k is the forward rate constant.

Parameter	α-MoC_{1-x}	β-Mo_2C	1.0 ML Cu/α-MoC_{1-x}	1.0 ML Cu/β-Mo_2C
K_1	25.08	54.04	7.26	55.93
K_2	0.74	0.09	1.89×10^{-5}	0.18
k_3	181.25	3733.11	1.48×10^{7}	2743.69

5.4 Discussion

In this Chapter, the surface properties, reactivities, and reaction kinetics for the α-MoC_{1-x} and β-Mo_2C supported Cu catalysts were examined. The catalytic properties of carbide supported Cu catalysts are found to be dependent on the carbide phase. Thus, the structure of the carbide need to be taken into consideration when designing future carbide catalysts.

In line with the findings in Chapter 3, when the catalysts were prepared via wet impregnation (target Cu loading: 0.7 ML), Cu deposition was observed to saturate the surface of α-MoC_{1-x} and β-Mo_2C. Interestingly, the Cu saturation levels differed for the α-MoC_{1-x} and β-Mo_2C, which was determined to be 0.24 ML and 0.56 ML, respectively. This difference in saturation levels could be a consequence of different PZC values of the catalysts. In experiments probing the PCZ values, the PZC value determined for the α-MoC_{1-x} was ~6.1 (solution initial pH: ~4.62) and β-Mo_2C was ~5.0 (solution initial pH: ~4.97). The obtained results could be explained by the theory proposed

by J. Park and J. Regalbuto. They indicated that when the PZC value of a catalyst is higher than that of the solution pH value, the surface of the catalyst could be slightly protonated [19]. Given that the α-MoC_{1-x} has a higher PZC value than the solution pH value, it is likely that the protonation of catalyst surface prevented the contact between Cu^{2+} ion and the α-MoC_{1-x} surface due to repulsion, resulting in a lower saturation level of Cu on the α-MoC_{1-x}. In contrast, β-Mo_2C has a PZC value relatively similar to the solution pH value. Consequently, it is possible to achieve a higher Cu loading on β-Mo_2C. Aside from the PZC examined in this research, other surface properties, such as zeta-potential [27], may also play a role during the Cu deposition on Mo_2C, which could be a focus of future research. As a high loading of Cu cannot be achieved via wet impregnation, Cu admetal was deposited onto α-MoC_{1-x} and β-Mo_2C using incipient wetness impregnation.

In catalyst evaluation experiments, the reactivity of carbides was found to be structure dependent, which is not unexpected. The hcp β-Mo_2C showed a 150% higher areal rate for AWS compared to that for fcc α-MoC_{1-x}. These trends parallel previous studies; J. Rodriguez et al. reported experimental results that β-Mo_2C is significantly more reactive towards water dissociation than MoC. Such higher reactivity resulted in higher coverage of O/OH on β-Mo_2C and higher areal WGS rates on β-Mo_2C than that for MoC [13]. Despite the difference in AWS rates, the selectivity observed for α-MoC_{1-x} and β-Mo_2C was relatively similar.

In this research, the promotion effect of Cu on activities was also observed. Upon the deposition of 1.0 ML Cu, the AWS activity for α-MoC_{1-x} and β-Mo_2C was enhanced by approximately 137% and 114%, respectively. The Cu on α-MoC_{1-x} showed a slightly higher degree of enhancement than that for β-Mo_2C, which may due to the metal-support interaction. Similar differences in the degree of activity enhancement induced by admetal were previously reported.

Lin et al. found that for Pt/α-MoC, the deposited Pt admetal exhibits a stronger integration with the fcc α-MoC than with the hcp β-Mo_2C. The strong metal-support interaction alters the surface electronic structure and forms an electron-rich domain at the interface of Pt and α-MoC, which enhances the bifunctional nature of the catalyst and leads to a higher methanol reforming activity on Pt/α-MoC [4]. Likewise, for WGS, Rodriguez et al. reported the deposition of Pt had a greater enhancement in activity on MoC than on β-Mo_2C [13].

While the degrees of enhancement induced by metal-support interaction resemble those from previous studies, the trends in actual AWS rates observed in this research are different from previous reports for WGS and methanol reforming. For AWS reaction, a higher areal rate on Cu/β-Mo_2C (110.2 nmol/s/m^2) was observed than that for Cu/α-MoC_{1-x} (49.3 nmol/s/m^2); for WGS reported previously, α-MoC supported metal (Pt, Au) catalysts showed higher activities [5,13] than the corresponding M/β-Mo_2C. Potential factors influencing the activity trend include the type of admetal, surface coverage of metal, metal-support interaction, and structure of the reactant [28–30]. It is also likely that certain phase of carbide favor specific reaction routes. This speculation is supported by the report of J. Rodriguez et al.; they reported that the Pt deposition on β-Mo_2C enhanced its activity by approximately 400%, for the side reaction producing CH_4 under WGS condition. Such enhancement was not observed for Pt/MoC [13]. This chemistry is not yet fully understood and could be the aim of future research.

In the kinetic study presented in this chapter, the results of power law fitting showed that the AWS, Cannizzaro reaction, and aldol condensation had different reaction orders to acetaldehyde and water; these differences had a strong impact on selectivities. While the AWS was almost zero order for acetaldehyde, Cannizzaro reaction and aldol condensation were strongly dependent on the acetaldehyde partial pressures, being first and second order, respectively. This is not

unexpected as both reactions required two acetaldehyde molecules to react. Given that both side reactions had stronger dependencies to acetaldehyde, higher selectivity to the acetic acid was observed at lower aldehyde partial pressures. High selectivity of 80% to acetic acid was obtained in this research, and even higher selectivity to acid may be achieved by further lowering the aldehyde partial pressure. In contrast, AWS and Cannizzaro reaction were both first order for water, while aldol condensation was independent to water partial pressures. Recall that the AWS and Cannizzaro reaction are the two major side reactions observed in this research. Both reactions had strong dependencies to the partial pressure of water, and varying the water partial pressure did not change the selectivities.

For the results of phenomenological-based kinetic models, several models fit the data reasonability well. Specifically, E-R model with aldehyde adsorb (surface reaction limiting) and L-H model with two distinct types of adsorption site (surface reaction limiting) produced a good fit for all of the catalysts. L-H model with single type of adsorption site (surface reaction limiting) well fit the data of α-MoC_{1-x} and 1.0 ML Cu/α-MoC_{1-x}; redox model (water reduction limiting) produced a good fit of β-Mo_2C and 1.0 ML Cu/β-Mo_2C. Recall that the apparent activation energies obtained for all catalysts are similar, which suggests that the RDS for all catalyst could be the same. While redox model and L-H model (single type of adsorption site) only fitted certain catalysts, the mechanism underlying the AWS reaction is more likely to be E-R mechanism (with aldehyde adsorbed, RDS: surface reaction) or L-H (two type of site, RDS: surface reaction). In addition, this speculation of the RDS parallels the kinetic studies reported for WGS reaction, in which the surface reaction was proposed to be the RDS for Mo_2C-based catalysts [5,31,32].

Despite that, it is difficult to draw a definitive conclusion. This similar goodness of fit is likely a consequence of limited range of reaction partial pressures tested in this research. In order

to obtain more conclusive evidence and better understand the mechanism, a wider range of reactant partial pressure is suggested. Kinetic experiments varying the acetaldehyde to water ratio could also provide additional insight [33,34].

5.5 Conclusion

In this chapter, the catalytic properties and reactivities of α-MoC_{1-x}, β-Mo_2C, and their supported Cu catalysts were evaluated for the AWS reaction. The incipient wetness impregnation method was adopted for metal deposition to reach the target Cu saturation levels on the α-MoC_{1-x} and β-Mo_2C, which was speculated to be limited by the PZC of materials when wet impregnation is used. In the evaluation of the catalysts, the β-Mo_2C showed 150% higher AWS areal rate compared to that for α-MoC_{1-x}. The deposited 1.0 ML Cu promoted the activity for AWS for both α-MoC_{1-x} and β-Mo_2C, by approximately 137% and 114%, respectively. The α-MoC_{1-x} had a slightly higher degree of enhancement, perhaps due to the stronger interaction between the Cu and α-MoC_{1-x}. It is likely that the enhancement observed for α-MoC_{1-x} and β-Mo_2C are due to the deposited Cu. The Cu admetals render additional sites for aldehyde adsorption, and the carbide supports are responsible for water dissociation, which resemble our conclusions drawn in Chapter 4.

In this chapter, kinetic experiments were also carried out to understand the reaction kinetics and mechanism for the AWS reaction. The AWS and Cannizzaro reaction were found to be ~1 order to water, while aldol condensation was ~0 order. In contrast, the Cannizzaro reaction and aldol condensation had strong dependency and a positive correlation with the partial pressure of acetaldehyde. AWS however, had a weak dependency. Consequently, higher selectivity to the AWS can be achieved by lowering acetaldehyde partial pressures. From the fitting results of phenomenological-based kinetic models, E-R with aldehyde adsorb (surface reaction limiting) and

L-H with two types of site (surface reaction limiting) appeared to stand out from other models. While determining the exact reaction mechanism from the results is challenging, the conclusions drawn from the kinetic experiments are not contradictory to our bifunctional mechanism hypothesis. Also, the results suggest that the AWS reaction could be limited by the surface reaction, which is consistent with reports for the WGS. However, investigations with wider ranges of partial pressure for each reactant could provide more insight into the mechanism.

5.6 References

[1] J. R. dos Santos Politi, F. Viñes, J. A. Rodriguez, F. Illas, Phys. Chem. Chem. Phys. 15 (2013) 12617–25.
[2] S. T. Oyama, The Chemistry of Transition Metal Carbides and Nitrides, Springer, Netherlands, 1996.
[3] S. T. Oyama, Catal. Today 15 (1992) 179–200.
[4] L. Lin, W. Zhou, R. Gao, S. Yao, X. Zhang, W. Xu, S. Zheng, Z. Jiang, Q. Yu, Y.-W. Li, C. Shi, X.-D. Wen, D. Ma, Nature. 544 (2017) 80–83.
[5] S. Yao, X. Zhang, W. Zhou, R. Gao, W. Xu, Y. Ye, L. Lin, X. Wen, B. Chen, E. Crumlin, J. Guo, Z. Zuo, W. Li, J. Xie, L. Lu, C.J. Kiely, L. Gu, C. Shi, J. A. Rodriguez, D. Ma, Science. 4321 (2017) 1–10.
[6] Y. Chen, S. Choi, L. T. Thompson, Catal. Today 259 (2016) 285–291.
[7] B. M. Wyvratt, J. R. Gaudet, L. T. Thompson, J. Catal. 330 (2015) 280–287.
[8] M. Siaj, I. Temprano, N. Dubuc, P. H. Mcbreen, J. Organomet. Chem.691 (2006) 5497–5504.
[9] R. Kojima, K. Aika, Appl. Catal. A. 219 (2001) 141–147.
[10] M. M. Sullivan, J.T. Held, A. Bhan, J. Catal. 326 (2015) 82–91.
[11] S. Posada-Pérez, P.J. Ramírez, R.A. Gutiérrez, D.J. Stacchiola, F. Viñes, P. Liu, F. Illas, J. A. Rodriguez, Catal. Sci. Technol. 6 (2016) 6766–6777.
[12] S. Posada-Pérez, F. Viñes, J. A. Rodríguez, F. Illas, J. Chem. Phys. 143 (2015) 114704.
[13] J. A. Rodriguez, P. J. Ramírez, R. A. Gutierrez, Catal. Today 289 (2016) 47–52.
[14] J. A. Schaidle, N. M. Schweitzer, O. T. Ajenifujah, L. T. Thompson, J. Catal. 289 (2012) 210–217.
[15] N. M. Schweitzer, J. A. Schaidle, O. K. Ezekoye, X. Pan, S. Linic, L. T. Thompson, J. Am. Chem. Soc. 133 (2011) 2378–2381.
[16] A. Djire, Dissertation, University of Michigan, 2016
[17] Y. Chen, S. Choi, L. T. Thompson, J. Catal. 343 (2016) 147–156.
[18] S. K. Bej, C. A. Bennett, L. T. Thompson, Appl. Catal. A 250 (2003) 197–208.
[19] J. Park, J. R. Regalbuto, J. Colloid Interface Sci. 175 (1995) 239–252.
[20] T. E. King, Dissertation, Uniservity of Michigan, 2007.
[21] N. M. Wilson, D.W. Flaherty, J. Am. Chem. Soc. 138 (2016) 574–586.
[22] E. Heracleous, A. A. Lemonidou, J. Catal. 237 (2006) 175–189.

[23] W. Ma, G. Jacobs, D. E. Sparks, R. L. Spicer, B. H. Davis, J. L. S. Klettlinger, C. H. Yen, Catal. Today. 228 (2014) 158–166.
[24] P. Kumar, S. R. Yenumala, S. K. Maity, D. Shee, Appl. Catal. A. 471 (2014) 28–38.
[25] C. M. Saffron, J. H. Park, B. E. Dale, T. C. Voice, Environ. Sci. Technol. 40 (2006) 7662–7667.
[26] B. M. Wyvratt, Dissertation, Uniservity of Michigan, 2016.
[27] R. López Cordero, F. J. Gil Llambias, A. López Agudo, Appl. Catal. 74 (1991) 125–136.
[28] K. Srilatha, N. Lingaiah, P. S. Sai Prasad, B. L. A. Prabhavathi Devi, R. B. N. Prasad, S. Venkateswar, Ind. Eng. Chem. Res. 48 (2009) 10816–10819.
[29] Y. Liu, E. Lotero, J.G. Goodwin, J. Catal. 243 (2006) 221–228.
[30] T. Gómez, E. Florez, J.A. Rodriguez, F. Illas, J. Phys. Chem. C. 114 (2010) 1622–1626.
[31] P. Liu, J. A. Rodriguez, Phys. Chem. B. 110 (2006) 19418–19425.
[32] H. Tominaga, M. Nagai, J. Phys. Chem. B 109 (2005) 20415–20423
[33] F. G. Botes, B. van Dyk, C. McGregor, Ind. Eng. Chem. Res. 48 (2009) 10439–10447.
[34] G. P. Van Der Laan, A.A.C.M. Beenackers, Catal. Rev. - Sci. Eng. 41 (1999) 255–318.

Chapter 6

Summary and Recommended Future Work

6.1 Summary and Overall Conclusions

The overall goal of the research described in this dissertation was to elucidate the structure-function relationship of heterogeneous catalysts for reactions using H_2O as a reactant to convert biomass feedstocks and biomass-derived products. With an aim to develop greener and more sustainable chemistries, catalyst research for such type of reactions that convert biomass with water, such as steam reforming, has drawn significant interests in the past decades [1–3]. In this research, aldehyde water shift (AWS) reaction is selected as the model reaction as an example of using water for biomass conversion to produce commodity chemicals and fuels.

To date, the catalyst research for the AWS reaction is limited and mainly focuses on homogenous complexes [4–7], and few heterogeneous catalysts [8–10]. Inspired by catalyst designs for analogous reactions using water as an oxidant, in particular water gas shift (WGS) and steam reforming of alcohol [2,3,11–15], the present research explores the use of heterogeneous catalysts for AWS reaction, and advances our understanding of their structure-function relationship. By correlating the catalyst performance to its catalytic properties, the characteristics of the active sites for the AWS reaction and side reactions on various type of metal oxide and molybdenum carbide catalysts were investigated.

In Chapter 2, We first evaluated a series of metal oxide supported metal catalysts, including CeO_2 and Al_2O_3 as supports for Pt, Cu, and Au admetals with 0.1 monolayers (ML) surface coverage. Cu-based catalysts were found to be more active than Pt- and Au-based catalysts; the

rate of Cu/CeO_2 was 3 times higher than those for Pt/CeO_2 and Au/CeO_2. The effects of support were further investigated by comparing the performance of Cu-Zn-Al, bulk Cu nanoparticle, and Cu/SiO_2 catalysts. We found that the catalysts that integrate surface Cu sites with reducible oxides (CeO_2 and ZnO) had the highest AWS activity. Cu/CeO_2 catalyst showed 8-fold higher Cu site-normalized AWS rate compared to that for the bulk Cu. The Cu-Zn-Al catalyst, in which the ZnO in Cu-Zn-Al is less reducible than CeO_2 [12], showed a 3-fold Cu site-normalized rate of that for bulk Cu. It is speculated that reducible oxides can dissociate water via the oxygen vacancy to provide the oxygen for the reaction while the Cu admetal provides the site for aldehyde oxidation. In contrast, the Cu site-normalized rates for Cu/Al_2O_3 and bulk Cu were similar, which implies that the activity of Cu/Al_2O_3 could be attributed to the Cu admetal. With these findings, we believe that the close proximity of sites for water dissociation and aldehyde oxidation could lead to high AWS activity, via a bifunctional mechanism.

Building on these discoveries, in Chapter 3 and Chapter 4, mix-phase molybdenum carbide (Mo_2C) supported metal catalysts were evaluated as the Mo_2C support is believed to possess sites for both water dissociation and aldehyde adsorption [16,17]. The bare Mo_2C showed a 2-fold or higher areal as compared to metal oxide supported Cu catalysts. This demonstrates its potential for being a highly active and non-innocent support for the AWS reaction. For Cu/Mo_2C catalyst with Cu loading of 0.1 ML prepared via incipient wetness impregnation, the Cu on Mo_2C showed a rate 14-fold higher than that for the bulk Cu. These results again verified the importance of the type of support, and suggest potential synergies between the Cu admetal and the Mo_2C support. When the Cu loading was increased from 0.1 to 2.0 ML, the AWS activity increased and peaked at 1.0 ML Cu with twice the areal rate compared to that of the bare Mo_2C. When varying Cu loading, AWS rates of Cu as predicted by the perimeter model well matched the experimental results. This further

suggests that the Cu-Mo_2C interfacial sites are critical for catalyzing the AWS reaction. These results are consistent with the bifunctional mechanism discussed earlier. Given that Mo_2C is known for its ability to dissociate water [16], the supported Cu could facilitate aldehyde oxidation using oxygen released from H_2O dissociation on Mo_2C sites. Additionally, this research demonstrated that the AWS activity of Mo_2C can be fully restored after regeneration. With its high activity and regenerability, Mo_2C-based materials could be ideal catalysts for industrial AWS application.

Catalysts based on phase-pure fcc α-MoC_{1-x} and hcp β-Mo_2C were synthesized and evaluated for AWS in Chapter 5; 1.0 ML of Cu was deposited on each of the two phases of carbide and evaluated as catalysts for the AWS reaction. The β-Mo_2C showed ~130% higher areal AWS rates compared to those for the α-MoC_{1-x}; Cu deposition of 1.0 ML coverage showed enhancements in AWS activities compared to their bare counters for both α-MoC_{1-x} (137% higher than bare α-MoC_{1-x}) and β-Mo_2C (114% higher than bare β-Mo_2C). As α-MoC_{1-x} has been reported to have a stronger interaction with metals (e.g. Pt and Au) compared to the β-Mo_2C [2,15], a similar effect may present between Cu and α-MoC_{1-x} which results in more significant enhancements in AWS activity on α-MoC_{1-x}. The promotional effect of Cu in higher AWS activities could also be a consequence of the bifunctional mechanism as previously discussed for the mixed-phase Mo_2C. In kinetic studies, the AWS was found to be ~1^{st} order in water, whereas the correlation with aldehyde partial pressure is relatively weak (~0.2 order). When evaluating phenomenological-based kinetic models, the Eley–Rideal with aldehyde adsorb (surface reaction limiting) and L-H with two types of site (surface reaction limiting) were the most consistent with the results obtained. While the fitting results for those models are similar and determining the exact reaction mechanism is challenging, it appears that the AWS reaction is limited by the surface reaction, similar to reports

for the WGS. Future investigations with larger ranges of each partial pressure could provide more conclusive evidence.

Aside from investigating the active sites for the AWS reaction, the characteristics driving the selectivity were also examined. For metal oxide supported Cu catalysts, Cu/CeO_2, Cu-Zn-Al, and bulk Cu were 60-70% selective to acetic acid, and other metal oxide supported catalysts produced primarily crotonaldehyde via aldol condensation. Results from the temperature-programmed desorption of NH_3 implicated weak acid sites were responsible for the formation of crotonaldehyde. In contrast to metal oxide-based catalysts, aldol condensation was noted to be a minor side reaction for Mo_2C-based catalysts. Mo_2C-based catalysts were 63-74% selective to acetic acid and produced ethanol as the major side product via Cannizzaro reaction (32-24% selective to ethanol). The Cannizzaro reaction rates were found to be a strong function of acid site densities of the catalysts, indicating that the Cannizzaro reaction could be catalyzed by the acid sites. It is speculated that the aldehyde adsorbed on the acid site interacts with the hydroxyl dissociated from water and forms a surface acetate. The acetate then reacts with another aldehyde adsorbed on an adjacent acid site to produce ethanol and acetic acid. By studying metal oxide and Mo_2C supported Cu, Pt, and Au catalysts for AWS reaction, the research described in this dissertation establishes a foundation for future investigations of the structure-function relationships.

6.2 Extension of Current Research

6.2.1 Further Examining the Characteristics of Surface Sites

Further characterization of surface sites, including CO sites, acid sites, and reactant adsorption sites, will provide stronger evidence and more direct support to the speculations and conclusions drawn in the dissertation.

In Chapter 4, the exposed Mo_2C surfaces of Cu/Mo_2C catalysts were estimated using CO uptake based on the speculation that majority of CO adsorption took place on Mo_2C surface. While our CO uptake support the speculation and the calculated Cu dispersions were consistent with the XRD observation, more direct evidence can further strengthen the argument. Diffuse Reflectance Infrared Fourier Transform Spectroscopy (DRIFTS) could be a powerful tool to examine such surface chemistry. By comparing the infrared spectra of bare Mo_2C and Cu/Mo_2C, whether additional CO adsorption sites were created by Cu admetal can be revealed. The location of CO adsorption on catalysts can also be identified by examining the infrared frequencies associated with certain domains of the catalyst surface. For instance, J. France and P. Hollins reported that CO adsorption on Cu gives an absorption band in 2070-2087 cm^{-1}, depending on the CO coverage and the Cu facet [18]. For hcp β-Mo_2C, it was reported two CO absorption bands appeared at 2054 and 2196 cm^{-1} [19,20]. Consequently, DRIFTS can be useful in identifying the location of CO adsorption sites on Cu/Mo_2C.

In addition to characterizing the CO adsorption sites, the IR spectra could also provide important information regarding the acid sites, which are speculated to be active for the Cannizzaro reaction as described in Chapter 4. The acid site densities were probed by NH_3 chemisorption and temperature program desorption (TPD). However, the NH_3 TPD can only reveal the total acid site densities, and cannot determine the type of acid sites (e.g. Lewis or Brønsted). As pyridine is known as an adsorbate interact only with the Lewis acid sites [21,22], different types of acid sites and site densities can be elucidated by examining the IR spectra of pyridine on Mo_2C-based catalysts. The correlation of the type of acid site and the rate of Cannizzaro reaction could be further obtained.

Lastly, DRIFTS can also provide valuable information for deducing reaction mechanisms. Such technique is widely utilized in mechanistic studies, including for WGS reaction [11,23,24]. By taking the spectra of catalysts exposed to acetaldehyde, water, and under reaction atmosphere, the surface species and reaction intermediates on the catalyst could be examined. As discussed in Chapter 5, the Eley-Rideal model (aldehyde pre-adsorb, RDS: surface reaction) and Langmuir-Hinshelwood model (two type of sites, RDS: surface reaction) both produced reasonably good fits to the rate data. Thus, it is difficult to conclude which mechanism underlying the AWS reaction. By examining the IR spectra after exposing catalysts to reactants (e.g. adsorbed water and hydroxyl), the surface species formed could provide more concrete evidence to determine the reaction mechanisms.

6.2.2 Revealing the Impact of Metal-Support Interactions to AWS activity

Aside from the characteristic of the active sites, electronic perturbation induced by the metal-support interactions can have determining effects on the reactivity of catalysts. X-ray photoelectron spectroscopy (XPS) experiments will allow us to examine such type of electronic perturbations. Numerous research has indicated that for Mo_2C supported metal catalysts, the electronic structure of the admetal is altered by such interactions. Experimentally, Yao et al. examined a 2 wt% Au/α-MoC catalyst with XPS and reported that the binding energy of Au 4f is about 0.6 eV higher compared to that for the bulk Au, which resulted in a stronger adsorption of CO on the electronically modified Au admetal in WGS [15]. A similar experimental observation was reported by Lin et al. For 2wt% Pt/α-MoC, the Pt $4f_{7/2}$ binding energy showed a shift 0.6 eV higher compared to metallic Pt [2]. Computationally, Posada-Pérez et al. demonstrated the interaction between Cu and fcc MoC lowered the activation energy barrier and facilitated the direct CO_2* dissociation to CO* + O* during CO_2 conversion [25]. Based on these reports, such could

also present on the Cu/Mo_2C catalysts studied in this research. With the XPS experiments, electronic structure of Cu/Mo_2C and the potential perturbations resulting from metal-support interactions could be revealed. The results may be further correlated with the reactivity of the catalysts.

6.2.3 Further Investigating Reaction Kinetics and Mechanisms

The research presented in Chapter 5 investigated the reaction kinetics and potential mechanisms for AWS on the α-MoC_{1-x}- and β-Mo_2C-based catalysts. Several phenomenon-based kinetic models produced a similar goodness of fit, which makes it difficult to conclusively determine the exact mechanism underlying the AWS reaction. This similarity in the goodness of fit is likely a consequence of the limited range of partial pressures tested. As described in Chapter 5, in kinetic experiments, the partial pressure range of acetaldehyde and water are 0.03 – 0.27 atm and 0.15 – 0.56 atm, respectively.

While the majority of kinetic experiments reported in literature tested over a wide pressure range of over an order of magnitude [26–28] (with a few exceptions [29]), the ranges of partial pressures used in this research were constrained by limitations of the reactor system. For example, the minimum partial pressure of acetaldehyde was limited by the flow rate on the mass flow controller installed, which controls the N_2 flow through the aldehyde bubbler; the maximum value was limited by the mass transport in the bubbler. Feeding aldehyde using an acetaldehyde/N_2 mixture gas cylinder instead of using a bubbler could be a practical solution for reaching lower acetaldehyde partial pressures. For water, the minimum partial pressure was limited by the lowest injection rate on the HPLC pump (0.01 ml/min). Replacing the HPLC pump with a syringe pump with an air-tight syringe may lower the injection rate of water and provide a wider range of water

partial pressure. With a wider range of partial pressures, more information can be obtained to establish a kinetic model with better resolution.

6.3 Research in New Areas

6.3.1 Elucidating the Effect of Preparation Methods on Carbide-based Catalysts

In this research, Mo_2C supported metal catalysts were prepared via two preparation methods, wet impregnation and incipient wetness impregnation. The preparation techniques could have impacts on the catalytic properties of catalysts.

In the two preparation methods employed in this research, the major differences in treatments are: (1) the volume of precursor solution that Mo_2C interact with, (2) the concentration of the precursor solution, and (3) the contact time of Mo_2C in the precursor solution. During wet impregnation, the Mo_2C particles were soaked in a 70 mL diluted metal precursor solution, and the particles were allowed to interact with the solution for 12 hours. In contrast, for incipient wetness impregnation, the Mo_2C was treated with a small amount (~8 µL/dropl, ~95 µL total) of high concentration solution of metal precursors (~700-fold of that for the wet impregnation). This method yields a short contact time, normally a few seconds before the solution droplet is absorbed by the support. With the drastic differences in the treatment, it is possible that catalysts prepared via different methods lead to different structures and hence different catalytic properties. One of the indications observed in this research is that, when targeting a high Cu loading of 0.75 ML during incipient wetness impregnation, sparkles were observed when the first few drops of the Cu precursor solution were added to the native Mo_2C; meanwhile, noticeable amount of heat was released. This is likely due to the severe redox reaction on the surface [30]. However, such a phenomenon was not observed during wet impregnation targeting a similar loading (0.7ML).

In Table 6.1, characterization results and AWS activity of 0.1 ML Cu/m-Mo_2C (mixed-phase) catalysts prepared via the two methods are compared. These results were presented in Chapter 3 and Chapter 5. While surface areas and NH_3 uptakes were similar, the Cu/Mo_2C prepared via incipient wetness impregnation had a higher CO uptake and AWS activity. This is somewhat unexpected, as we anticipated better Cu dispersion on catalyst prepared via wet impregnation, which could lead to better performance. Spectroscopy, such as DRIFTS, XPS, and transmission electron microscopy (TEM) with elemental mapping could provide information about the admetal particle size, surface structure and chemistry, and the electronic properties of the catalysts.

Table 6.1 Comparison of surface properties and AWS activity for 0.1 ML Cu/Mo_2C via incipient wetness impregnation and wet impregnation.

Catalysts	Surface Area (m^2/g)	CO Uptake ($\mu mol/m^2$)	NH_3 Uptake ($\mu mol/m^2$)	AWS Rate ($nmol/s/m^2$)	Activation Energy (kCal/mol)
0.1 ML Cu/m-Mo_2C (Incipient Wetness)	87	4.42	1.67	88	15
0.1 ML Cu/m-Mo^2C (Wet)	93	3.18	1.63	55	13

6.3.2 Understanding the Effect of Carbide Structure and Metal/Carbon Ratio

Increasing attention is paid to the effect of carbide structures and metal/carbon ratio on the catalytic properties of catalysts. Different structures of the carbide were reported to have different reactivities for numerous reactions including ammonia synthesis, CO oxidation, WGS reaction, and steam reforming [2,15,31–33]. Previous computational research demonstrated that the Mo_2C structure, Mo/C ratio, and the changes in coordination number of Mo/C, have a strong impact on the theoretical stability of the catalyst. Liu and Rodriguez indicated that the increase of C coordination number of the metal atoms enhanced the stability [34]. Politi et al. demonstrated that

the orthorhombic Mo_2C to be the most stable phase thermodynamically, closely followed by the hexagonal Mo_2C phase, and the fcc MoC phase is reported to be not stable [35]. On the other hand, via computational study, Shi et al. reported that the hcp Mo_2C (001) with Mo/C ratio of 2, has a much stronger dissociative adsorption of water compared to Mo_2C (101) with Mo/C ratio of 1. Consequently, Mo_2C (001) can dissociate water and form surface OH + H and O + 2H. In contrast, the dissociation reaches equilibrium on the Mo_2C(101) surface [36]. Echoing the report, Rodriguez et al. experimentally demonstrated that the Pt/β-Mo_2C (001) is much more reactive towards water than Pt/MoC. The Pt/β-Mo_2C(001) showed a much higher O + OH coverage from water dissociation and the coverage increased continuously with time; On Pt/MoC, the O + OH coverage was relatively a constant [33].

Researchers also reported that the structure of carbides has effects on its interaction with the surface admetal. Based on experimental results coupled with computational studies, Lin et al. and Yao et al. reported that fcc α-MoC had a stronger interaction with Pt and Au compared to the hcp β-Mo_2C. This stronger interaction led to a significantly higher activity on the fcc α-MoC for WGS and methanol reforming [2,15]. In Chapter 5, we reported that the α-MoC_{1-x} and β-Mo_2C had different surface properties (e.g. PZC and site density) and reactivities for AWS. It was also observed that the 1.0 ML Cu deposition promoted the AWS activity on α-MoC_{1-x} more significantly than on β-Mo_2C. However, in this research, the Mo/C ratios for α-MoC_{1-x} and β-Mo_2C were not determined. For the fcc α-MoC_{1-x}, various x values ranging from 0.5 to 0.8 has been reported [2,37]. This variation in the Mo/C ratio may have impacts on catalytic properties, however, the correlation is not well understood.

To better understand the effect of carbide structures and Mo/C ratios on the catalytic properties, characterizations using spectroscopy, such as XPS and XAS, could provide important

insights. Specifically, states of surface Mo and the electronic perturbations inducing by the metal-support interaction can be examined with XPS experiments. With XAS, we can examine the metals deposited on various phases of carbides, which the reduction of metal could subject to the structures of the carbide. Additionally, information on metal-support interactions can be obtained by investigating the coordination number of admetal and carbide support. Combining the findings in spectroscopy experiments with reactivity results presented in research, this could shed light onto the surface chemistry and further to our understanding of the structure-function relationship of the molybdenum carbide materials for AWS.

6.3.3 Coupling the Experimental Research with Computational Works

Computational work can provide support for the speculations drawn from experimental studies. For instance, abundant research has experimentally demonstrated that the metal-support interfacial sites can be the key leading to high activities for various reactions including WGS [11–14,38]. Using DFT calculations, Yao et al. calculated that the effective energy barrier for the WGS reaction on Au/α-MoC is 0.72 eV, which is significantly lower than the barrier of 2.69 eV on bare α-MoC. For Au/α-MoC, the RDS was demonstrated to surface reaction on the interfacial sites [15]. Similarly, Lin et al. reported the effective energy barriers in WGS for Pt/α-MoC and α-MoC, and the energy barriers computed were 0.91 eV and 1.87 eV, respectively; for Pt/α-MoC, the Pt-MoC interfacial sites are the active site [2]. In the same study, L. Lin et al. also computed the energy barrier for aqueous-phase reforming of methanol. In line with their reports for WGS using α-MoC, the energy barrier was lower by 0.63 eV upon Pt deposition. The active sites on Pt/α-MoC again were located at the interface of Pt and α-MoC. These findings in computational works strongly support the speculation proposed in the experimental studies.

To further understand the mechanism of admetal enhancing the catalyst reactivity for AWS reaction, DTF calculation can be a powerful tool. With the results discussed in Chapter 4, it is experimentally evident that the interfacial sites of Cu-Mo_2C played a key role in catalyzing the AWS reaction. By coupling the experiment findings with DTF calculations, mechanistic information could be further obtained. This can be a strong support for the speculative mechanisms deducted from experiment results in this research, and provide further insight and guidance to the future catalyst design for the AWS.

6.3.4 Extend the AWS Studies to Other Model Compounds

In this dissertation, acetaldehyde was selective as the model compound. For future research, it will be exciting to extend the AWS catalyst research to other compounds, such as 5-Hydroxymethylfurfural (HMF). HMF can be converted to 2,5-furan dicarboxylic acid (FDCA) via oxidation reactions, which is one of the top 12 value-added bio-derivative identified by the U.S. Department of Energy in 2009 [39]. As discussed in the Introduction, the oxidation reaction typically takes place in alkaline aqueous solutions with the presence of O_2 (0.5 – 10 atm) in low temperatures (25 °C to 100 °C). Supported noble metal catalysts (Pt, Au, and Pd) are common catalysts used for these type of reactions [40]. Recently, Davis et al. reported that H_2O could be the source of oxygen during the oxidation, participating via the form of hydroxyl groups (OH^-). However, in such proposed mechanism involving water, O_2 still played an indirect but essential role, regenerating the principal oxidant, OH^-, on the catalyst surface [41,42]. As the Mo_2C could provide oxygen source released from water dissociation, HMF oxidation using water as oxidant may be realized via an AWS reaction pathway.

6.4 Reference

[1] R. R. Davda, J. W. Shabaker, G.W. Huber, R.D. Cortright, J. A. Dumesic, Appl. Catal., B 56 (2005) 171–186.

[2] L. Lin, W. Zhou, R. Gao, S. Yao, X. Zhang, W. Xu, S. Zheng, Z. Jiang, Q. Yu, Y.-W. Li, C. Shi, X.-D. Wen, D. Ma, Nature. 544 (2017) 80–83.
[3] Y. Ma, G. Guan, X. Hao, Z. Zuo, W. Huang, P. Phanthong, K. Kusakabe, A. Abudula, RSC Adv. 4 (2014) 44175–44184.
[4] S. Murahashi, T. Naota, K. Ito, Y. Maeda, H. Taki, J. Org. Chem. 52 (1987) 4319–4327.
[5] G. G. Stanley, D. A. Aubry, N. Bridges, B. Barker, B. Courtney, ACS Div. Fuel Chem. Prepr. 49 (2004) 712–713.
[6] T. P. Brewster, W. C. Ou, J. C. Tran, K. I. Goldberg, S. K. Hanson, T. R. Cundari, D. M. Heinekey, ACS Catal. 4 (2014) 3034–3038.
[7] T. P. Brewster, J. M. Goldberg, J. C. Tran, D. M. Heinekey, K. I. Goldberg, ACS Catal. 6 (2016) 6302–6305.
[8] L. M. Orozco, M. Renz, A. Corma, ChemSusChem. 9 (2016) 2430–2442.
[9] L. M. Orozco, M. Renz, A. Corma, Green Chem. 19 (2017) 1555–1569.
[10] N. Xiang, P. Xu, N. Ran, T. Ye, RSC Adv. 7 (2017) 38586–38593.
[11] K. G. Azzam, I. V. Babich, K. Seshan, L. Lefferts, J. Catal. 251 (2007) 153–162.
[12] J. A. Rodriguez, P. Liu, J. Hrbek, J. Evans, M. Pérez, Angew. Chem. 119 (2007) 1351–1354.
[13] N. M. Schweitzer, J. A. Schaidle, O. K. Ezekoye, X. Pan, S. Linic, L. T. Thompson, J. Am. Chem. Soc. 133 (2011) 2378–2381.
[14] K. D. Sabnis, Y. Cui, M. C. Akatay, M. Shekhar, W. S. Lee, J. T. Miller, W. N. Delgass, F. H. Ribeiro, J. Catal. 331 (2015) 162–171.
[15] S. Yao, X. Zhang, W. Zhou, R. Gao, W. Xu, Y. Ye, L. Lin, X. Wen, B. Chen, E. Crumlin, J. Guo, Z. Zuo, W. Li, J. Xie, L. Lu, C.J. Kiely, L. Gu, C. Shi, J. A. Rodriguez, D. Ma, Science. 4321 (2017) 1–10.
[16] P. Liu, J. A. Rodriguez, Phys. Chem. B. 110 (2006) 19418–19425.
[17] M. Siaj, I. Temprano, N. Dubuc, P. H. Mcbreen, J. Organomet. Chem.691 (2006) 5497–5504.
[18] P. Hollins, J. Pritchard, Surf. Sci. 89 (1979) 486-495.
[19] W. Wu, Z. Wu, C. Liang, X. Chen, P. Ying, C. Li, J. Phys. Chem. B 107 (2003) 7088–7094.
[20] W. Wu, Z. Wu, C. Liang, P. Ying, Z. Feng, C. Li, C. Phys. Chem. Chem. Phys. 6 (2004) 5603–5608.
[21] D. Barthomeuf, Acidity and basicity in zeolites, in: G. Ohlmann, H. Pfeifer, R. Fricke (Eds.) Catalysis and Adsorption by Zeolites, 1st ed. Elsevier Science Publishing Company Inc. New York, 1991, pp. 157-169.
[22] M. I. Zaki, M. a. Hasan, F. A. Al-Sagheer, L. Pasupulety, Colloids Surf., A 190 (2001) 261–274.
[23] X. Wang, J. A. Rodriguez, J. C. Hanson, D. Gamarra, A. Martinez-Arias, M. Fernandez-Garcia, J. Phys. Chem. B 110 (2006) 428–434.
[24] T. Wang, Y.W. Li, J. Wang, M. Beller, H. Jiao, J. Phys. Chem. C 118 (2014) 3162–3171.
[25] S. Posada-Pérez, P. J. Ramírez, J. Evans, F. Viñes, P. Liu, F. Illas, J. A. Rodriguez, J. Am. Chem. Soc. 138 (2016) 8269–8278.
[26] N. M. Wilson, D.W. Flaherty, J. Am. Chem. Soc. 138 (2016) 574–586.
[27] C. Stegelmann, N. C. Schiødt, C. T. Campbell, P. Stoltze, J. Catal. 221 (2004) 630–649.
[28] A. A. Gokhale, J. A. Dumesic, M. Mavrikakis, J. Am. Chem. Soc. 130 (2008) 1402–1414.
[29] Z. J. Zhao, Z. Li, Y. Cui, H. Zhu, W.F. Schneider, W.N. Delgass, F. Ribeiro, J. Greeley, J. Catal. 345 (2017) 157–169.

[30] J. A. Schaidle, N. M. Schweitzer, O. T. Ajenifujah, L. T. Thompson, J. Catal. 289 (2012) 210–217.
[31] R. Kojima, K. Aika, Appl. Catal. A. 219 (2001) 141–147.
[32] S. T. Oyama, Catal. Today 15 (1992) 179–200.
[33] J. A. Rodriguez, P. J. Ramírez, R. A. Gutierrez, Catal. Today 289 (2016) 47–52.
[34] P. Liu, J. A. Rodriguez, J. Chem. Phys. 120 (2004) 5414–5423.
[35] J. R. dos Santos Politi, F. Viñes, J. A. Rodriguez, F. Illas, Phys. Chem. Chem. Phys. 15 (2013) 12617–25.
[36] Y. Shi, Y. Yang, Y.W. Li, H. Jiao, Appl. Catal., A. 524 (2016) 223–236.
[37] Y. Chen, S. Choi, L. T. Thompson, Catal. Today 259 (2016) 285–291.
[38] K. Mudiyanselage, S. D. Senanayake, L. Feria, S. Kundu, A.E. Baber, J. Graciani, A. B. Vidal, S. Agnoli, J. Evans, R. Chang, S. Axnanda, Z. Liu, J. F. Sanz, P. Liu, J. A. Rodriguez, D. J. Stacchiola, Angew. Chemie Int. Ed. 52 (2013) 5101–5105.
[39] T. Werpy, G. Petersen, A. Aden, J. Bozell, J. Holladay, J. While, A. Manheim, D. Elliot, L. Lasure, S. Jones, M. Gerber, K. Ibsen, L. Lumberg, S. Kelly, Top Value Added Chemicals from Biomass I—Results of Screening for Potential Candidates from Sugars and Synthesis Gas, U.S. Department of Energy, 2004
[40] Z. Zhang, K. Deng, ACS Catal. 5 (2015) 6529–6544.
[41] S. E. Davis, B. N. Zope, R. J. Davis, Green Chem. 14 (2012) 143–147.
[42] S. E. Davis, A.D. Benavidez, R.W. Gosselink, J. H. Bitter, K. P. De Jong, A. K. Datye, R. J. Davis, J. Mol. Catal. A: Chem. 388–389 (2014) 123–132.

Appendix

Supporting Information

Thermodynamic Calculation

The Gibbs free energies of reaction were calculated using the Gibbs free energies of formation listed in Table S2. The equilibrium conversions were calculated from the equilibrium constants, K_{eq}= Exp (-ΔG°/RT).

Table A.1 Thermodynamic properties and Gibbs free energy of reactions.

Species	**Gibbs free energy of formation (kJ/mol) at standard condition**	**Ref**
Acetaldehyde (g)	-133	[1]
Water (g)	-228.6	[1]
Acetic acid (g)	-374.2	[1]
Ethanol (g)	-167.9	[1]
Crotonaldehyde	-36.50	[2]
Reaction	**Gibbs free energy of reaction (kJ/mol)**	**Equilibrium Conversion at 240˚C**
AWS reaction	-12.6	94%
Cannizzaro reaction	-47.5	>99%
Aldol condensation	0.9	36%

Carbon Balance

For all carbon balance studies, the reaction temperatures were held at 240˚C. During the reaction, a portion of the acetaldehyde condensed when passing the condenser (at 5˚C), while the rest remained in the gas phase. The total amount of carbon in the gas phase (unreacted acetaldehyde) was determined using the GC-TCD and the total amount of carbon in the liquid phase (unreacted acetaldehyde and products) was determined using the GC-FID. Dividing the amount of carbon measured by the total amount of carbon injected, carbon balances between 74% an 96% were determined. Note that some acetaldehyde may have evaporated during transfer (e.g. from the condenser to vial for storage, and preparing and diluting samples for GC analysis) due to its low boiling point (20˚C). Thus, the carbon balance obtained is lower than the actual value. In control experiments with known amounts of the aldehyde, the carbon balances closed within 83% and 95%.

Table A.2 Carbon balance for all catalysts examined in this dissertation.

Metal Oxide-Based Catalysts	**Carbon Balance**	**Mix-phased Mo_2C-Based Catalysts**	**Carbon Balance**	**Pure Phase Mo_2C-Based Catalysts**	**Carbon Balance**
CeO_2	---	Mo_2C	90%	α-MoC_{1-x}	74%
Cu/CeO_2	77%	0.1 ML Cu/Mo_2C (Wet)	91%	β-Mo_2C	90.5%
Pt/CeO_2	92%	0.1 ML Pt/Mo_2C (Wet)	76%	1.0 ML Cu/α-MoC_{1-x}	96%
Au/CeO_2	74%	0.1 ML Au/Mo_2C (Wet)	79%	1.0 ML Cu/β-Mo_2C	90%
Al_2O_3	80%	0.5 ML Cu/Mo_2C (Wet)	77%		
Cu/Al_2O_3	80%	0.1 ML Cu/Mo_2C (Incipient Wetness)	85%		
Pt/Al_2O_3	74%	0.25 ML Cu/Mo_2C (Incipient Wetness)	78%		
Au/Al_2O_3	81%	0.5 ML Cu/Mo_2C (Incipient Wetness)	76%		
Cu/SiO_2	---	0.75 ML Cu/Mo_2C (Incipient Wetness)	84%		
Cu-Zn-Al	81%	1.0 ML Cu/Mo_2C (Incipient Wetness)	89%		
Nano-Cu	---	2.0 ML Cu/Mo_2C (Incipient Wetness)	76%		
		0.5 ML K/Mo_2C (Incipient Wetness)	95%		
		0.5 ML $Cu/K/Mo_2C$ (Incipient Wetness)	83%		

Reference

[1] J. R. Rumble, CRC Handbook of Chemistry and Physics, 98th ed; CRC Press, Boca Raton, FL, 2017
[2] Céondo GmbH Database. Chemical Properties of 2-Butenal, (E)- (CAS 123-73-9). https://www.chemeo.com/cid/37-661-7/2-Butenal (accessed July 18, 2018)